Spring 1-1-2011

Order and Disruption of Order Induced by Self-Assembled Monolayers

Stephanie Michelle Malone
University of Colorado at Boulder, stephanie.malone@colorado.edu

Order and Disruption of Order Induced by Self-Assembled Monolayers

by

Stephanie M. Malone

B.S.E., Princeton University, 2006

A thesis submitted to the Faculty of the Graduate School of the University of Colorado in partial fulfillment of the requirements for the degree of Doctor of Philosophy

Department of Chemical and Biological Engineering

2011

This thesis entitled: Order and Disruption of Order Induced by Self-Assembled Monolayers

Written by Stephanie M Malone

Has been approved for the Department of Chemical and Biological Engineering

_____

Daniel K. Schwartz

_____

Mark P. Stoykovich

Date_____

The final copy of this thesis has been examined by the signatories, and we find that both the content and the form meet acceptable presentation standards of scholarly work in the above mentioned disciplines.

Abstract

Malone, Stephanie Michelle (Ph.D., Chemical and Biological Engineering)

Order and Disruption of Order Induced by Self-Assembled Monolayers

Thesis directed by Professor Daniel K. Schwartz

Self-assembly is defined as objects spontaneously and reversibly arranging themselves in the absence of outside direction. It involves a delicate balance between interparticle and intermolecular attraction and repulsion forces, thus resulting in a lower thermodynamic energy for an ordered state. In this work, the effect of self-assembly has been studied in both thermotropic and lyotropic liquid crystals. The utility of liquid crystals lies in the synergistic alignment that arises from the inherent elasticity of the material. Liquid crystals orient themselves based on the surface chemistry or topography of a substrate, and the bulk of the material will then align in concert with that surface layer. This allows amplification of any surface interactions, or as studied in this work, surface order, which can then be easily characterized with polarized light.

Thermotropic, nematic liquid crystals were used to probe the relationship of the chain length of alkylsilane self-assembled monolayers (SAMs) to surface energy. It was found that the liquid crystals interact with only the outermost 4 molecules in a SAM. Additionally, it was found that rubbing can not only induce azimuthal orientation on chains longer than 5, but that it can alter the surface energy and impart polar liquid crystal tilt.

Thermotropic liquid crystals were also used to further understand the extent of surface passivation of glycidoxypropyltrimethoxysilane (GPTMS) SAMs. While it was expected that this surface would have low azimuthal anchoring energy, this property was exploited for the detection of double-stranded DNA (dsDNA). The chirality of the molecule, combined with negligible anchoring energy, combined to allow propagation of the unique chiral alignment of -32±4 when exposed to extended dsDNA

Finally, it was found that not only do linactants self-assemble into aggregates in 2D Langmuir-Blodgett films, but that linactants also followed the model of 3D micelles, despite being fundamentally different than micelles or hemimicelles. The size scale of these molecules are ~37 nm, rather than limited to the size of two molecules as with a micelle, despite an apparent CMC, as well as eventual onset of lyotropic phases.

Dedication

To my parents, for their unwavering faith in me.

Acknowledgments

First, I would like to thank my funding sources, I have received support from GAANN (Graduate Assistanceships in Areas of National Need), NSF MRSEC, DMR-0213918, DMR-0906735, DMR-0455490, DMR-0213918, and DMR-0455490. I appreciate the helpful discussion from my committee members, especially when out of my element with biological work. I am grateful to Arthur Klittnick, Renfan Shao, and Joe MacLennan for many helpful discussions in the beginning of my graduate studies that helped me to understand liquid crystal work in the very beginning. I'd like to thank the member of my group, Andrew Price, Siwar Trabelsi, Andrei Honciuc, Rob Walder, Mark Kastantin, Indiria Sriram, Blake Langdon, Nathaniel Nelson, Carolyn Schoenbaum, Aaron McUmber, Jon Monserud, Pat Noonan, Rudy Kashar, and Josh Mabry, for both the helpful and entertaining discussions that go on in lab. I've had the help of several good undergrads, Kevin Daly, Amit Shavit, and Stephanie Perkins, who all helped accomplish more work than I would have been able to on my own.

Most of all I would like to thank Dan, who always kept me in awe with his extensive knowledge of literature, and always had good ideas for me, and always encouraged me to keep moving forwarded, even when I get myself stuck on minutia. He has helped me improve greatly, and find even more areas when I can improve in the future.

Table of Contents

List of Tables

List of Figures

.

Chapter 1

Introduction

The formation of an ordered system has two pathways: external guidance and self-assembly. External guidance is intuitive: of course increased order is likely under directed assembly. More subtle, however, are the mechanisms of self-assembly. Self-assembly is defined as objects spontaneously and reversibly arranging themselves into an ordered structure without outside direction. For a self-assembled structure to exist, intermolecular or interparticle forces result in a lower overall free energy than the entropy entropic energy loss in the transition from disordered to ordered structures. This balance of thermodynamic forces is what makes self-assembly so sensitive: minute changes in environmental conditions can tip energetics so that self-assembly is no longer favored. The in-depth study of self-assembled order, and the disruption of that order, can be used to more fully understand surface energies and molecular interactions. Thorough understanding of these interactions can be used to develop sensing mechanisms, leading to a deep fundamental understanding of the world around us.

Order can be studied on multiple size scales, ranging from molecular order to colloidal crystals[1]. Understanding molecular order elucidates the mechanisms for chemical reactions and interactions: this paves the way for applications including surface coatings and catalysis. Regarding surface coatings, self-assembled

monolayers are especially useful as alignment layers for liquid crystals. The order imparted by the monolayer is then propagated epitaxially, effectively amplifying any surface topology or interactions. In this way, the study of liquid crystalline order and disorder can be used as an amplification method to obtain deeper understanding of studied systems.

1.1 Liquid crystals

The common phases of matter are familiar to us all: solid, liquid, and gas. In the case of a solid, intermolecular forces are stronger than the translational energy (i.e. $\frac{1}{2}kT$ for each degree of freedom), thus restricting molecular movement to vibrational modes and establishing molecular order. A crystalline solid possesses both translational and orientational order. Upon increasing translational energy (e.g. with heating), molecular vibrations become stronger than intermolecular forces, thus allowing the free molecular motion present in liquids and gases. The attractive intermolecular forces in a liquid are still quite strong; although free molecular motion is allowed, in actuality, liquids in do not fill much more volume than a solid. In contrast, to a first approximation, gases have no intermolecular interactions except in extreme conditions (e.g. extremely high temperature and pressure). Both liquids and gases lack positional and orientational order, making these materials completely isotropic.

Phase transitions are generally sharp; unless near the critical point, where clear transitions no longer exist between phases. Interestingly, an anisotropic mesophase known as liquid crystal exists for some classes of molecules. Unsurprisingly, liquid

crystals exhibit properties of both liquid and crystalline materials. While it flows freely, similar to a liquid, there is also long-range orientational order, similar to a crystalline solid. The amount of crystalline order depends on conditions such as temperature, concentration, phase, and any surface interactions.

1.1.1 Liquid crystalline order

Prior to deeper discussion of the phases and behaviors of liquid crystalline materials, a descriptive terminology must first be defined. The class of molecules that forms liquid crystal mesophases tends to be comprised of long, asymmetric molecules. The director ($\hat{n}$), is the average direction in which the long axis of the liquid crystal molecule is oriented. Unsurprisingly, not every molecule aligns itself exactly with the director. Instead, each molecule fluctuates somewhat from the overall director. This fluctuation is quantified by the order parameter,

$$S = \langle \frac{3cos^2\theta - 1}{2} \rangle, \text{ (eq. 1.1)}$$

where θ is the deviation of an individual molecule from the director orientation. Because this quantity is averaged over the bulk of the material, the brackets in equation 1.1 denote a temporal and spatial average. For an isotropic sample such as a liquid, S=0, whereas for a perfectly crystalline sample, S=1. S is on typically between 0.3 and 0.8 for a liquid crystal, and it decreases as the temperature increases (Figure 1.1)[2].

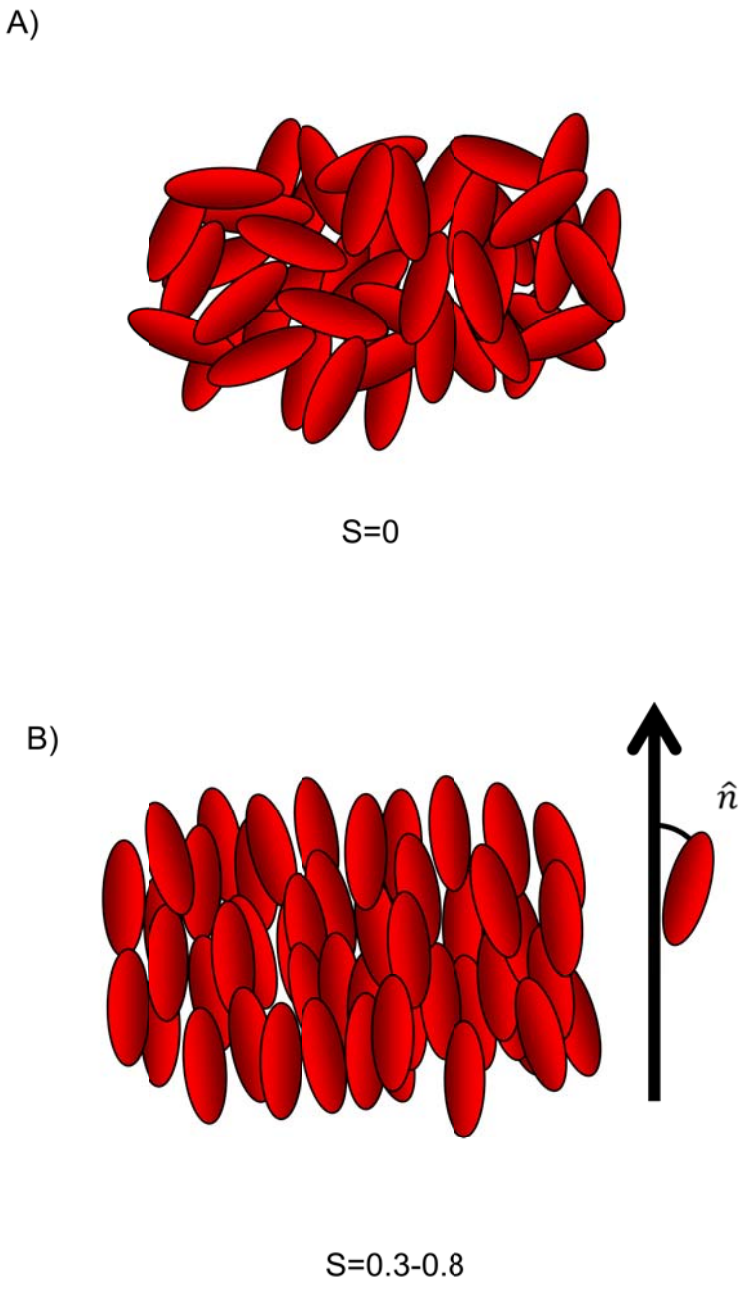

Figure 1.1: Liquid crystal molecules (represented by ovals) in the A) isotropic, B) liquid crystalline phase. The black arrow represents the director. Each molecule deviates on average from the director.

Orientation descriptions aside from deviations from the director are described analogously to the polar coordinate system. The azimuthal angle, θ, is the angle of the molecule projected into the x-y plane. The zenithal, or polar angle, is the molecule's angle relative to the z-axis.

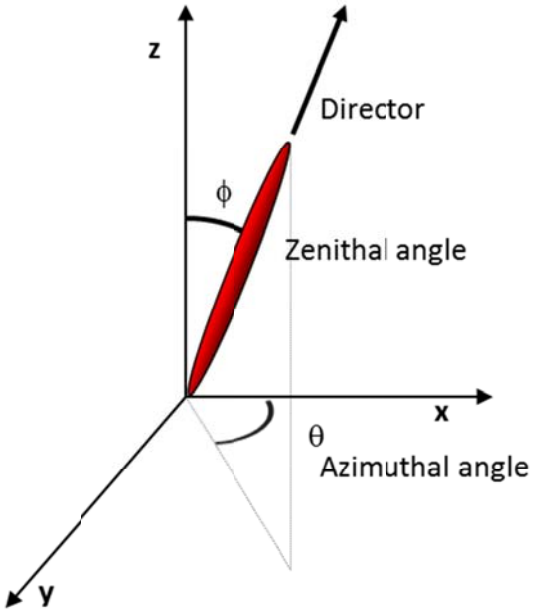

Figure 1.2: Description of the director, zenithal/polar anchoring, and the azimuthal angle as they relate to a single mesogen.

1.1.2 Liquid crystal type

Liquid crystalline order can be affected by the type of mesogen (i.e. individual liquid crystal molecule), mesogen concentration, or the temperature. While multiple molecular configurations may form liquid crystalline mesophases, the most common type is the calamatic liquid crystal, a rod-like molecule. In this case, one molecular axis is very different than the other two. What all classes of mesogens have in common, however, is molecular anisotropy. The main property of a calamatic liquid crystal is a central rigid moiety. This makes the molecule much longer in one dimension that is much longer than the other two molecular axes, fulfilling the requirement for molecular anisotropy.

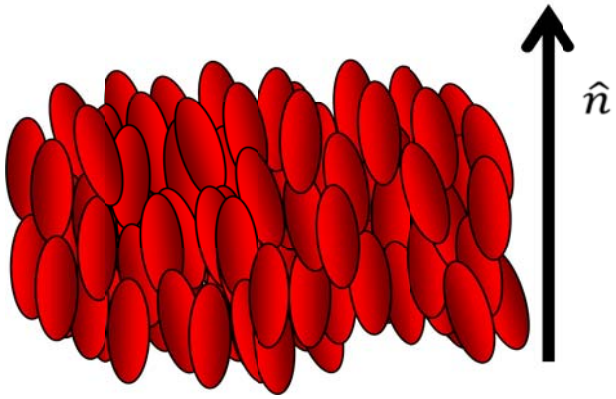

Figure 1.3: Calamatic liquid crystal in the nematic phase

This dissertation will discuss calamatic liquid crystals. Calamatics are type of thermotropic liquid crystals, which indicates that the order parameter is highly dependent on temperature. As temperature rises, the molecules gain more kinetic energy, causing increasing fluctuation from the overall director. Order then decreases, lowering the order parameter. Several distinct phases can exist in a calamatic; but each is only stable through a range of temperatures. The isotropic phase occurs after the liquid crystal has melted completely and becomes an isotropic liquid. The nematic phase has orientational, but no positional order. Smectic phases have both orientational and positional order (Figure 1.4).

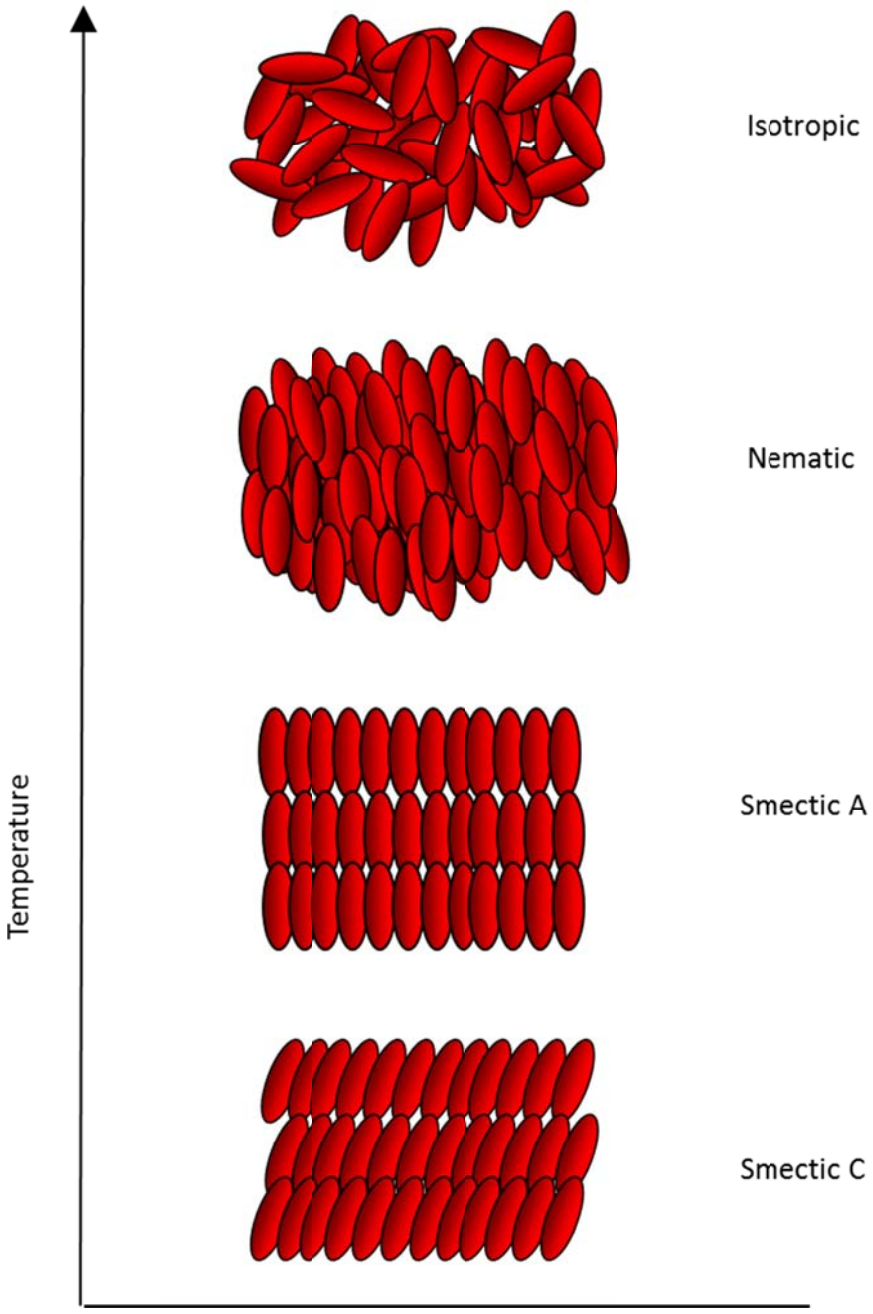

Figure 1.4: Liquid crystal phase changes with temperature. As temperature increases, the order parameter decreases, which can result in the isotropic, nematic, and smectic phases. This list includes the most common liquid crystal phases, but is not exhaustive.

As opposed to thermotropic liquid crystals, lyotropic liquid crystals change order parameter and phase with mesogen concentration. One such example is an aqueous surfactant solution. Above a critical concentration, surfactant molecules form ordered structures such as micelles and vesicles. At higher concentrations, surfactants form hexatic or lamellar phases, and exhibit liquid crystalline long-range order. Polymeric molecules with rigid moieties also form liquid crystalline phases under appropriate conditions, as the rigid moieties induce molecular anisotropy. Molecular anisotropy is the common link with all liquid crystalline mesogens, and that anisotropy allows liquid crystalline materials to maintain positional and orientational order in an otherwise fluid phase. This dissertation will discuss how the order in both thermotropic and lyotropic liquid crystals gives information about molecular-level structure, including molecular orientation and concentration.

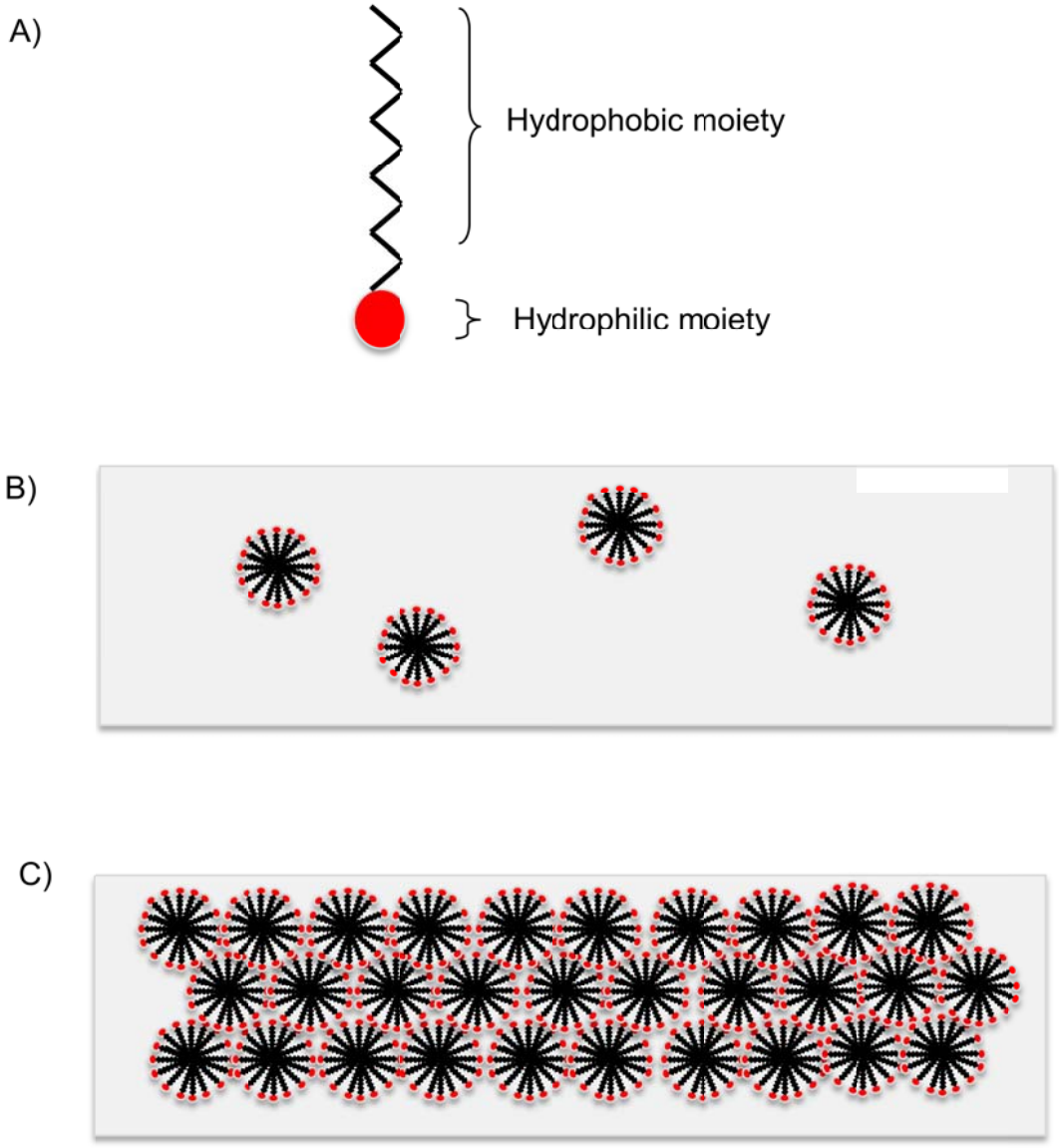

Figure 1.5: Schematic of a surfactant system undergoing lyotropic self-assembly. A) Single amphiphile with hydrophobic and hydrophilic moieties. B) Amphiphile spontaneously assembling into micelles. C) Micelles forming lyotropic liquid crystalline phases.

1.1.3 Nematic liquid crystals

As stated above, the extent of long-range order depends on the specific phase of liquid crystal. The nematic phase, used in this work, has order associated with the director, but no positional order. The naming of the nematic phase is inspired by its observable characteristics. Nematic is rooted in the Greek word for thread. When viewing a nematic liquid crystal through crossed polarizers, charachteristic topological defects present as dark "threads" running throughout the sample. In reality, these lines are discontinuities in orientational order are known as disclinations. In a disclination, the preferred direction of the liquid crystal is undefined[2].

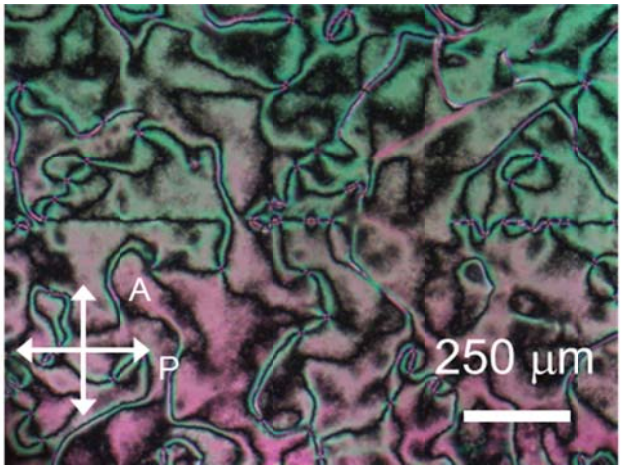

Figure 1.6: Image of a nematic liquid crystal viewed through crossed polarizers. Black lines are the disclinations characteristic to nematic liquid crystals. White arrows represent the crossed polarizers used for visualization.

The liquid crystals used in this work are 5CB (4-n-pentyl-cyanobiphenyl) and MBBA (*n*-(4-Methoxybenzylidene)-4-butylaniline). Both are calamatic, thermotropic liquid crystals, and are nematic at room temperature and have relatively low nematic to isotropic transition temperatures. (5CB T_{N-I}=35 °C, MBBA T_{N-I}=35 °C)[3]. These were chosen because extensive previous literature on both, and because of the contrast of electrical properties between the two mesogens.

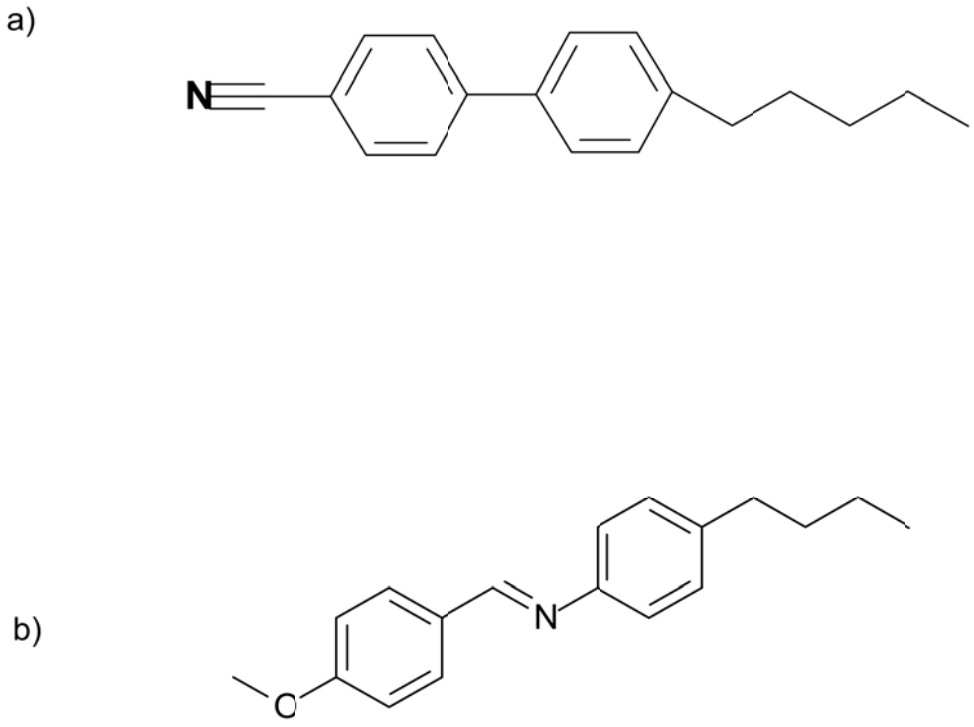

Figure 1.7: A) 5CB molecule B) MBBA molecule. 5CB is a polar liquid crystal, while MBBA is a nonpolar liquid crystal.

1.1.4 Birefringence

While most materials have only one index of refraction, birefringent materials such as liquid crystals have two. This separates incident light into two rays, the ordinary and extraordinary ray. The ordinary ray (n_o or $n_\perp$) follows Snell's law, and it vibrates perpendicular to the optical axis. The extraordinary ray (n_e or $n_{||}$) vibrates parallel to the optical axis, and does not follow Snell's law. The difference between these two values is the birefringence, defined as

$$\Delta n = n_e - n_o \text{ (eq 1.2).}$$

In optically positive materials, n_e is greater than n_o. The converse is true in optically negative materials. In either case, the axis with the larger index of refraction is the slow axis, and the one with the smaller index of refraction is the fast axis. Because of the two rays propagate at different velocities while travelling a fixed distance; they exit the material out of phase. The resulting phase difference is referred to as the retardation of the light. Retardation has two main consequences: rotation of the polarization of light, and interference colors.

Rotating the polarization of light is notable in birefringent materials because it allows for visualization through crossed polarizers. Crossed polarizers would normally block all transmission of light (Figure 1.8). A linear polarizer is designed so that once light passes through, it vibrates in only one direction. A material is then placed in the light path. If a material is non-birefringent, it has no effect on incident light. Thus, no light passes through the second polarizer (analyzer) because there is no component of light aligned with it, as the two polarizers are perpendicular to each other. A

birefringent material, however, will rotate the polarization of light. Once this occurs, a component of the light exists that can pass through the analyzer, thus allowing light to pass through the system.

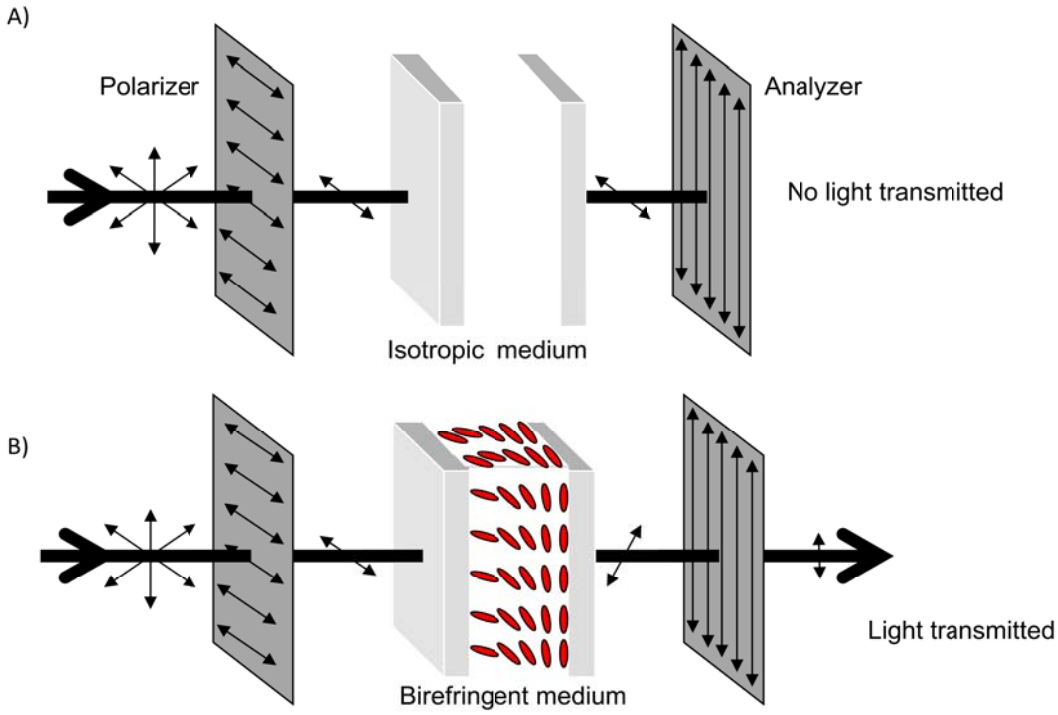

Figure 1.8: Scheme of visualization of birefringent materials through crossed polarizers. A) Light passing through a linearly polarizing filter will vibrate in a single direction. If it then passes through an isotropic medium, polarization is not altered, and the light is completely blocked by a second polarizer (analyzer), oriented at 90º to the first. B) Light passing through a birefringent medium is rotated, allowing a component to past through the second polarizer.

Polarized visualization also leads to the observation of interference colors. The index of refraction, and therefore the birefringence, is slightly dependent on the wavelength of light. This dependence on wavelength causes liquid crystals appear brightly colored when observed through crossed polarizers. The amount of retardation of the phases of

light can be estimated using the colors presented through crossed polarizers. Retardation and birefringence are related by

$$R = \Delta n \cdot d, \text{ (eq 1.3)}$$

where R is retardation, Δn is birefringence, and d is the thickness of the birefringent material. A simple method of estimating the birefringence of a sample is the Michel-Levy diagram[4](See Figure 1.9), a graphical interpretation relating interference color, birefringence, and thickness. If two of these variables are known, the third can be determined from the chart. The birefringence can then be used to determine the azimuthal and polar angles of the liquid crystal, provided thickness is known. Retardation can also be measured with a compensator for more accurate quantification[5].

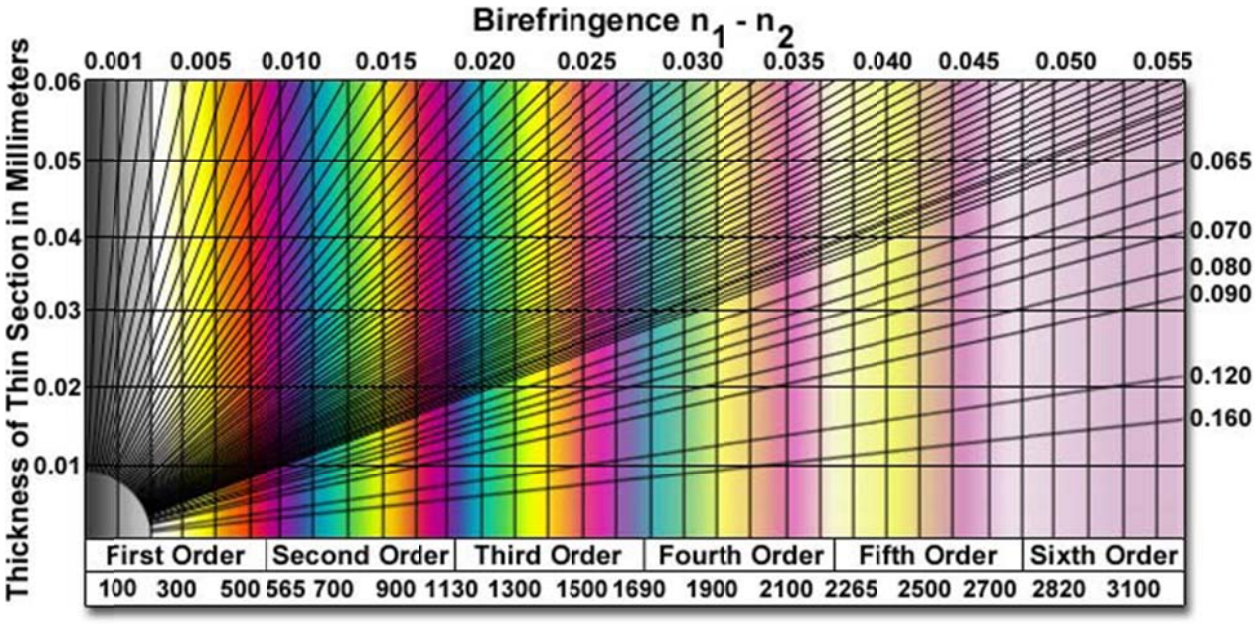

Figure 1.9: Michel-Levy diagram. If two of the three variables (thickness, birefringence, and interference color) are known, the third can be determined form the chart.

1.1.5 Liquid crystal anchoring

From a fundamental perspective, the anchoring and orientation of liquid crystals can be regarded as a sensitive probe of the surface properties of a substrate. Liquid crystals are capable of detecting surface conditions invisible to AFM, ellipsometry, and FTIR[6-8]. Previous work has used various surface modification approaches to create gradients[6, 9], patterns[3,10-13], and blended substratess[14, 15] in order to probe the subtleties of the liquid crystal/substrate interaction. If a liquid crystal molecule is polar, it can reorient in an electromagnetic field as well. This electroptic response is the basis for the twisted nematic cell, which switches from transmitting to blocking light, guided by the reorientation of liquid crystals in an electric field[2, 16]. More generally, liquid crystal reorientation in response to surface conditions and external fields can all be interpreted by tracking birefringence, which as stated previously is directly related to liquid crystal anchoring/orientation.

Liquid crystals are useful in display and sensor applications precisely because of the relationship between birefringence and response to environmental conditions. Additionally, the inherent elasticity of liquid crystal makes it a natural amplification mechanism. Another focus of this dissertation will be surface anchoring, i.e. the interactions between a liquid crystal and a bounding surface. Anchoring is quantified by measuring the anchoring energy, or the amount of energy necessary to perturb a molecule from the easy axis[17]. The easy axis is defined as the direction at which a liquid crystal aligns to minimize its elastic energy. Anchoring energy can be calculated from the surface free energy (γ) as follows:

$$\gamma \equiv \gamma(\theta_o, \phi_o) + W(\theta - \theta_o, \phi - \phi_o) \equiv \gamma(\theta_o, \phi_o) + W_a(\theta - \theta_o)W_p(\phi - \phi_o) \text{ (eq 1.4),}$$

where θ_o and $\phi_o$represent the azimuthal and polar easy axes, respectively. Surface energy can be separated into contributions from the azimuthal and polar anchoring energy. When $\theta = \theta_o$, the anchoring function W becomes a function of the polar anchoring energy (W_p) only. Likewise, when $\phi = \phi_o$, W become a function of only the azimuthal anchoring energy (W_a) only. Any chemical or physical alteration on the surface will alter liquid crystalline anchoring energy; thus tracking of anchoring energy creates a very useful probe for surface conditions.

1.1.6 Liquid crystal alignment techniques

Because easy direction and anchoring energy are highly dependent on surface anisotropy, alignment layers are often created by physical surface modification. A number of treatments have been empirically developed to induce desired surface alignment. Commonly, liquid crystal anchoring is directed by treating an substrate with physical or chemical methods such as rubbing, brushing, surface patterning, selective degradation, oblique evaporation, or Langmuir-Blodgett films[13, 18-32,33,34]. This manufactured anisotropy generates alignment layers which induce epitaxial liquid crystal alignment close to the substrate. Because of the energetic penalties associated with discontinuous director change, the bulk volume of the liquid crystal will then align itself to the surface layer in order to globally minimize elastic distortion energy. In this way, surface liquid crystals amplify surface conditions, allowing direct observation of surface phenomena via altered tilt/birefringence.

As stated previously, liquid crystals react incredibly sensitively to surface conditions, even those undetectable by other investigative methods. Even the method

of applying the previous treatments affects anchoring behavior. It is well known that rubbing strength is related to the degree of liquid crystal alignment and tilt [8,9,19, 31,29, 35, 36]. Despite its sensitivity to methodology, rubbing is the standard technique for commercial alignment layers because of its high throughput and ease of use. The most common defects in LCDs, however, are direct byproducts of rubbing. Static electricity and dust, both of which are inevitable byproducts of rubbing a substrate, result in dead pixels. This is one of the main reasons large displays are disproportionately expensive: as the display grows larger, it is rarer for a screen to be flawless. Thorough understanding of liquid crystal alignment and surface interactions will lead to improved contact-free alignment systems, which obviously have commercial potential for large screen applications.

1.1.8 Types of liquid crystal alignment

Liquid crystal alignment has three main states: homeotropic, planar, and tilted. In homeotropic alignment, the director lies perpendicular to the alignment layer. In planar alignment, the director of the liquid crystal molecule lies parallel to the alignment layer. Tilted alignment is intermediate between homeotropic and planar alignment. Combinations of any of these types are known as hybrid aligned cells (Figure 1.10).

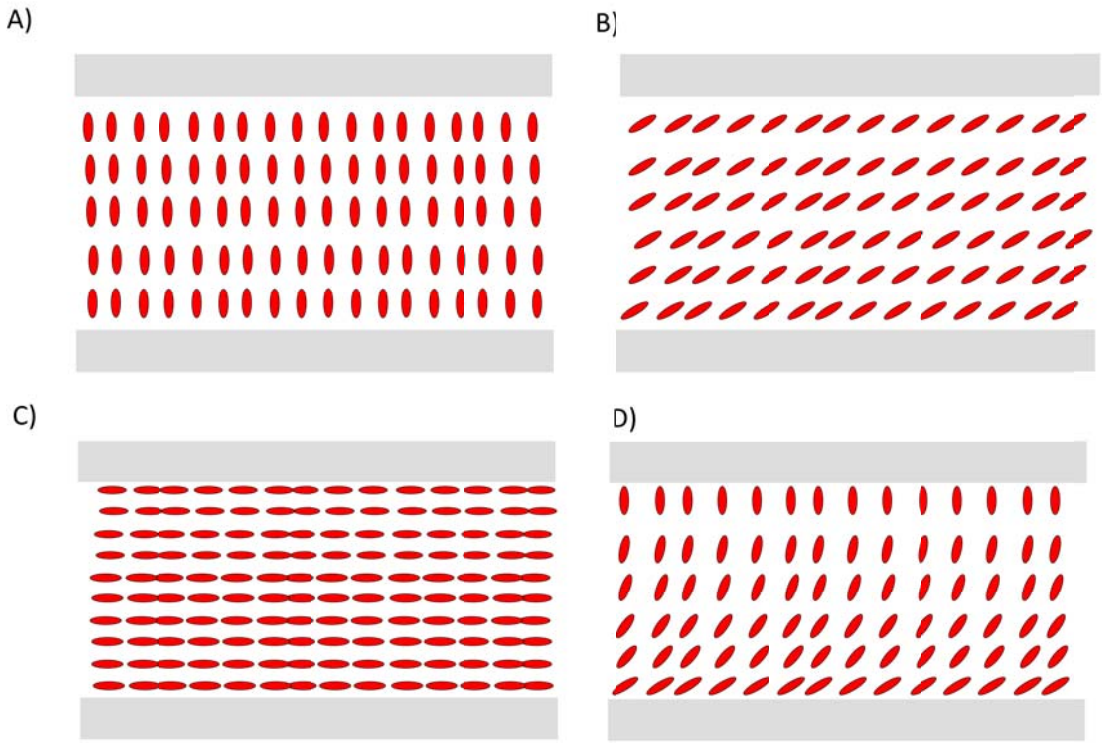

Figure 1.10: Depictions of liquid crystal alignment in liquid crystal cells. The gray rectangles indicate alignment layers, while the red ovals indicate liquid crystal molecules. A) Homeotropically aligned liquid crystal cell, where the liquid crystal molecules are aligned perpendicularly to the substrate. B) Tilted aligned liquid crystal cell. C) Planar aligned liquid crystal cell, where the liquid crystal lies parallel to the substrate. D) Hybrid aligned liquid crystal cell, where the top surface is homeotropic, and the bottom surface is tilted. Note the smooth transition between tilted to homeotropic alignment in the HAN cell. This is a result of the inherent elasticity of liquid crystals.

Liquid crystals are an elastic material; therefore they undergo continuous orientation transitions shifts (Figure 1.10d). In the absence of any biasing force, molecules in the nematic phase will align in a single direction. If a discontinuity (disclination) forms, it manifests as a point or line defect in order. Both of these responses serve to minimize the elastic distortion energy, as liquid minimizes free energy by avoiding discontinuous changes in the director, as this disrupts the elastic

distortion energy. The requirement for continuous anchoring is what allows the classification of liquid crystal alignment as a mesoscopic rather than a microscopic phenomenon. Because of its inherent elasticity, the liquid crystal acts as a bulk material rather than as discrete molecules, allowing for effective modeling with the elastic continuum theory. This theory can be simplified to apply tor nematics to calculate the elastic energy:

$$F = \frac{1}{2}[K_s(\nabla \cdot n)^2 + K_t(\mathrm{n} \cdot \nabla \times n)^2 + K_b(\mathrm{n} \times \nabla \times n)^2], \text{ (eq 1.5)}$$

This relationship denotes the Frank elastic energy[37]. The three constants associated with deforming liquid crystals are K_s, the splay constant, K_t, the twist constant, and K_b, the bend constant. The free energies associated with liquid crystal deformations are the splay $[\frac{1}{2}K_s(\nabla \cdot n)]$, twist $[\frac{1}{2}K_t(\mathrm{n} \cdot \nabla \times n)]$, and bend $[\frac{1}{2}K_b(\mathrm{n} \times \nabla \times n)]$, which are represented in Figure 1.11.

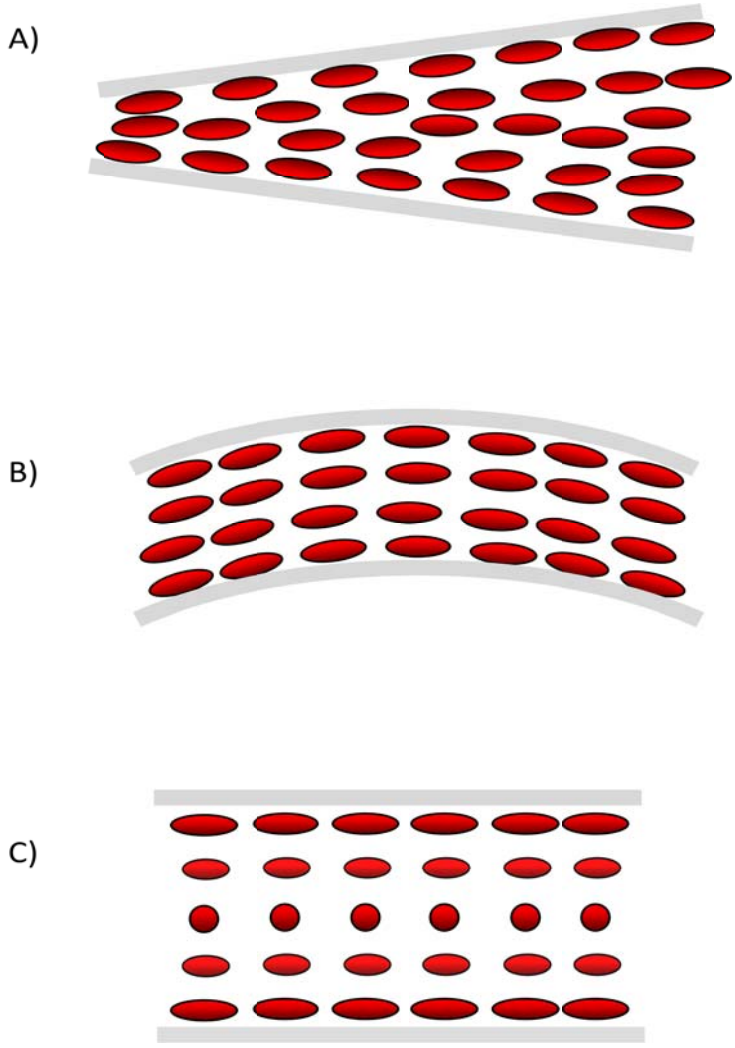

Figure 1.11: Schematic of three main types of elastic distortions in liquid crystals: A) Splay B) Bend C) Twist

Liquid Crystal Elastic Constants[3]	K_{11} (splay)	K_{22} (twist)	K_{33} (bend)
5CB	6.4 pN	3 pN	10 pN
MBBA	6 pN	4 pN	7.5 pN

Table 1.1: Elastic constants of 5CB and MBBA

Elasticity also highlights the importance of surface anchoring on control of liquid crystal alignment. Despite the easy axis defining the local energy minimum, it is common for liquid crystals to align obliquely to it. This is because competing elastic forces dictate that deviation from the easy axis will reach the global energy minimum. If the two easy axes of a liquid crystal cell are not aligned, the bulk energy must also be accounted for, as the combination of the surface and bulk energy must be minimized. For example, in a twist cell, the easy axes of each substrate are perpendicular to each other. Rather than align each easy axis, and transition between the two in bulk, the twist angle instead is less than 90°. In this case, minimizing the twist energy outweighs the energy penalty for deviating from the easy axis.

Anchoring energy, or the amount of energy necessary to deviate from the easy axis, is related to the bulk elastic constants previously mentioned in the Frank continuum theory. Relating anchoring energy to the Frank elastic constants also defines new quantity known as the extrapolation length,

$$L = \frac{K}{W} \text{ (eq 1.6)}$$

where L is the extrapolation length, K is elastic constant, and W is the anchoring energy. Extrapolation length is qualitatively defined as the distance from a discontinuity until the director again coincides with the easy axis. For low anchoring energy, it is easy to see that this results in long extrapolation lengths, and that any molecule decorating the surface imparts a large influence on liquid crystal alignment. Likewise, when there is high anchoring energy, the director returns to the easy axis much closer to the disclination. The combination of liquid crystal elasticity and the anchoring strength explain the extrapolation length thoroughly, and the control of these parameters provides the basis for liquid crystalline detection.

1.1.9 Visualization of liquid crystal alignment

As described by the Michel-Levy diagram, different liquid crystal orientations result in distinct birefringence colors when viewed through crossed polarizers. A homeotropicly aligned liquid crystal presents as black through all angles of rotation. Because the liquid crystal is perpendicular to the alignment layer, and thus parallel to the optical axis, the light “sees” only a single index of refraction, and it behaves as a non-birefringent material. If liquid crystal has nonzero polar tilt, it behaves as a birefringent material, and interference colors are visible viewed through crossed polarizers.

Polar alignment is detected by interference colors, but the presence of azimuthal alignment is observed as a result of rotation. If a sample is degenerate, (random

azimuthal alignment), as it is rotated, the average intensity of the light passing through the sample will remains constant. At high magnification, Schlieran textures become evident (Figure 1.6). The dark lines (nematic threads) indicate local alignment with one of the crossed polarizers. When liquid crystal is aligned with either of the two polarizers, no light is transmitted (extinction). If the sample is azimuthally aligned, however, extinction occurs globally in the sample. If there is azimuthal alignment, intensity minima occur every 90° of rotation as the liquid crystal aligns with either the polarizer or analyzer.

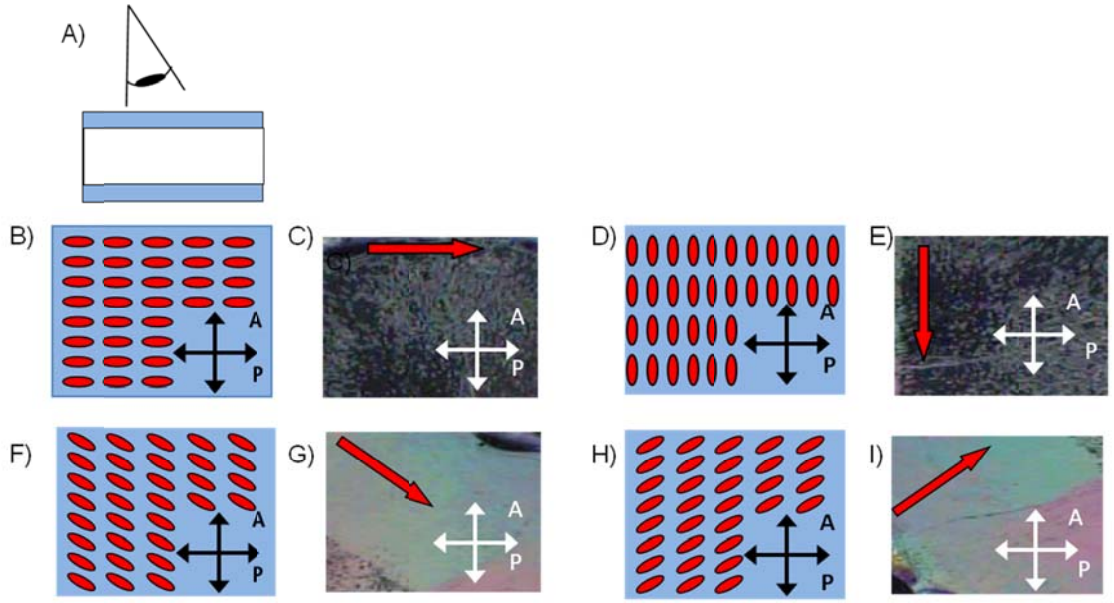

Figure 1.12: Schematic and example pictures of azimuthally aligned liquid crystals. A) Point of view, looking through a liquid crystal, down on to a substrate. B) Schematic of liquid crystal molecules azimuthally aligned with the polarizer. C) Visualization of a liquid crystal cell aligned with the polarizer D) Schematic of liquid crystal molecules azimuthally aligned with the analyzer E) Visualization of a liquid crystal cell aligned with the analyzer. F) Schematic of liquid crystal molecules azimuthally aligned 45° to the polarizer. G) Visualization of a liquid crystal cell aligned 45° to the polarizer. H) Schematic of liquid crystal molecules azimuthally aligned 45° to the analyzer. I) Visualization of a liquid crystal cell aligned 45° to the analyzer.

1.1.9 Mechanism of alignment

The mechanism of liquid crystalline alignment can be explained via two schemes: (1) physical interactions of the anisotropic molecules with the surface, or (2) molecular interactions that occur between the liquid crystals and surface. The first can be caused by alignment to grooves,[27] microscratches,[18, 38] or other topological features.[12, 39] Anisotropic liquid crystal molecules orient themselves along surface features to minimize elastic distortion energy, which then produces bulk alignment. In this theory, molecular interactions between liquid crystals and the alignment layer play no role in anchoring. In the second scheme, interactions between the surface and liquid crystals can be the result of intermolecular forces such as hydrogen bonding, dispersion forces, hydrophobic interactions, excluded volume, and steric interactions.[40] However, theses interactions are difficult to validate without molecular modeling, and physical interactions are generally considered the mode of liquid crystal alignment.

1.2 Liquid crystalline sensors

1.2.1 Liquid crystalline biosensors

Many previous examples of liquid crystal use to sense biological molecules have been demonstrated.[41-44] Liquid crystals have proven capable of responding to the presence of lipids, [45, 46] protein binding, [47,48-50] and nucleic acids.[44, 51] They provide a direct optical response without the need for specific labeling of the species of interest. Many of these systems, however, involve an intermediate interaction between the biological molecule and the liquid crystal. In some cases, this can be the target

molecule interacting with a surfactant monolayer, which then interacts with the liquid crystal. While this is not direct chemical labeling, the extra component of the sensing mechanism adds a confounding factor to the detection scheme, and removal will simplify the process. Elimination of extraneous “reporter” molecules in the reaction should lead to increased reliability and repeatability of this technique. Our objective is to combine the advantageous elimination of chemical labeling with the high sensitivity of liquid crystal detection. To apply this mechanism to DNA detection, we exploit the specific affinity of complementary strand of DNA via hybridization. Detection of a specific sequence is facile due to spontaneous complementary pairing. Current technology features premade chips where potential complements are present, waiting for detection via hybridization. Because of the native affinity of DNA for its complement, the fundamental requirement of a DNA sensor is the ability to distinguish between single and double-stranded DNA. Work by Nakata identified unique liquid crystal alignment associated with the presence of double stranded DNA in sheared, concentrated films. We intend to expand this work to less concentrated DNA films to differentiate between double and single-stranded DNA.

1.2.2 Liquid Crystalline Sensitivity

As stated previously, liquid crystals are an elastic material described by the continuum theory. This means that rather each molecule reacting individually to elastic stresses, the entire phase acts as a continuous medium. This is most readily apparent in the concept of extrapolation length, which quantifies as the distance over which that elasticity applies itself. The extrapolation length of liquid crystals can theoretically reach

up 100 μm, i.e. the effect of a perturbation the director field can be observed up to 100 μm from its point of origin[52]. Strong alignment favors return to the easy axis, necessitating a much larger anisotropy to disrupt anchoring, and a low extrapolation lenght. Weak alignment, however, requires only small surface disruptions to observe liquid crystal over a large extrapolation length.[53] The exact extrapolation length, of course, depends on the anchoring energy created by the liquid crystal/alignment layer interactions and the elasticity of the particular liquid crystal (eq 1.6). If a substrate is engineered to have a very low anchoring energy, the result is a very low energy barrier towards a shift in anchoring. Thus, single molecules on a substrate can easily shift the liquid crystal director for long extrapolation length all directions, and have an even larger effect if anchoring is further reduced.

Extrapolation length is related to both anchoring energy and elasticity, but because the elasticity of a liquid crystal is constant, for maximum extrapolation length, weak surface anchoring conditions on the alignment layer are crucial. While it may seem advantageous to minimize both the zenithal and the azimuthal anchoring energy, in fact, strong zenithal anchoring is critical to observation of azimuthal alignment. The liquid crystal molecules must remain tilted (ideally planar alignment) in order to observe azimuthal alignment. Strong zenithal alignment guarantees that any azimuthal alignment will be visible. Additionally, azimuthal anchoring energy tends to be several orders of magnitude smaller than polar anchoring; therefore higher extrapolation lengths are possible with azimuthal rather than zenithal alignment.[54, 55,56] Specifically for MBBA and 5CB, the azimuthal anchoring energy is one to two orders of magnitude smaller than the polar anchoring energy.[3, 57, 58 59] Because of the necessity of strong zenithal

alignment, and because azimuthal energy is initially lower than zenithal energy, in this work we will focus on minimizing only the azimuthal anchoring energy.

Azimuthal anchoring can be either aligned or degenerate. To clarify, degenerate azimuthal anchoring is a common state that implies that while planar anchoring is favored by the substrate$\left(\phi = \frac{\pi}{2}\right)$, there is no preferred azimuthal angle (θ) (see Figure 1.2), i.e. there is no energetic penalty for the director to assume any value of θ as long as the condition $\phi = \frac{\pi}{2}$ holds. This also implies there is virtually no energetic cost for any added surface anisotropy to induce azimuthal alignment.[60] Unfortunately, many surfaces, even those that induce degenerate alignment, possess surface memory. In this phenomena, while there is no initial bias towards liquid crystal alignment, the first layer eventually interacts with the surface in a way that causes an easy direction to be formed, essentially increasing the anchoring energy over time. To circumvent this, we aim for surface passivation, which disallows surface/liquid crystalline interactions, preventing anchoring energy creation at the solid/liquid crystalline interface. If a passivated surface is created, minimization of the anchoring energy can lead to a disruption the liquid crystalline order that could lead to a potentially infinite propagation of liquid crystalline order because of the infinitesimally small anchoring energy leads to infinitely large extrapolation length.

1.3 Two-dimensional liquid crystalline domains

A more thorough discussion of lyotropic liquid crystals is also called for. It is well documented that at sufficiently high concentrations, micelles themselves may begin to pack into more ordered structures such as hexagonal and lamellar phases[61]. While these are well categorized in three dimensions, aggregation also occurs in two dimensional systems[62]. Hemimicelles and other types of surface aggregates[63-77] certainly exist, and share many properties with their 3D counterparts. The study of surfactants has already begun to move past standard applications such as solubility, mixing, and detergency. Monolayers can also be the basis for applied surface coatings, changing the reactivity or even the utility of materials. Monolayers need not be self-assembled to be an interesting study. In fact, the study of non-equilibrium states gives opportunity for a finer of control of any layers formed. Similarly to surfactants forming three dimensional superstructures at high concentrations, at high surface concentrations, surface active agents within monolayers can also form 2D long range liquid crystalline order. Studying this order leads to greater fundamental understanding of both self and directed assembly.

1.4 References

1. Kim, M. H.; Im, S. H.; Park, O. O., Rapid fabrication of two- and three-dimensional colloidal crystal films via confined convective assembly. *Adv. Funct. Mater.* **2005,** 15, (8), 1329-1335.

2. Collings, P. J.; Hird, M., *Introduction to Liquid Crystals Chemistry and Physics*. Taylor and Francis: Bristol, PA, 1997.

3. Blinov, L. M.; Cigrinov, V. G., *Electrooptic effects in liquid crystal materials*. Springer: New York [etc.], 1996.

4. Bloss, D. F., *An Introduction to the Methods of Optical Crystallography*. Holt, Rinehart and Winston: New York, Chicago, San Francisco, Toronto, London, 1961.

5. Price, A. D.; Schwartz, D. K., Fatty-Acid Monolayers at the Nematic/Water Interface: Phases and Liquid-Crystal Alignment. *J. Phys. Chem. B* **2007,** 111, (5), 1007-1015.

6. Price, A. D.; Schwartz, D. K., Anchoring of a Nematic Liquid Crystal on a Wettability Gradient. *Langmuir* **2006,** 22, (23), 9753-9759.

7. Moon, D. W.; Kurokawa, A.; Ichimura, S.; Lee, H. W.; Jeon, I. C., Ultraviolet-ozone jet cleaning process of organic surface contamination layers. *Journal of Vacuum Science & Technology A: Vacuum, Surfaces, and Films* **1999,** 17, (1), 150-154.

8. Ye, T.; Wynn, D.; Dudek, R.; Borguet, E., Photoreactivity of Alkylsiloxane Self-Assembled Monolayers on Silicon Oxide Surfaces. *Langmuir* **2001,** 17, (15), 4497-4500.

9. Clare, B. H.; Efimenko, K.; Fischer, D. A.; Genzer, J.; Abbott, N. L., Orientations of Liquid Crystals in Contact with Surfaces that Present Continuous Gradients of Chemical Functionality. *Chem. Mater.* **2006,** 18, (9), 2357-2363.

10. Wan, J. T. K.; Tsui, O. K. C.; Kwok, H.-S.; Sheng, P., Liquid crystal pretilt control by inhomogeneous surfaces. *Physical Review E* **2005,** 72, 021711 1-4.

11. Behdani, M.; Keshmiri, S. H.; Soria, S.; Bader, M. A.; Ihlemann, J.; Marowsky, G.; Rasing, T., Alignment of liquid crystals with periodic submicron structures ablated in polymeric and indium tin oxide surfaces. *Applied Physics Letters* **2003,** 82, (16), 2553-2555.

12. Behdani, M.; Rastegar, A.; Keshmiri, S. H.; Missat, S. I.; Vlieg, E.; Rasing, T., Submicron liquid crystal pixels on a nanopatterned indium tin oxide surface. *Applied Physics Letters* **2002,** 80, (24), 4635-4637.

13. Lee, B.-w.; Clark, N. A., Alignment of Liquid Crystals with Patterned Isotropic Surfaces. *Science* **2001,** 291, (5513), 2576-2580.

14. Ogawa, K.; Mino, N.; Nakajima, K., Control of Pretilt Angles of Liquid Crystal Molecules in a Liquid Crystal Cell Using a Chemically Adsorbed Monolayer as an Alignment Film. *Japanese Journal of Applied Physics* **1990,** 29, (9), L1689-L1692.

15. Vaughn, K. E.; Sousa, M.; Kang, D.; Rosenblatt, C., Continuous control of liquid crystal pretilt angle from homeotropic to planar. *Applied Physics Letters* **2007,** 90, (19), 194102.

16. Doorn, C. Z. v., Dynamic behavior of twisted nematic liquid-crystal layers in switched fields. *Journal of Applied Physics* **1975,** 46, (9), 3738-3745.

17. Papoular, M.; Rapini, A., Ondes de Surface Dans Un Cristal Liquode Nematique. *J. Phys. Colloques* **1970,** 31, (C1), C1-27-C1-28.

18. Kim, Y. B., Atomic force microscopy of rubbed polyimide aligning films for liquid crystal displays. *Molecular Crystals and Liquid Crystals Science and Technology Section a-Molecular Crystals and Liquid Crystals* **1995,** 262, 89-98.

19. Sato, Y.; Sato, K.; Uchida, T., RELATIONSHIP BETWEEN RUBBING STRENGTH AND SURFACE ANCHORING OF NEMATIC LIQUID-CRYSTAL. *Japanese Journal of Applied Physics Part 2-Letters* **1992,** 31, (5A), L579-L581.

20. Uchida, T.; Hirano, M.; Sakai, H., Director Orientation of a Ferroelectric Liquid-Crystal on Substrates with Rubbing Treatment - The Effect of Surface Anchoring Strength *Liquid Crystals* **1989,** 5, (4), 1127-1137.

21. Vanaerle, N.; Barmentlo, M.; Hollering, R. W. J., Effect of Rubbingon the Molecular-Orientation Within Polyimide Orienting Layers of Liquid-Crystal Displays *Journal of Applied Physics* **1993,** 74, (5), 3111-3120.

22. Geary, J. M.; Goodby, J. W.; Kmetz, A. R.; Patel, J. S., The Mechanism of Polymer Alignment of Liquid-Crystal Materials. *Journal of Applied Physics* **1987,** 62, (10), 4100-4108.

23. Lee, E. S.; Vetter, P.; Miyashita, T.; Uchida, T., Orientation of Polymer-Molecules in Rubbed Alignment Layer and Surface Anchoring of Liquid-Crystals *Japanese Journal of Applied Physics Part 2-Letters* **1993,** 32, (9B), L1339-L1341.

24. Seo, D. S.; Kobayashi, S.; Kang, D. Y.; Yokoyama, H., Effects of Rubbing and Temperature-Dependence of Polar Anchoring Strength of Homogeneously Aligned Nematic Liquid-Crystal on Polyimide Langmuir-Blodgett Orientation Films *Japanese Journal of Applied Physics Part 1-Regular Papers Brief Communications & Review Papers* **1995,** 34, (7A), 3607-3611.

25. Schadt, M.; Schmitt, K.; Kozinkov, V., Surface Induced Parallel Alignment of LIquid Crystals by Linearly Polymerized Photopolymers. *Japanese Journal of Applied Physics* **1992,** 31, 2155-2164.

26. Seo, D.-S., Investigation of surface anchoring strength and pretilt angle in NLC on rubbed polythiophene surfaces with alkyl chain lengths. *Liquid Crystals*

Liquid Crystals J1 - Liquid Crystals **1999,** 26, (11), 1621-1624.

27. Berreman, D. W., Solid Surface Shape and the Alignment of an Adjacent Nematic Liquid Crystal. *Physical Review Letters* **1972,** 28, (26), 1686-1686.

28. Stohr, J.; Samant, M. G.; Cossy-Favre, A.; Diaz, J.; Momoi, Y.; Odahara, S.; Nagata, T., Microscopic origin of liquid crystal alignment on rubbed polymer surfaces. *Macromolecules* **1998,** 31, (6), 1942-1946.

29. Kim, Y. J.; Zhuang, Z.; Patel, J. S., Effect of multidirection rubbing on the alignment of nematic liquid crystal. *Applied Physics Letters* **2000,** 77, (4), 513-515.

30. Faetti, S., Azimuthal anchoring energy of a nematic liquid crystal at a grooved interface. *Physical Review A* **1987,** 36, (1), 408-410.

31. Ishihara, S.; Wakemoto, H.; Nakazima, K.; Matsuo, Y., The effect of rubbed polymer films on the liquid crystal alignment. *Liquid Crystals* **1989,** 4, (6), 669 - 675.

32. Zhuang, X.; Marrucci, L.; Shen, Y. R., Surface-Monolayer-Induced Bulk Alignment of Liquid Crystals. *Physical Review Letters* **1994,** 73, 1513-1516.

33. Iimura, Y.; Kobayashi, N.; Kobayashi, S., A New Method for Measuring the Azimuthal Anchoring Energy of a Nematic Liquid Crystal. *Japanese Journal of Applied Physics* **1994,** 33, (Part 2, No. 3B), L434.

34. Nakajima, Y.; Saito, K.; Murata, M.; Uekita, M., The Pretitlt Angle Controllable Polyimide Langmuir-Blodgett-Film for Nematic Liquid Crystals *Molecular Crystals and Liquid Crystals Science and Technology Section a-Molecular Crystals and Liquid Crystals* **1993,** 237, 111-119.

35. Ban, B. S.; Kim, Y. B., Materials and Rubbing Dependence on Azimuthal Anchoring Energy of Rubbed Polyimide Surfaces. *J. Phys. Chem. B* **1999,** 103, (19), 3869-3871.

36. Wei, X.; Hong, S.-C.; Zhuang, X.; Goto, T.; Shen, Y. R., Nonlinear optical studies of liquid crysral alignment on a rubbed polyvinyl alcohol surface. *Physical Review E* **2000,** 62, (4), 5160-5172.

37. Frank, F. C., I. Liquid crystals. On the theory of liquid crystals. *Discussions of the Faraday Society* **1958,** 25, 19-28.

38. Ruetschi, M.; Grutter, P.; Funfschilling, J.; Guntherodt, H. J., Creation of Liquid-Crystal Wave-Guides wiht Scanning Force Microscopy. *Science* **1994,** 265, (5171), 512-514.

39. Lockwood, N. A.; dePablo, J. J.; Abbott, N. L., Influence of Surfactant Tail Branching and Organization on the Orientation of Liquid Crystals at Aqueous-Liquid Crystal Interfaces. *Langmuir* **2005,** 21, (15), 6805-6814.

40. Hiltrop, K.; Stegemeyer, H., On the Orientation of Liquid Crystals by Monolayers of Amphiphilic Molecules. *Berichte der Bunsengesellschaft für physikalische Chemie* **1981,** 85, (7), 582-588.

41. Lai, S. L.; Tan, W. L.; Yang, K.-L., Detection of DNA Targets Hybridized to Solid Surfaces Using Optical Images of Liquid Crystals. *ACS Applied Materials & Interfaces*, null-null.

42. Chen, C. H.; Yang, K. L., Detection and Quantification of DNA Adsorbed on Solid Surfaces by Using Liquid Crystals. *Langmuir* **2010,** 26, (3), 1427-1430.

43. Nakata, M.; Zanchetta, G.; Buscaglia, M.; Bellini, T.; Clark, N. A., Liquid Crystal Alignment on a Chiral Surface: Interfacial Interaction with Sheared DNA Films. *Langmuir* **2008,** 24, (18), 10390-10394.

44. Price, A. D.; Schwartz, D. K., DNA Hybridization-Induced Reorientation of Liquid Crystal Anchoring at the Nematic Liquid Crystal/Aqueous Interface. *Journal of the American Chemical Society* **2008,** 130, (26), 8188-8194.

45. Price, A. D.; Schwartz, D. K., Fatty-acid monolayers at the nematic/water interface: Phases and liquid-crystal alignment. *Journal of Physical Chemistry B* **2007,** 111, (5), 1007-1015.

46. Brake, J. M.; Daschner, M. K.; Abbott, N. L., Formation and characterization of phospholipid monolayers spontaneously assembled at interfaces between aqueous phases and thermotropic liquid crystals. *Langmuir* **2005,** 21, (6), 2218-2228.

47. Clare, B. H.; Abbott, N. L., Orientations of Nematic Liquid Crystals on Surfaces Presenting Controlled Densities of Peptides: Amplification of Protein-Peptide Binding Events. *Langmuir* **2005,** 21, (14), 6451-6461.

48. Hartono, D.; Bi, X.; Yang, K.-L.; Yung, L.-Y. L., An Air-Supported Liquid Crystal System for Real-Time and Label-Free Characterization of Phospholipases and Their Inhibitors. *Advanced Functional Materials* **2008,** 18, (19), 2938-2945.

49. Brake, J. M.; Daschner, M. K.; Luk, Y.-Y.; Abbott, N. L., Biomolecular Interactions at Phospholipid-Decorated Surfaces of Liquid Crystals. *Science* **2003,** 302, (5653), 2094-2097.

50. Brake, J. M.; Abbott, N. L., Coupling of the orientations of thermotropic liquid crystals to protein binding events at lipid-decorated interfaces. *Langmuir* **2007,** 23, (16), 8497-8507.

51. Bi, X.; Huang, S.; Hartono, D.; Yang, K.-L., Liquid-crystal based optical sensors for simultaneous detection of multiple glycine oligomers with micromolar concentrations. *Sensors and Actuators B: Chemical* **2007,** 127, (2), 406-413.

52. Bai, Y.; Abbott, N. L., Recent Advances in Colloidal and Interfacial Phenomena Involving Liquid Crystals. *Langmuir* **2011,** 27, (10), 5719-5738.

53. Rasing, T.; I., M., *Surfaces and Interfaces of Liquid Crystals*. Springer: New York, 2004.

54. Fonseca, J. G.; Galerne, Y., Simple method for measuring the azimuthal anchoring strength of nematic liquid crystals. *Applied Physics Letters* **2001,** 79, (18), 2910-2912.

55. Murauski, A.; Chigrinov, V.; Muravsky, A.; Yeung, F. S.-Y.; Ho, J.; Kwok, H.-S., Determination of liquid-crystal polar anchoring energy by electrical measurements. *Physical Review E* **2005,** 71, (6), 061707.

56. Lee, S. H.; Yoon, T. H.; Kim, J. C., Determination of azimuthal anchoring energy in a twisted nematic liquid crystal. *Physical Review E* **2005,** 72, (6).

57. Sonin, A. A., *The Surface Physics of LIquid Crystals*. Gordon and Breach Publishers: New York, 1995.

58. Dunmar, D.; Fukuda, A.; Luckhurst, G., *Physical Properties of Liquid Crystals: Nematics*. INSPEC, THe Institution of Electrical Engineers: London, 2001.

59. Jerome, B., Surface Effects and Anchoring in Liquid-Crystals. *Reports on Progress in Physics* **1991,** 54, (3), 391-451.

60. Fukuda, J.-i.; Yoneya, M.; Yokoyama, H., Consistent numerical evaluation of the anchoring energy of a grooved surface. *Physical Review E* **2009,** 79, (1), 011705.

61. Luzzati, V.; Husson, F., STRUCTURE OF LIQUID-CRYSTALLINE PHASES OF LIPID-WATER SYSTEMS. *J. Cell Biol.* **1962,** 12, (2), 207-&.

62. Blanchette, C. D.; Lin, W. C.; Orme, C. A.; Ratto, T. V.; Longo, M. L., Domain nucleation rates and interfacial line tensions in supported bilayers of ternary mixtures containing galactosylceramide. *Biophysical Journal* **2008,** 94, (7), 2691-2697.

63. Fuerstenau, D. W., Streaming Potential Studies on Quartz in Solutions of Aminium Acetates in Relation to the Formation of Hemi- micelles at the Quartz-Solution Interface. *The Journal of Physical Chemistry* **1956,** 60, (7), 981-985.

64. Gu, T.; Rupprecht, H., Hemimicelle shape and size. *Colloid & Polymer Science* **1990,** 268, (12), 1148-1150.

65. Cain, N.; Van Bogaert, J.; Gin, D. L.; Hammond, S. R.; Schwartz, D. K., Self-organization of a wedge-shaped surfactant in monolayers and multilayers. *Langmuir* **2007,** 23, (2), 482-487.

66. Ducker, W. A.; Wanless, E. J., Surface-aggregate shape transformation. *Langmuir* **1996,** 12, (24), 5915-5920.

67. Fuerstenau, D. W., Equilibrium and nonequilibrium phenomena associated with the adsorption of ionic surfactants at solid-water interfaces. *Journal of Colloid and Interface Science* **2002,** 256, (1), 79-90.

68. Fuerstenau, D. W.; Colic, M., Self-association and reverse hemimicelle formation at solid-water interfaces in dilute surfactant solutions. *Colloids and Surfaces a-Physicochemical and Engineering Aspects* **1999,** 146, (1-3), 33-47.

69. Grant, L. M.; Ducker, W. A., Effect of substrate hydrophobicity on surface-aggregate geometry: Zwitterionic and nonionic surfactants. *Journal of Physical Chemistry B* **1997,** 101, (27), 5337-5345.

70. Manne, S.; Cleveland, J. P.; Gaub, H. E.; Stucky, G. D.; Hansma, P. K., Direct Visualization of Surfactant Hemimicelles by Force Microscopy of the Electrical Double-Layer *Langmuir* **1994,** 10, (12), 4409-4413.

71. Manne, S.; Gaub, H. E., Molecular-Organization of Surfactants at Solid-Liquid Interfaces *Science* **1995,** 270, (5241), 1480-1482.

72. Manne, S.; Schaffer, T. E.; Huo, Q.; Hansma, P. K.; Morse, D. E.; Stucky, G. D.; Aksay, I. A., Gemini surfactants at solid-liquid interfaces: Control of interfacial aggregate geometry. *Langmuir* **1997,** 13, (24), 6382-6387.

73. Nelson, M.; Cain, N.; Taylor, C. E.; Ocko, B. M.; Gin, D. L.; Hammond, S. R.; Schwartz, D. K., Periodic arrays of interfacial cylindrical reverse micelles. *Langmuir* **2005,** 21, (22), 9799-9802.

74. Patrick, H. N.; Warr, G. G.; Manne, S.; Aksay, I. A., Surface micellization patterns of quaternary ammonium surfactants on mica. *Langmuir* **1999,** 15, (5), 1685-1692.

75. Wanless, E. J.; Davey, T. W.; Ducker, W. A., Surface aggregate phase transition. *Langmuir* **1997,** 13, (16), 4223-4228.

76. Wanless, E. J.; Ducker, W. A., Weak influence of divalent ions on anionic surfactant surface-aggregation. *Langmuir* **1997,** 13, (6), 1463-1474.

77. Wolgemuth, J. L.; Workman, R. K.; Manne, S., Surfactant aggregates at a flat, isotropic hydrophobic surface. *Langmuir* **2000,** 16, (7), 3077-3081.

Chapter 2

Polar and Azimuthal Alignment of a Nematic Liquid Crystal by Alkylsilane Self-Assembled Monolayers as Affected by Chain-Length and Mechanical Rubbing

Alkylsilane self-assembled monolayers (SAMs) on oxide substrates can be used as liquid crystal alignment layers. We have studied the effect of alkyl chain length, photolytic degradation, and mechanical rubbing on polar and azimuthal liquid crystal anchoring. Chain length was studied with SAMs that had been photolytically degraded in order to produce a gradient of surface properties, as well as SAMs deposited from varying discrete alkyl chain lengths. Alkyl chain length varied between 1 and 18 carbons. In both gradient and discrete SAMs, the liquid crystal transition between homeotropic and tilted corresponded to increasing wettability of the SAMs. An offset between the transition contact angle for photolytically degraded SAMs vs. discrete SAMs suggested that layer thickness and composition are more relevant than wettability for liquid crystal alignment. Mechanical rubbing proved capable of inducing azimuthal alignment, as well as slightly increasing polar tilt. This induced tilt was most easily visualized near the homeotropic to tilted transition, e.g., unaligned SAMs of alkyl chain length 5 shifted from homeotropic alignment to tilted transition upon rubbing.

2.1 Introduction

The epitaxial alignment and of liquid crystals to surface grooves is a well-studied phenomenon.[1] Both polar and azimuthal liquid crystal anchoring are of significant interest; changing either provides information about a substrate's surface properties, including topography and chemistry. The extreme sensitivity of liquid crystals to underlying surface conditions is unparalleled. Subtleties including the tilt of Langmuir-Blodgett films,[2-4] switching of photoisomerizable compounds[5,6] peptides adsorption,[7-11] and DNA adsorption[5, 12, 13] have all been detected via liquid crystal/substrate interactions.

Detection is typically accomplished by identifying the liquid crystal textures that correspond to alignment layer properties. This generally manifests itself in the form of a shift of the polar or azimuthal anchoring angle, or the onset of azimuthal alignment in a previously degenerate sample. Detection is also possible by monitoring anchoring energy. Measuring anchoring energy is a more involved technique than observation of liquid crystal textures via polarization; therefore, we will focus on visual cues from birefringence and liquid crystalline textures to identify surface interactions. To accomplish this, we must first create alignment layers that produce known liquid crystal textures. These are formed by treating substrates with empirically developed techniques to impart the desired anchoring conditions: in this case, tilted polar alignment. One common class of alignment mechanism is contact-based, i.e. rubbing. Rubbing is thought to either cause small grooves in a substrate's surface, or to align surface molecules.[14, 15] Self-assembled monolayers have also been shown to strongly influence liquid crystal alignment.[11, 16-19] The attachment chemistries of monolayers

vary to interact with each particular type of substrate. Gold, for example, utilizes thiol chemistry as an attachment mechanism. Oxide surfaces (e.g. glass, fused silica, or silicon wafers) use silane chemistry. Silane chemistry is used in this work; see Chapter 5.1.1 for a more in-depth discussion of silane SAM formation.

Many research groups have designed experiments to further understand the interactions between liquid crystals and alignment layers, including creating gradients,[16, 20] patterning, [21-25] and blended substrates.[26, 27] Surface modification allows close observation and comparison of surface patterns to liquid crystal texture, thus providing insight into the mechanisms liquid crystal anchoring. In the case of strong anchoring, liquid crystals closely mimic surface patterning. Conversely, with weak anchoring, a homogenous liquid crystal pattern can form, effectively averaging out any irregularities. Transitional regions in an alignment layer provide insight into the elasticity of liquid crystals by comparing the transition of the substrate to the anchoring transition of the liquid crystal. Subtle modifications in an alignment layer such as monolayer density,[28-31] blending,[18, 32] irradiation,[33,34] substrate corrugation,[35] and oblique degradation[33, 36] affect both polar and azimuthal anchoring. When used to monitor surface changes, liquid crystals become an extremely sensitive probe of surface properties, even detecting surface features invisible to AFM, ellipsometry, and FTIR[16, 37, 38].

More detailed literature review reveals the extent of the ability of liquid crystal interactions to reveal subtle, molecular-level changes. Ban and Kim demonstrated that a change in the length of polymeric side chains in an alignment layer affects the liquid crystal tilt angle (pretilt). Additionally, they find that the type, and even the extent of rubbing affects pretilt[40]. Nakajima and Uekita explore the mechanism of alkyl chain

density and its effect on pretilt, and find that decreasing density of alkyl chains shifts anchoring to lower pretilt.[46] Drawhorn and Abbot discovered that homogenous alkanethiol SAMs on gold induce planar alignment regardless of chain length; however, certain mixtures of chain length induce homeotropic alignment.[17] The mechanism in this case was interpreted to be similar to the model for homeotropic alignment induced by DMOAP (N,N-dimethyl-n-octadecyl-3-aminopropyltri-methoxysilyl chloride) mononalyers.[47] Similarly, Gupta and Abbot found that odd numbered alkyl chains impart azimuthal alignment orthogonal to the alignment caused by even numbered alkyl chains in alkanethiol SAMs.[18] Crawford et al. also demonstrated that chain length of an aliphatic acid affects liquid crystal anchoring, bringing on a planar to homeotropic transition with increasing chain length.[48] Seo confirmed the demonstration that rubbing technique affects tilt, more specifically that contacting the surface not only affects liquid crystal orientation, but that the liquid crystal detects the pressure and number of brushing strokes.[49]

Again, all of these studies demonstrate that the subtle differences in an alignment layer have are greatly magnified by liquid crystal alignment. The inherent elasticity of liquid crystalline materials dictates that even minute changes in an alignment layer propagate from the surface throughout the bulk. This epitaxial transfer of surface alignment to the bulk effectively amplifies surface effects, creating macroscopically visible cues to molecular-level interactions. This amplification, however, also creates the major problem associated with forming alignment layers. The amplification of any surface irregularities leads to extremely low tolerance for any defects in an alignment layer. Rubbing is an extremely high throughput method, and

thus suitable for production capacity of applications such as display technology. It, however, also creates dust and static electricity, and both impart defects to the alignment layer.[15, 39-45] Many of the noncontact methods mentioned above are being explored for alignment layer purposes to eliminate the defect formation associated with rubbing, while still creating strong, uniform liquid crystal alignment. Alignment via self-assembled alignment layers is a logical step for noncontact alignment of liquid crystal films.

While the previously described alkanethiol SAMs are dissimilar to the alkylsilane alignment layers used in this work, it is unlikely that the attachment mechanism has any major effect on liquid crystal interactions due to the monolayer thickness [50]. In this work, we explore the effect of alkyl chain length on polar and azimuthal liquid crystal anchoring. Azimuthal anchoring is imparted by the rubbing technique. We have covalently attached alkyl silane monolayers to glass surfaces. These were created with either discrete alkyl chain lengths (C1-C18), or a C18 (OTS, or octradecyltrietyhoxysilane) SAM was photolytically degraded in order to study short alkyl chains in an additional configuration. We demonstrate that alkyl chain length is directly related to the polar pretilt of the liquid crystal, in addition to showing that the subtle changes from rubbing not only affect pretilt, but that rubbing can actually *create* pretilt. See Chapter 5 for experimental details.

2.2 Results and discussion

2.2.1 Polar anchoring dependence on monolayer thickness

Figure 2.1 shows polarized microscope images of hybrid-aligned nematic (HAN) cells prepared using a photolytically-degraded OTS SAMs (Figure 2.1a), HAN cells prepared using un-degraded shorter SAMs of varying chain lengths (Figures 2.1b-g), and clean glass (Figure 2.1h). Hybrid aligned cells have an un-degraded OTS SAM on one side, and either a degraded or discrete alkyl chain length SAM on the other. For more details, see Chapter 5.1. UV irradiation in the presence of oxygen gas generates short-lived oxygen containing radicals that degrade OTS SAMs by cleaving carbon-carbon bonds[16, 37, 38, 51, 52]. Previous work suggests that it is the outermost C-C bond is preferentially cleaved, resulting in sequential shortening of each chain[17,37, 53, 54]. Our group previously demonstrated via AFM that the degraded, gradient SAMs were laterally homogeneous over length scales probed by the AFM tip, i.e. ≥5 nm [16]. If a mechanism that cleaved a C-Si, Si-O, or O-C bond dominated, bare islands within the monolayers would have been observed. Thus, it is reasonable to hypothesize that the gradient surfaces described above are characterized by a gradual decrease in average chain length, and that the polar anchoring transition is directly related to the variation in film thickness caused by the shortening chain lengths.

2.2.2 Homeotropic to planar transition

As reported previously, a relatively abrupt transition from homeotropic anchoring to nearly planar polar anchoring is observed with increasing degradation along a gradient SAM.[16,20] This appears in Figure 2.1a as a transition from optical extinction (black) on the left side of the sample to colors on the right associated with large birefringence (washed out greens and pinks). The birefringence was estimated with comparison with the Michel-Levy diagram (Figure 1.9). In order to verify the relationship between tilt and chain length, SAMs were deposited with discrete chain lengths of 1, 2, 3, 4, 5, 6, 10, and 18. Figure 2.1b-g demonstrates that similar to the irradiated SAMs behavior is observed as a function of chain length for shorter, un-degraded SAMs. For chain lengths greater than five (Figure 2.1b,c), no light transmission is observed (extinction) as a result of homeotropic anchoring, while for shorter chains (Figure 2.1d-g), the birefringence is consistent with tilted or planar anchoring. One would expect that the birefringence colors would follow the patterns laid out by the Michel-Levy diagram[55] for Figure 2.1b-g, but that only holds true if all liquid crystal cells are the same thickness. While each liquid crystal cell was controlled for thickness, there was substantial variation between sample cells ($\pm$ 5μm). Instead, for each individual cell we measure retardation and cell thickness, and use this information to calculate birefringence. Observed interference colors are based on retardation rather than birefringence, explaining the deviation from the patterns observed in the Michel-Levy diagram. Once birefringence was calculated, there was a clear relationship between pretilt angle and alkyl chain length, as birefringence is directly related to liquid crystal tilt angle (See Chapter 5.1.7).

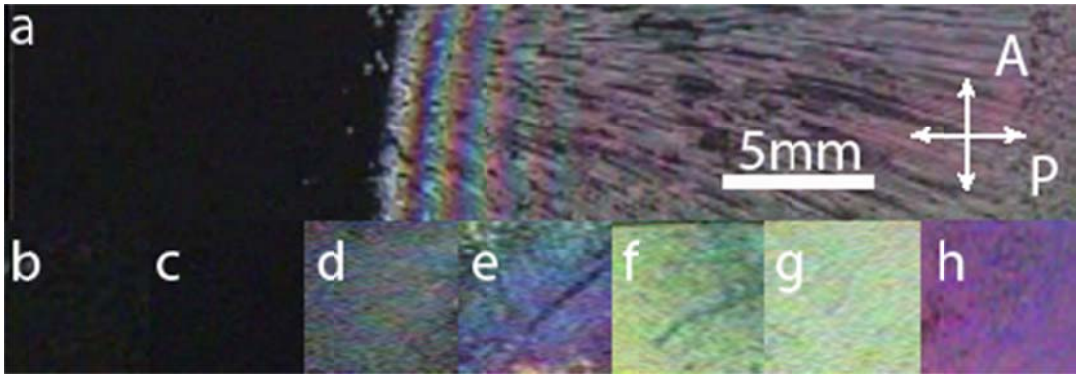

Figure 2.1: Polarized microscope images of HAN cells; the analyzer and polarizer are oriented as shown by the white arrows. The surfaces of interest described are: (a) photolytically-degraded OTS (C18) SAM with a continuous gradient of surface properties (least degraded at left, most degraded at right), where degradation indicates a shortening of alkyl chain length (b) C6 SAM, (c) C5 SAM, (d) C4 SAM, (e) C3 SAM, (f) C2 SAM, (g) C1 SAM, (h) glass

Observations of changes in liquid crystal polar alignment suggest that the interfacial free energies associated with homeotropic and tilted/planar anchoring evolve systematically with UV exposure (degradation) and/or chain length. It is therefore interesting to compare the surface anchoring with other measures of interfacial free energy, such as wettability. Figure 2.2 shows the correlation between contact angle and alkyl degradation (Figure 2.2a) and alkyl chain length (Figure 2.2b). The cosine of the contact angle decreases systematically with distance from the UV source or increasing chain length, suggesting at least a qualitative correlation between wettability and liquid crystal anchoring. This is supported by Young's equation (Chapter 5.1.8), which links surface energy directly to the contact angle[56].

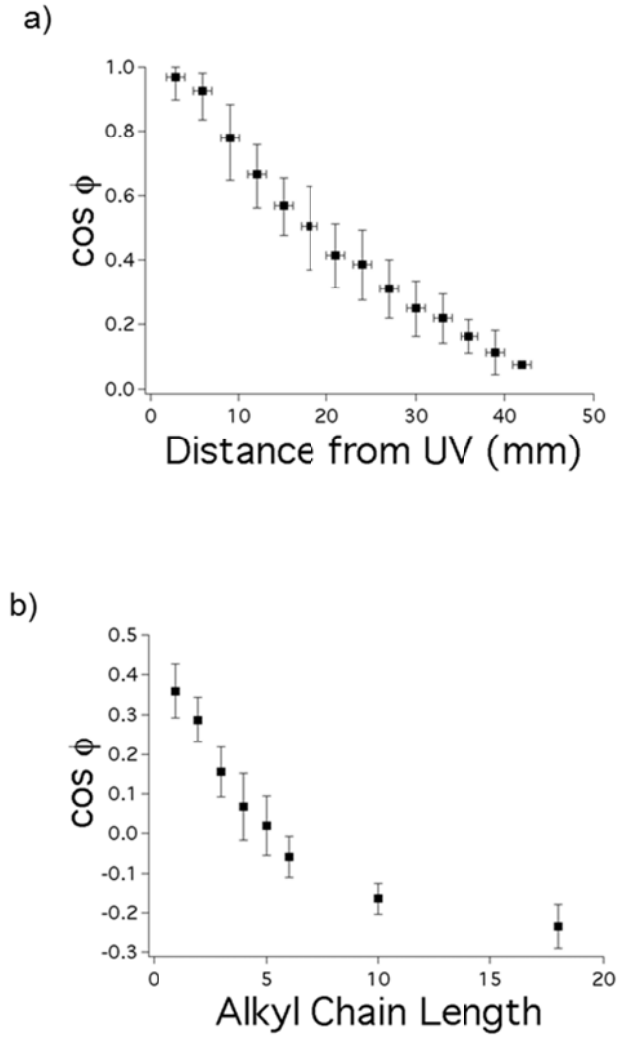

Figure 2.2: Cosine of the contact angle of water measured on (a) a photolytically-degraded gradient surface as a function of distance from the UV source, and (b) un-degraded SAMs as a function of alkyl chain length. Both indicate an increase in wettability with decreasing alkyl chain length.

2.2.3 Comparison of gradient and discrete self-assembled monolayers

In order to compare the gradient SAM and discrete SAMs directly, it is necessary to fine a common parameter, in this case, birefringence, as the alkyl chain lengths are not exactly known in the irradiated SAMs. It is possible to collapse the measured birefringence data by plotting it against $\cos\phi$ for both substrates(Figure 2.3). As expected from the qualitative observations of birefringence, both types of alignment layers exhibit an abrupt birefringence transition (from homeotropic to tilted) as wettability increased. However, when comparing discrete and degraded SAMs, there is a significant offset between the critical transition values of $\cos\phi$, suggesting that water and liquid crystal phase probe somewhat different chemical or structural surface properties. This is not surprising, given the vastly different chemical structures of water and 5CB (see Figure 1.7 for the structure of 5CB).

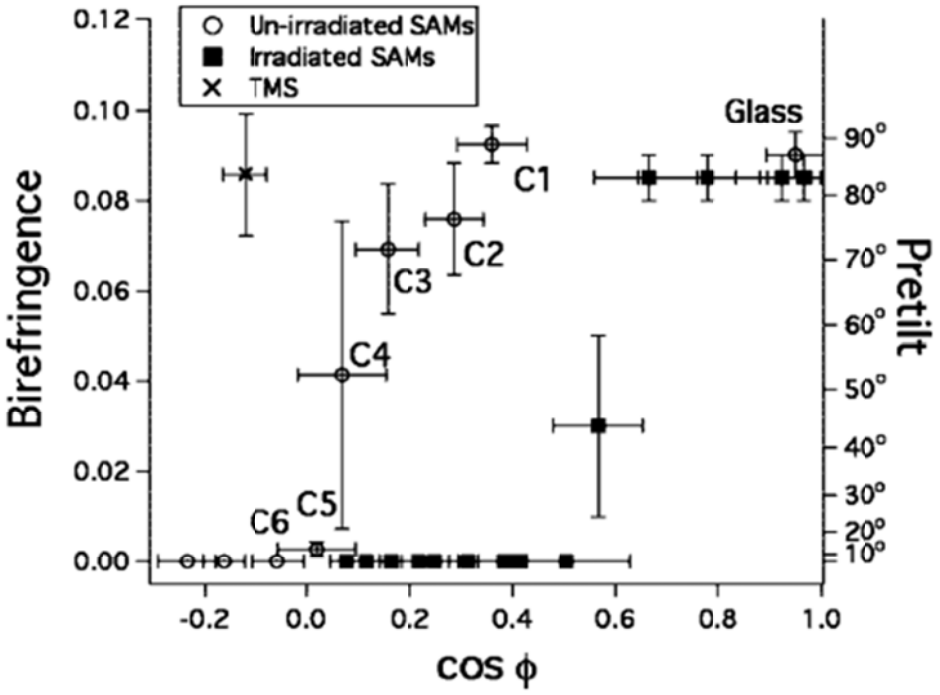

Figure 2.3: Direct comparison of birefringence vs. wettability for discrete chain length and degraded SAMs. The optical birefringence is directly related to the polar liquid crystal anchoring angle (pretilt).

The C4 SAM is particularly interesting because it falls directly within the transitional region between homeotropic and tilted anchoring. In Figure 2.3, the uncertainty of the birefringence for C4 samples is very large. This uncertainly is calculated as the standard deviation of values measured for six independent samples. The values for C4 are evenly distributed within a large birefringence range. This supports the hypothesis that the transition from homeotropic to tilted anchoring is extremely sensitive to sample variation, and that small effects can have a large impact on birefringence/pretilt. This is consistent with the idea that the transition from homeotropic to planar is extremely abrupt, and a discontinuous transition.[16] While all six samples were ostensibly prepared identically, there is large variation in birefringence.

The sensitivity of the transition of the C4 SAM is consistent with the birefringent transition of the gradient SAMs. Sample variation showed a slight lateral shift on the transition region of the irradiated samples. While this variation can also be explained by slight variations in sample thicknesses (the individual thicknesses of samples were measured, cells with identical thicknesses were not feasible), it is also likely that sample to sample variation also contributed to the shift in the liquid crystal anchoring transition region.

2.2.4 Trimethylsiloxane (TMS) SAMs and birefringence

The comparison to TMS substrates again confirms that liquid crystal anchoring is affected by more factors than simply wettability. Though only one methyl group thick, and thus similar to the C1 monolayers, the TMS coated substrates were much more hydrophobic than the C1 monolayers, with $\phi = 97° \pm 2°$, or $\cos\phi = -0.12$ (Figure 2.3). The pretilt of C1 and TMS SAMs was similar, but the wettability of the C1 substrates is much higher than that of TMS. The difference in wettability is presumably due to the increased lateral density of methyl groups within the monolayer. While the alkylsilane SAMs contain a single alkyl chain, TMS consists of three methyl groups per molecule. In contrast to alkylsilane SAMS, TMS SAMs have an extremely low wettability, but still give a high birefringence (Figure 2.3). This again indicates more affects liquid crystal alignment than simply surface wetting, and suggests that the thickness of the monolayer can come into play when predicting liquid crystal tilt.

2.2.5 Wettability/Surface roughness of transition regions

The anchoring behavior as a function of chain length for discrete SAMs is qualitatively consistent with the view that monolayer thickness is an approximate probe for liquid crystal pretilt. In particular, the abrupt change from homeotropic to tilted anchoring for C4 and irradiated SAMs supports this conjecture. In both cases, the anchoring transition is correlated with a change in the wettability of water. This is supported by previous work by our group[16] and others.[57] However, the specific contact angles associated with the anchoring transition differ significantly: ~55˚ for gradient SAMs and ~85˚ for discrete SAMs. This may be due to the fact that the dispersion in

chain length is expected to be significant for the degraded SAMs. Assuming random photolytic cleavage of chains (Poisson statistics), the reduction of a C18 SAM by an average of 14 methylene units would result in a dispersion of ±3.7 units giving chain lengths of 4±4. We speculate that this large variation in chain length at the molecular level leads to a significant reduction of the contact angle relative to the uniform discrete SAMs[58-60].

2.2.6 Depth sensitivity of wetting

For discrete SAM substrates, the anchoring behavior as a function of chain length suggests that the influence of the underlying glass substrate on liquid crystal phase becomes influential when the barrier SAM is four methylene/methyl units thick. This particular thickness corresponds to the results of studies on the depth sensitivity of wetting. Bain and Whitesides[61] examined the contact angle of water and hexadecane on mercapto-ether monolayers on gold. They found that if an oxygen atom was embedded more than four carbons deep in an alkyl chain, it no longer affected the contact angle of water at the surface of the monolayer and the contact angle approached that of alkanethiols on gold. Hexadecane, which presumably only interacts with the monolayer via dispersion reactions, rather than hydrogen bonding with the embedded oxygen atom, is shown to be constant with varied depth of an oxygen atom. Thus, any effects due to wetting were shown to be the result of interactions with the outermost few angstroms of monolayers and the wetting substance (in our case liquid crystals) it is interacting with, indicating that substrate/liquid crystal interactions only occur below a critical monolayer thickness.

2.2.7 Azimuthal anchoring due to mechanical rubbing

In situations where un-rubbed substrates induced tilted or planar anchoring, rubbing was found to cause strong azimuthal alignment along the rubbing direction. For significantly longer or less degraded SAMs, rubbing had no noticeable effect. Previous studies suggested, however, that even long-chain SAMs retain a memory of rubbing. Walba et al. demonstrated that rubbed OTS SAMs induced azimuthal alignment for a liquid crystal in the smectic C phase.[62] The additional sensitivity to perturbations in the monolayer could be due to the inherent pretilt of the smectic C phase (see Figure 1.4). There is presumably an extremely low energy barrier for ordered azimuthal alignment as long as the polar pretilt conditions required by the smectic C phase are met.

We observe that rubbing has only a secondary effect with respect to polar anchoring, but that it creates azimuthal alignment effectively in the absence of homeotropic alignment.[62] The degree of alkyl chain length degradations also directly affects the impact of mechanical rubbing. For gradient surfaces, azimuthal alignment occurs only in the region of rapidly increasing birefringence (Figure 2.4 a,b), which is presumed to be chain lengths from 1-4. Far to the left of the transition region, where the degradation is less, the homeotropic anchoring (presumably chain lengths 6 or longer) is not affected by rubbing, and optical extinction is observed regardless of sample orientation. Similarly, far to the right of the transition region, rubbing has no effect, presumably because the surface is virtually bare of any alkyl chains that could impart bias from the rubbing due to extensive degradation. Within the transition region, however, there is strong azimuthal alignment in the rubbing direction, thus we observed extinction in the rubbed region when the rubbing direction is aligned with the polarizer.

Because it has been demonstrated earlier in the text that contact angle measurements are not directly relatable between discrete and degraded SAMs, approximate chain lengths for degraded SAMs were determined based on birefringence.

2.2.8 Rubbing creates polar alignment near transition region

The location of the transition from homeotropic to planar shifts slightly towards the left of a degraded sample, which is visible in Figure 2.4b. This indicates that near the transition point, rubbing can induce tilted anchoring in a homeotropic domain. For SAMs with slightly longer (or less degraded) alkyl chains, rubbing caused a transformation from homeotropic to aligned tilted anchoring. This effect was subtle, however, and only observed very close to the transition. This effect is more easily visualized in the discrete SAMs described below. In all of the samples in Figure 2.4, the upper half of the substrate was shielded from rubbing, while the bottom half of the substrate was rubbed to induce azimuthal alignment. As with the gradient surface, when the chain length of discrete SAMs is large compared to the transition chain length, rubbing has no effect, e.g. C6 SAMs induce uniformly homeotropic anchoring regardless of rubbing (Figure 2.4 c,d). Homeotropic anchoring was also observed for C10 and C16 SAMs. However, for C5 SAMs, while un-rubbed regions induce homeotropic anchoring, rubbing results in weak birefringence. C1 through C4 SAMs are all aligned by rubbing, while no effect is observed on the control substrate, glass. The lack of alignment on rubbed glass demonstrates that azimuthal alignment on SAMs is directly related to the effect of rubbing on a SAM, not an artifact (e.g. due to contamination from the brush). While an attempt at quantitative measurement of birefringence increase was attempted for all chain lengths, all increases were within

experimental error for chain lengths 1-4. Therefore, the visible birefringence increase associated with the transition from homeotropic to tilted anchoring (extinction to birefringent) was the only transition that could be reliably observed.

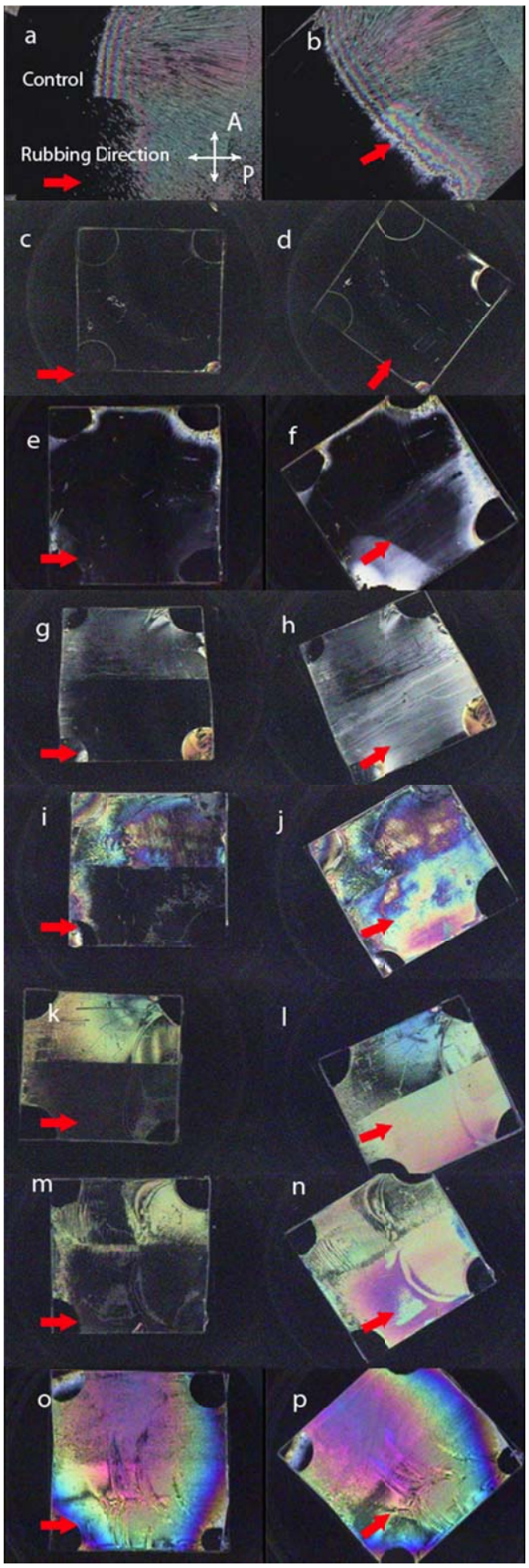

croscope
olarizers)
various
m half of
anically-
arrows.
was not
control.
esents a
s on the
arallel to
on the
fset from
(a, b)
S SAM
AM, (e, f)
C3 SAM,
AM(o, p)

2.3 Conclusions

Both discrete and gradient monolayers exhibited an abrupt transition from homeotropic to tilted alignment, suggesting that the transition may correspond to a critical monolayer thickness. Both types of monolayer showed a direct correlation between wettability and chain length/degradation; however, there was an offset in the critical contact angles for the transition between the two types of substrate. This suggested that while wettability can provide a qualitative guide to the surface energy associated with liquid crystal anchoring, the liquid crystal actually responds to a subtly different surface property than is measured by contact angle. One possible difference involves the surface heterogeneity caused by the statistical nature of photolytic degradation. Mechanical rubbing was shown to induce azimuthal alignment only in the transition region of degraded SAMs and in chain lengths $\leq$C5. In most cases, therefore, azimuthal alignment only occurred on substrates where tilt was observed in the absence of rubbing. However, for alignment layers very close to the transition, rubbing can induce tilt; the C5 SAM is a notable example. Thus, it is apparent that liquid crystals prove to be an extremely sensitive surface probe. They have been proven to react to azimuthal stimulus differently, depending on substrate alkyl chain length. Polar tilt is also substantially affected by substrate chain length, likely due to long-range interactions between the liquid crystal and underlying substrate.

2.4 References

1. Berreman, D. W., Solid Surface Shape and the Alignment of an Adjacent Nematic Liquid Crystal. Physical Review Letters **1972,** 28, (26), 1686-1686.

2. Fang, J. Y.; Gehlert, U.; Shashidar, R.; Knobler, C. M., Imaging the azimuthal tilt order in monolayers by liquid crystal optical amplification. Langmuir **1999,** 15, (2), 297-299.

3. Alexe-Ionescu, A. L.; Barbero, G.; Ignatov, A.; Miraldi, E., Surface transitions in nematic liquid crystals oriented with Langmuir-Blodgett films. Applied Physics A: Materials Science & Processing **1993,** 56, (5), 453-455.

4. Fazio, V. S. U.; Komitov, L.; Lagerwall, S. T., Alignment of nematic liquid crystals on mixed Langmuir-Blodgett monolayers. Thin Solid Films **1998,** 329, 681-685.

5. Price, A. D.; Ignes-Mullol, J.; Angels Vallve, M.; Furtak, T. E.; Lo, Y.-A.; Malone, S. M.; Schwartz, D. K., Liquid crystal anchoring transformations induced by phase transitions of a photoisomerizable surfactant at the nematic/aqueous interface. Soft Matter **2009,** 5, (11), 2252-2260.

6. Aronzon, D.; Levy, E. P.; Collings, P. J.; Chanishvili, A.; Chilaya, G.; Petriashvili, G., rans-cis isomerization on an azoxybenzene liquid crystal. Liquid Crystals **2007,** 34, 707-718.

7. Clare, B. H.; Guzman, O.; dePablo, J.; Abbott, N. L., Anchoring Energies of Liquid Crystals Measured on Surfaces Presenting Oligopeptides. Langmuir **2006,** 22, (18), 7776-7782.

8. Kim, S. R.; Abbott, N. L., Rubbed Films of Functionalized Bovine Serum Albumin as Substrates for the Imaging of Protein–Receptor Interactions Using Liquid Crystals. Advanced Materials **2001,** 13, (19), 1445-1449.

9. Hartono, D.; Xue, C.-Y.; Yang, K.-L.; Yung, L.-Y. L., Decorating Liquid Crystal Surfaces with Proteins for Real-Time Detection of Specific Protein-Protein Binding. Advanced Functional Materials **2009,** 19, (22), 3574-3579.

10. Gupta, V. K.; Skaife, J. J.; Dubrovsky, T. B.; Abbott, N. L., Optical Amplification of Ligand-Receptor Binding Using Liquid Crystals. Science **1998,** 279, (5359), 2077-2080.

11. Luk, Y.-Y.; Tingey, M. L.; Hall, D. J.; Israel, B. A.; Murphy, C. J.; Bertics, P. J.; Abbott, N. L., Using Liquid Crystals to Amplify Protein-Receptor Interactions: Design of Surfaces with Nanometer-Scale Topography that Present Histidine-Tagged Protein Receptors. Langmuir **2003,** 19, (5), 1671-1680.

12. Price, A. D.; Schwartz, D. K., DNA Hybridization-Induced Reorientation of Liquid Crystal Anchoring at the Nematic Liquid Crystal/Aqueous Interface. J. Am. Chem. Soc. **2008,** 130, (26), 8188-8194.

13. Chen, C. H.; Yang, K. L., Detection and Quantification of DNA Adsorbed on Solid Surfaces by Using Liquid Crystals. Langmuir **2010,** 26, (3), 1427-1430.

14. Seo, D.-S.; Hwang, L.-Y.; Lee, B.-H. In A study on mechanism of pretilt angle generation in nematic liquid crystal for rubbed polyimide surfaces, Properties and Applications of Dielectric Materials, 1997., Proceedings of the 5th International Conference on, 1997; Hwang, L.-Y., Ed. 1997; pp 946-948 vol.2.

15. Stohr, J.; Samant, M. G.; Cossy-Favre, A.; Diaz, J.; Momoi, Y.; Odahara, S.; Nagata, T., Microscopic origin of liquid crystal alignment on rubbed polymer surfaces. Macromolecules **1998,** 31, (6), 1942-1946.

16. Price, A. D.; Schwartz, D. K., Anchoring of a Nematic Liquid Crystal on a Wettability Gradient. Langmuir **2006,** 22, (23), 9753-9759.

17. Drawhorn, R. A.; Abbott, N. L., Anchoring of Nematic Liquid-Crystals on Self-Assembled MOnolayers Formed from Alkanethiols on Semitransparent Films of Gold. Journal of Physical Chemistry **1995,** 99, (45), 16511-16515.

18. Gupta, V. K.; Abbott, N. L., Azimuthal anchoring transition of nematic liquid crystals on self-assembled monolayers formed from odd and even alkanethiols. Physical Review E **1996,** 54, (5), R4540-R4543.

19. Park, S. J.; Jang, C. H., Using liquid crystals to detect DNA hybridization on polymeric surfaces with continuous wavy features. Nanotechnology **2010,** 21, (42), 7.

20. Clare, B. H.; Efimenko, K.; Fischer, D. A.; Genzer, J.; Abbott, N. L., Orientations of Liquid Crystals in Contact with Surfaces that Present Continuous Gradients of Chemical Functionality. Chem. Mater. **2006,** 18, (9), 2357-2363.

21. Lee, B.-W.; Clark, N. A., Alignment of Liquid Crystals with Patterned Isotropic Surfaces. Science **2001,** 291, (5513), 2576-2580.

22. Gupta, V. K.; Abbott, N. L., Design of Surfaces for Patterned Alignment of Liquid Crystals on Planar and Curved Substrates

10.1126/science.276.5318.1533. Science **1997,** 276, (5318), 1533-1536.

23. Behdani, M.; Keshmiri, S. H.; Soria, S.; Bader, M. A.; Ihlemann, J.; Marowsky, G.; Rasing, T., Alignment of liquid crystals with periodic submicron structures ablated in polymeric and indium tin oxide surfaces. Appl. Phys. Lett. **2003,** 82, (16), 2553-2555.

24. Behdani, M.; Rastegar, A.; Keshmiri, S. H.; Missat, S. I.; Vlieg, E.; Rasing, T., Submicron liquid crystal pixels on a nanopatterned indium tin oxide surface. Appl. Phys. Lett. **2002,** 80, (24), 4635-4637.

25. Wan, J. T. K.; Tsui, O. K. C.; Kwok, H.-S.; Sheng, P., Liquid crystal pretilt control by inhomogeneous surfaces. Physical Review E **2005,** 72, 021711 1-4.

26. Vaughn, K. E.; Sousa, M.; Kang, D.; Rosenblatt, C., Continuous control of liquid crystal pretilt angle from homeotropic to planar. Appl. Phys. Lett. **2007,** 90, (19), 194102.

27. Zhuang, X.; Marrucci, L.; Shen, Y. R., Surface-Monolayer-Induced Bulk Alignment of Liquid Crystals. Physical Review Letters **1994,** 73, 1513-1516.

28. Price, A. D.; Schwartz, D. K., Fatty-Acid Monolayers at the Nematic/Water Interface: Phases and Liquid-Crystal Alignment. J. Phys. Chem. B **2007,** 111, (5), 1007-1015.

29. Brake, J. M.; Mezera, A. D.; Abbott, N. L., Active Control of the Anchoring of 4'-Pentyl-4-cyanobiphenyl (5CB) at an Aqueous-Liquid Crystal Interface By Using a Redox-Active Ferrocenyl Surfactant. Langmuir **2003,** 19, (21), 8629-8637.

30. Ogawa, K.; Mino, N.; Nakajima, K., Control of Pretilt Angles of Liquid Crystal Molecules in a Liquid Crystal Cell Using a Chemically Adsorbed Monolayer as an Alignment Film. Japanese Journal of Applied Physics **1990,** 29, (9), L1689-L1692.

31. Lockwood, N. A.; dePablo, J. J.; Abbott, N. L., Influence of Surfactant Tail Branching and Organization on the Orientation of Liquid Crystals at Aqueous-Liquid Crystal Interfaces. Langmuir **2005,** 21, (15), 6805-6814.

32. Filas, R. W.; Patel, J. S., Chemically induced high-tilt surfaces for liquid crystals. Applied Physics Letters **1987,** 50, (20), 1426-1428.

33. Seo, D.-S.; Han, J.-M., Generation of pretilt angle in NLCs and EO characteristics of a photo-aligned TN-LCD with oblique non-polarized UV light irradiation on a polyimide surface. Liq. Cryst. **1999,** 26, (7), 959-964.

34. Chaudhari, P.; Lacey, J.; Doyle, J.; Galligan, E.; Lien, S.-C. A.; Callegari, A.; Hougham, G.; Lang, N. D.; Andry, P. S.; John, R.; Yang, K.-H.; Lu, M.; Cai, C.; Speidell, J.; Purushothaman, S.; Ritsko, J.; Samant, M.; Stohr, J.; Nakagawa, Y.; Katoh, Y.; Saitoh, Y.; Sakai, K.; Satoh, H.; Odahara, S.; Nakano, H.; Nakagaki, J.; Shiota, Y., Atomic-beam alignment of inorganic materials for liquid-crystal displays. **2001,** 411, (6833), 56-59.

35. Sinha, G. P.; Wen, B.; Rosenblatt, C., Large, continuously controllable nematic pretilt from vertical orientation. Applied Physics Letters **2001,** 79, (16), 2543-2545.

36. Seo, D.-S.; Choi, J.-H., Preliminary communication Generation of high pretilt angle in a nematic liquid crystal with single oblique polarized UV light irradiation on polyimide surfaces. Liquid Crystals

Liquid Crystals J1 - Liquid Crystals **1999,** 26, (2), 291-293.

37. Moon, D. W.; Kurokawa, A.; Ichimura, S.; Lee, H. W.; Jeon, I. C., Ultraviolet-ozone jet cleaning process of organic surface contamination layers. Journal of Vacuum Science & Technology A: Vacuum, Surfaces, and Films **1999,** 17, (1), 150-154.

38. Ye, T.; Wynn, D.; Dudek, R.; Borguet, E., Photoreactivity of Alkylsiloxane Self-Assembled Monolayers on Silicon Oxide Surfaces. Langmuir **2001,** 17, (15), 4497-4500.

39. Kim, Y. J.; Zhuang, Z.; Patel, J. S., Effect of multidirection rubbing on the alignment of nematic liquid crystal. Appl. Phys. Lett. **2000,** 77, (4), 513-515.

40. Ban, B. S.; Kim, Y. B., Materials and Rubbing Dependence on Azimuthal Anchoring Energy of Rubbed Polyimide Surfaces. J. Phys. Chem. B **1999,** 103, (19), 3869-3871.

41. Kim, Y. B., Atomic force microscopy of rubbed polyimide aligning films for liquid crystal displays. Mol. Cryst. Liq. Cryst. Sci. Technol. Sect. A-Mol. Cryst. Liq. Cryst. **1995,** 262, 89-98.

42. Ishihara, S.; Wakemoto, H.; Nakazima, K.; Matsuo, Y., The effect of rubbed polymer films on the liquid crystal alignment. Liq. Cryst. **1989,** 4, (6), 669 - 675.

43. Vanaerle, N.; Barmentlo, M.; Hollering, R. W. J., Effect of Rubbingon the Molecular-Orientation Within Polyimide Orienting Layers of Liquid-Crystal Displays J. Appl. Phys. **1993,** 74, (5), 3111-3120.

44. Stohr, J.; Samant, M. G., Liquid crystal alignment by rubbed polymer surfaces: a microscopic bond orientation model. Journal of Electron Spectroscopy and Related Phenomena **1999,** 99, 189-207.

45. Sakamoto, K.; Arafune, R.; Ito, N.; Ushioda, S.; Suzuki, Y.; Morokawa, S., Molecular Orienatation fo Rubbed an Unrubbed Polyimide Films Determined by Polarized Infrared Absorption. Japanese Journal of Applied Physics **1994,** 33, L1323-L1326.

46. Nakajima, Y.; Saito, K.; Murata, M.; Uekita, M., The Pretitlt Angle Controllable Polyimide Langmuir-Blodgett-Film for Nematic Liquid Crystals Mol. Cryst. Liq. Cryst. Sci. Technol. Sect. A-Mol. Cryst. Liq. Cryst. **1993,** 237, 111-119.

47. Rasing, T.; I., M., Surfaces and Interfaces of Liquid Crystals. Springer: New York, 2004.

48. Crawford, G. P.; Ondris-Crawford, R. J.; Doane, J. W., Systematic study of orientational wetting and anchoring at a liquid-crystal-surfactant interface. Physical Review E **1996,** 53, (4), 3647-3662.

49. Seo, D.-S., Investigation of surface anchoring strength and pretilt angle in NLC on rubbed polythiophene surfaces with alkyl chain lengths. Liquid Crystals

Liquid Crystals J1 - Liquid Crystals **1999,** 26, (11), 1621-1624.

50. Bain, C. D.; Whitesides, G. M., Depth sensitivity of wetting: monolayers of .omega.-mercapto ethers on gold. J. Am. Chem. Soc. **1988,** 110, (17), 5897-5898.

51. Moon, D. W.; Kurokawa, A.; Ichimura, S.; Lee, H. W.; Jeon, I. C., Ultraviolet-ozone jet cleaning process of organic surface contamination layers. Journal of Vacuum Science & Technology A: Vacuum, Surfaces, and Films **1999,** 17, (1), 150-154.

52. Ito, Y.; Heydari, M.; Hashimoto, A.; Konno, T.; Hirasawa, A.; Hori, S.; Kurita, K.; Nakajima, A., The Movement of a Water Droplet on a Gradient Surface Prepared by Photodegradation. Langmuir **2007,** 23, (4), 1845-1850.

53. Ye, T.; McArthur, E. A.; Borguet, E., Mechanism of UV Photoreactivity of Alkylsiloxane Self-Assembled Monolayers. The Journal of Physical Chemistry B **2005,** 109, (20), 9927-9938.

54. Hong, L.; Sugimura, H.; Furukawa, T.; Takai, O., Photoreactivity of alkylsilane self-assembled monolayers on silicon surfaces and its application to preparing micropatterned ternary monolayers. Langmuir **2003,** 19, (6), 1966-1969.

55. Bloss, D. F., An Introduction to the Methods of Optical Crystallography. Holt, Rinehart and Winston: New York, Chicago, San Francisco, Toronto, London, 1961.

56. Israelachvili, J. N., Intermolecular And Surface Forces. Academic Press: 1991.

57. Alkhairalla, B.; Allinson, H.; Boden, N.; Evans, S. D.; Henderson, J. R., Anchoring and orientational wetting of nematic liquid crystals on self-assembled monolayer substrates: An evanescent wave ellipsometric study. Physical Review E **1999,** 59, (3), 3033-3039.

58. Wenzel, R. N., Resistance of Solid Surfaces to Wetting by Water Industrial & Engineering Chemistry **1936,** 28, (8), 988-994.

59. Cassie, A. B. D.; Baxter, S., Wettability of porous surfaces. Transactions of the Faraday Society **1944,** 40, 546-551.

60. Nosonovsky, M.; Bhushan, B., Cassie-Wenzel Wetting Regime Transition

Multiscale Dissipative Mechanisms and Hierarchical Surfaces. In Springer Berlin Heidelberg: 2008; pp 153-167.

61. Bain, C. D.; Whitesides, G. M., Depth sensitivity of wetting: monolayers of .omega.-mercapto ethers on gold. J. Am. Chem. Soc. **1988,** 110, (17), 5897-5898.

62. Walba, D. M.; Liberko, C. A.; Shao, R.; Clark, N. A., Smectic liquid crystal alignment using mechanically rubbed n-octadecylsiloxane self-assembled monolayers. Liq. Cryst. **2002,** 29, (8), 1015 - 1024.

Chapter 3

Liquid Crystal Response to Isolated DNA Helices

Nematic liquid crystals were exposed to glycidoxypropyltrimethoxysilane (GPTMS) self-assembled monolayer (SAMs) decorated with extended DNA molecules. GPTMS is known for imparting negligible anchoring energy on liquid crystals. Thus, it was hypothesized that inducing azimuthal alignment would cause a dramatic and long-ranging transition from random to uniform azimuthal alignment. Previous work indicated that DNA and other chiral molecules cause liquid crystal alignment at unique angles oblique to any extension direction. When DNA was stretched to its full contour length, it was discovered that while single-stranded DNA aligned the liquid crystal in the extension direction, double-stranded DNA (dsDNA) caused alignment at an oblique angle, providing a characteristic response to the chiral dsDNA helix that was readily observed optically. The intrinsic amplification due to liquid crystal orientational correlation enabled a macroscopic visible response to a single molecule of extended dsDNA.

3.1 Introduction

Phenomena that provide extraordinary sensitivity are greatly prized for applications including medical diagnostics, food safety, environmental monitoring, and bio-security. The apex of current medical technology is the plethora of diagnostic testing available for specific diseases. Significant potential for medical diagnostics exists in testing for proteins, genetic polymorphisms, and expressed genes to identify infectious diseases, cancers, and genetic disorders[1-4]. With today's technology, adults, children, and even embryos are routinely screened for genetic diseases. Newborns are tested for hereditary disease such as sickle-cell anemia and cystic fibrosis. Parents can even be screened prior to conception to determine the risk of passing such diseases on to offspring. Women opt to be tested for the BRCA1 gene (the breast cancer gene). Adult onset disorders such as Huntington's can be detected at any stage of life. Mapping the genetic material obtained from such tests has allowed scientists to pinpoint genes related to sudden infant death syndrome, neonatal diabetes, and bipolar disorder[5]. Often, these tests distinguish a mutation of only a single base pair, or a single nucleotide polymorphism (SNP). The ability to detect genomic variation with such precision allows applications such as forensics DNA analysis and evaluation of specific mutations as they relate to cancer prognosis and diagnosis. Two major categories currently exist for high sensitivity detection of biological molecules such as DNA and protein: (1) expensive and sophisticated laboratory instrumentation is used to detect low concentrations of target molecules, and (2) serial methods that amplify target molecules before measurement and detection.

3.1.1 Biosensing approaches

Biosensing devices use “capture molecules” to bind specific target molecules; in the case of DNA, we exploit the specific affinity of complementary DNA sequences for use as a capture sequence. Capture is followed by a “transduction” step, where the presence of the targeted molecule is converted into a measurable output signal. In the case of DNA, transduction discriminates between double-stranded (dsDNA) and single-stranded DNA (ssDNA), thereby identifying any captured molecules. Specifically, the basis for DNA identification involves synthesizing[6] the complement to a sequence of interest coupled with conditions designed to eliminate partially hybridized DNA pairs (high stringency conditions). The transduction step then identifies hybridized DNA molecules, effectively identifying any sequence.

The complementarity of DNA is so exact that the energetic difference between a perfect match and even a single nucleotide mismatch (single nucleotide polymorphism, or SNP) is detectable[7]. Stringency, or the conditions that favor hybridization, can be adjusted so that only perfectly matched strands will remain hybridized (high stringency). These conditions are affected by temperature, salt concentration, and pH[8]. Once hybridized under the proper stringency conditions, DNA sequences must then be identified via a transduction step. In most current approaches, transduction uses fluorescently labeled DNA to discriminate between dsDNA and ssDNA[9]. Keeping with convention, probe DNA is the sequence known to the experimenter. In a microarray format, these would be covalently attached to a surface. Target sequences are the unknown sequences to be identified. In fluorescent assays, these are labeled with a fluorophore to determine target location.

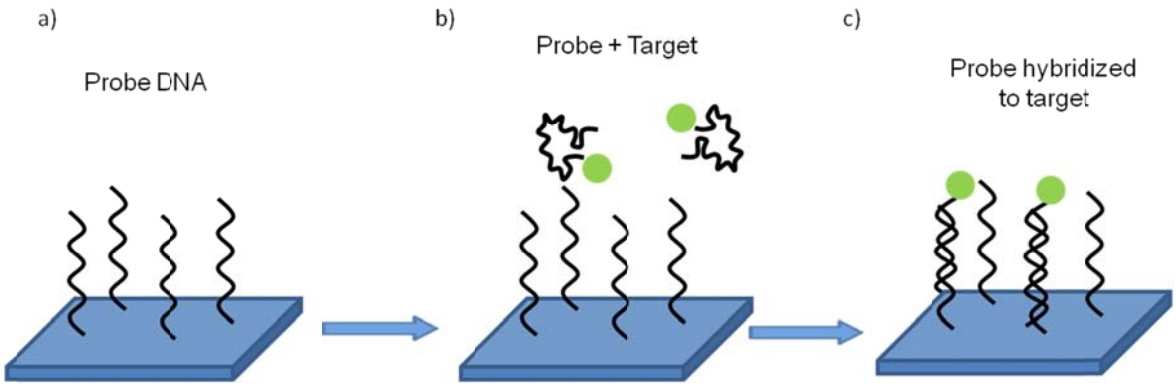

Figure 3.1: Description of the terminology of probe DNA and target DNA ion a fluorescently labeled system. a) Probe DNA is attached to a surface and the sequence is known to the experimenter. b) Labeled target DNA (sequence unknown to experimenter) is added to the system. c) DNA is hybridized. Unhybridized DNA is rinsed away, meaning any fluorescent molecules that remain must be hybridized to the surface DNA. This allows identification of target DNA, as the location and sequence of each complementary pair on the surface is known.

The affinity of complementary nucleotide sequences leads to two main detection strategies for detection: simplex and multiplex. When detection of low copy number is important, simplex methods such as quantitative PCR (qPCR) are used to amplify the sequence of interest. With proper primer selection, only the sequence of interest is amplified. Multi-primer PCR can be used to amplify several sequences at once, but this is not true multiplexing, as the number of parallel sequences quickly reaches an upper limit of 5 targets per tube.[10] Multiplexed methods rely on detection of multiple sequences in parallel, usually at low copy number.

Despite the fact that most approaches use fluorescence, it is the ability to discriminate between ssDNA and dsDNA that is the fundamental requirement for DNA biodetection, not fluorescence detection. This dissertation will explore preliminary

methods to differentiate between ssDNA and dsDNA without any chemical molecular modification steps such as fluorescent labeling.

3.1.2 Multiplexed current DNA technology

Owing to the vast scale of the human genome, it is advantageous to test multiple DNA sequences at once. Multiplexed devices allow this. Given the size of the genome, this is obviously a much more practical approach for increasing the throughput of genetic testing. While microarrays are not yet approved for many diagnostic purposes, rapid genotyping has the potential revolutionize patient care. Currently, it is possible to compare gene expression in normal and cancerous cells, thus relating specific genotypes to presented disease states. Genomic evaluation allows correlations to be drawn between patient genotype and treatment response, allowing for more effective practice of medicine[11]. It is also a gateway to personalized medicine, as target DNA or RNA can be obtained directly from a patient, and then used to determine an ideal course of treatment[4]. Because of the ability to screen for SNPs, alleles and gene expressions that indicate disease states and carrier states are readily identifiable. Like simplex devices, multiplexed systems are also based exploiting the complementarity of DNA, and rely on the specific interactions between probe and target DNA sequences. Multiple sequences of probe DNA are bound to a DNA chip, where thousands of individual oligomers can be tested against a single sample of patient DNA. With appropriate design, it is possible to obtain quantitative levels of gene expression (expression profiling) [1, 12-14].

In a typical fluorescent device, molecules are fluorescently labeled, and are then detected at very low concentrations using photon-counting devices. Various technologies have been developed to screen and identify DNA sequences. GeneChip technology from Affymatrix allows genotyping of SNPs on a genome-wide scale[15]. An extraordinarily sensitive device from Agilent utilizes a scanner capable of detecting 0.05 chromophores per square micron (cpsm)[16]. Fluorescent systems other than microplate-based readers also lend themselves to multiplexing. The Beadarray system from Illumina decorates individual beads with multiple oligonucleotides. Each bead is distributed into an array before scanning, where it is then identified via holographic label concurrently with fluorescent probe detection. The Luminex xMAP systems are especially ingenious at multiplexing. Labeled bead systems are again construed so that each bead tests for a different target. Rather than arrangement in an array, however, flow cytometry is used to individually identify each bead and read out the results for analyte detection. This allows multiplexing without having to establish separate workflows for each sample. The sheer allowable number of beads, along with the sorting mechanism based on flow cytometry makes this system ideal for multiplexing[17][18]. Sequencing can also be applied to detect the presence of target molecules[19]. Unsurprisingly, sequencing is primarily a simplex method.

3.1.3 Current simplex DNA technology

Simplex methods such as polymerase chain reaction (PCR) and sequencing are also employed for target DNA detection. In PCR, extremely low copy numbers of a specific sequence can be amplified in a single experiment. With selection of the proper

primers, if the target sequence is not present, it will not be amplified to the minimum detection level, turning PCR into an effective sensing mechanism as well. When detection of low copy number is important, real-time, or quantitative PCR (qPCR) is used to amplify the sequence of interest. Multi-primer PCR can be used to amplify several sequences at once, but this is not true multiplexing, as the number of parallel sequences quickly reaches an upper limit of 5 targets per tube[10]. Sequencing can also be applied to detect the presence of a target molecule[19]. Luminex is also known for sequencing, though understandably, the multiplexing for this method is much more limited (<10 sequences). Unsurprisingly, sequencing is primarily a simplex method[18].

Microscopy methods such as electron microscopy [20] or scanning probe microscopy [21] can also provide images of molecules with nanometer-scale resolution. Understandably, these approaches are best used at the bench-scale rather than with large-scale genetic testing. Yet another approach involves biochemical amplification methods. Immunoassays such as ELISA amplify specific interactions by exploiting specific binding to attach a labeled indicator molecule, usually fluorescent. Biochemical amplification is already effective; our work is designed to eliminate the need for amplification and labeling completely. In doing so, we will speed workflow, as well as eliminate the need for expensive labeling reagents.

3.1.4 Gap in current technology

While the previously mentioned technologies are effective at identifying DNA sequences, these technologies fall short with small-scale cost efficacy. The economy of scale of detecting hundreds of thousands of sequences at once makes the per oligomer test minimal. If testing for a single SNP, or sequence, however, the cost of target labeling, probe synthesis, and instrumentation can easily become cost prohibitive. Many applications also do not require the specificity and precision of detecting expression levels: a positive or negative test result would suffice. By elimination of the labeling, as well as fluorescent detection equipment that can easily cost upwards of $300,000[22], we can expand the reach of genetic testing. We will use the extreme sensitivity of liquid crystals, (see Chapter 1.2.3) to differentiate double and single stranded DNA, thus providing the basis of a technology that could be used to create a test to indicate the presence of hybridized DNA. This can act as a positive response for a disease state, while greatly reducing cost for a simplex test. This approach also lends itself to multiplexing. Our approach exhibits the necessary sensitivity to develop liquid crystal based DNA microarrays that can potentially be used without chemical amplification or expensive detection mechanisms in point-of-use applications.

3.1.5 Liquid crystalline response to DNA molecules

Previous examples of liquid crystals sensing biological molecules are plentiful in literature[23-26]. Liquid crystals have proven capable of responding to the presence of protein binding [27-29], nucleic acids [26, 30], and lipids [31, 32], providing a direct optical response without the need for chemical labeling. Our objective is to exploit liquid crystal

anchoring, as it exhibits extremely high sensitivity to intermolecular interactions. These approaches, however, are designed to observe changes in polar anchoring, generally a shift from homeotropic to tilted anchoring. One fundamental flaw with this approach is large elastic penalty for locally shifting a homeotropic to tilted alignment. If anchoring energy is high (Chapter 1.1.8), the extrapolation length of any effect due to DNA will be very small, and thus undetectable. DNA/liquid crystal anchoring would need to be incredibly strong to overcoming the energy due to homeotropic anchoring. In effect, due to the elasticity of liquid crystals, the overwhelming effect of a homeotropic anchoring disallows deviation from homeotropic anchoring, rending any surface changes indistinguishable, and the entire system would remain homeotropic rather than visualization of small regions affected by DNA. Studying azimuthal alignment in a surface passivated system, however, eliminates this problem; therefore we propose using glycidoxypropyltrimethoxysilane (also referred to GPTMS, GOPS, or GLYMO in literature). It has been previously shown to passivate the alignment layer, i.e. it imparts negligible azimuthal anchoring energy for several days. Negligible anchoring energy gives rise to essentially infinite extrapolation lengths, thus eliminating the energetic barriers to long-range ordering effects from liquid crystalline domain disruption. This propensity for long-range interactions is what gives a liquid crystal sensor system its extreme potential: a single molecule's worth of disruption can act as a catalyst to order an entire macroscopic network of molecules, thus giving a visual clue of surface interactions.

Instead or polar anchoring, as in literature, we will focus on an azimuthal mechanism for biomolecular detection. In this work, we report a unique technique that

requires neither sophisticated instrumentation nor chemical amplification to directly recognize dsDNA with single-molecule sensitivity. This extraordinary sensitivity is due to two characteristics of liquid crystals : (1) the responsiveness of liquid crystal molecules to subtle local structural features, such as the chirality of the dsDNA double helix, and (2) collective liquid crystal phenomena leading to long-range orientational order in the nematic phase; the latter results in a natural physical amplification effect where, in this case, the orientation of $>10^{14}$ liquid crystal molecules can be controlled by the presence of a single dsDNA helix.

3.2 Results and Discussion

3.2.1 GPTMS alignment layer

Our approach requires an underlying surface layer that imparts a negligible bias to liquid crystal orientation, so that it will respond to even a minimal symmetry-breaking stimulus. Satisfying this requirement, we use a glycidoxypropyltrimethoxysilane (GPTMS) self-assembled monolayer (SAM)[33, 34]. GPTMS surface coatings are known for their unique properties as liquid crystal alignment layers. They have already been shown to induce degenerate (random) planar liquid crystal anchoring with drop-cast films.[35] Instead of a drop-cast film, we use self-assembled monolayers in order to increase layer uniformity. The method of applying the film, however, does not affect GPTMS/liquid crystal interactions. GPTMS SAMs also induce planar anchoring.

While it is common for many alignment layers to induce degenerate planar alignment,[36, 37] GPTMS is unique in that it can *maintain* degenerate alignment over a time span of several days. [35, 38 39,40, 41,42-44] This implies that it can maintain degenerate azimuthal alignment without a surface memory effect (i.e negligible anchoring energy).

When there is a surface memory effect, the initial anchoring energy is zero, and liquid crystal molecules quickly and irreversibly adsorb to the alignment layer. These adsorbed orientations become essentially locked in, thus creating an easy axis and by extension, an anchoring energy. GPTMS passivates the surface by disallowing adsorption, therefore maintaining negligible anchoring energy over the course of our experiments.

Figures 3.2a and 3.2d show the nematic Schlieren texture that is characteristic of degenerate planar anchoring. While the fine details of this texture depend on the relative orientation of the sample and the polarizer, there is no overall anisotropy of the texture or intensity. We observed this type of degenerate planar texture even on samples that had been dipped in buffer solution to mimic the combing of DNA. This control experiment demonstrated that any residue due to removal from buffer solution was insufficient to cause a liquid crystal orientation[45], and inadequate to disrupt the degenerate azimuthal alignment. The fact that the GPTMS surfaces were sufficiently hydrophobic to emerge dry from the buffer may have been an important factor in minimizing this type of contamination.

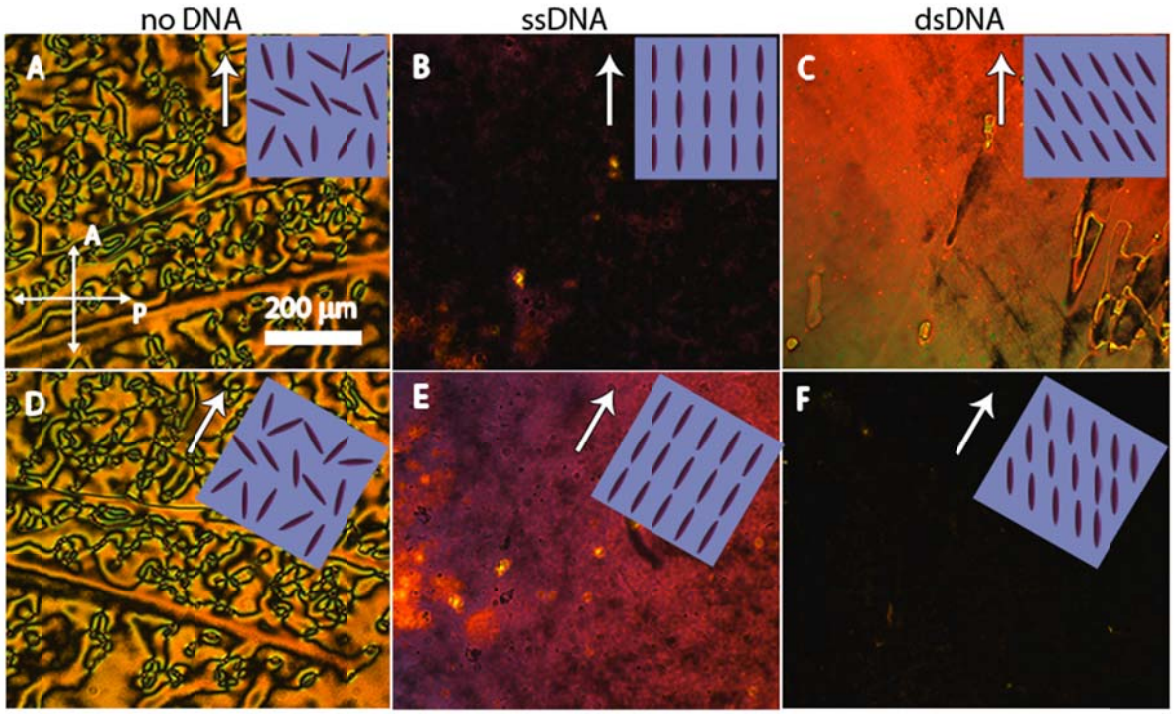

Figure 3.2: Polarized light images of hybrid aligned liquid crystal cells made with GPTMS and OTES monolayers respectively. White arrows indicate the dipping direction for DNA extension. Crossed white arrows indicated the directions of the crossed analyzer and polarizer. A dark image indicates crystal alignment in the direction of polarizer or analyzer. The inset cartoons demonstrate the alignment of crystal molecules that is consistent with the respective images. A) Control sample dipped in buffer with no DNA at 0˚ rotation (dipping direction aligned with the analyzer). B) ssDNA decorated surface at 0˚ rotation indicating crystal alignment at 0˚. C) dsDNA decorated surface at 0˚ rotation. D) Control sample with no DNA viewed at 30˚.E) ssDNA decorated surface at 30˚ rotation. F) dsDNA decorated surface at 30˚ rotation indicating alignment at ~–30˚.

3.2.2 Effect of dipping and DNA decoration on alignment layer

The presence of combed (i.e. extended via dipping) [46, 47] ssDNA was found to cause liquid crystal alignment in the extension direction ±10˚. This is demonstrated by Figures 3.2b and 3.2e, which show extinction when the combing direction is aligned directly with the polarizer (0˚) and high transmission when the sample is rotated to an

angle of 30˚. Although azimuthal liquid crystal alignment using ssDNA has not been explicitly demonstrated previously, alignment in the extension direction is expected due to the presence of topographic anisotropy breaking the orientational symmetry [48]. In fact, it is common to prepare surfaces for liquid crystal alignment by rubbing or brushing polymer surfaces to create this sort of anisotropy [49].

Remarkably, GPTMS surfaces decorated with extended dsDNA exhibited liquid crystal alignment at a characteristic oblique angle with respect to the combing direction; the chirality of this phenomenon suggests that it is in response to the dsDNA double helix. Figures 3.2c and 3.2f show high light transmission when the extension direction is aligned with the polarizer and extinction (low transmission) when the sample is rotated by 30˚, again demonstrating that this angle is related to the helical structure of dsDNA. The chirality of surface objects, in this case DNA, induces a chiral rotation in a non-chiral liquid crystal. [45, 50] Other groups produce similar results; for example, the Rosenblatt group has shown that liquid crystals align uniquely on chiral surface patterns etched with an AFM stylus.[51, 52 53] Xanthan gum, another chiral molecule, was separately reported to align liquid crystals at a characteristic angle of 15˚ from the presumed extension direction[54].

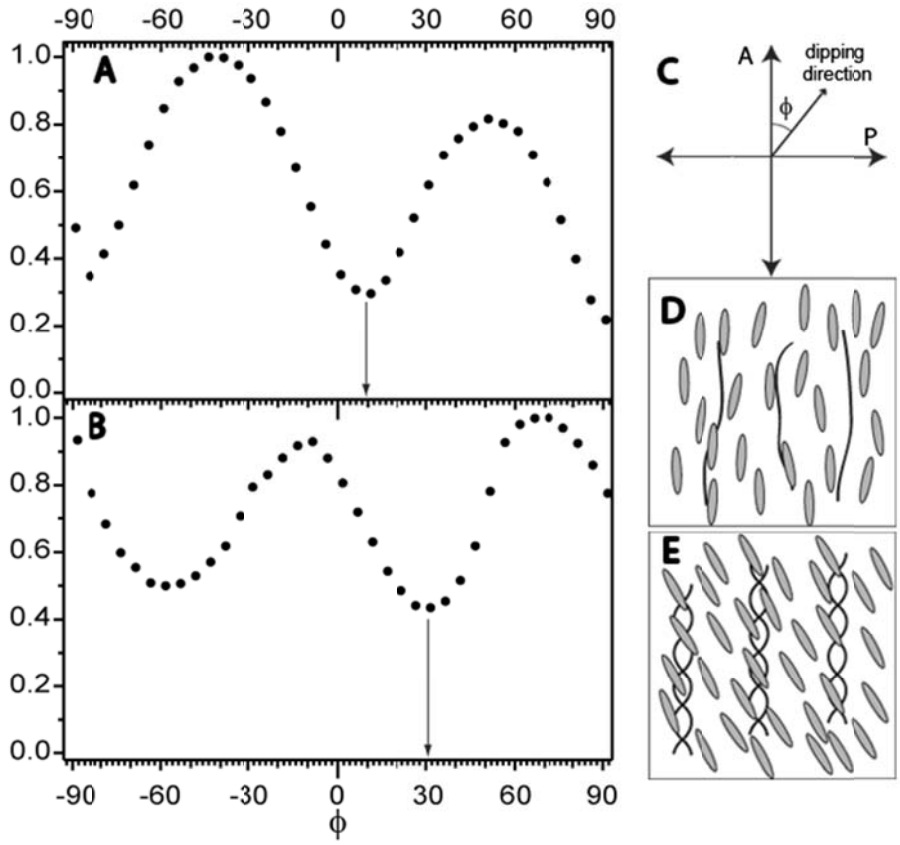

Figure 3.3: A) Representative normalized intensity measurement of polarized light transmitted through and liquid crystal cell with extended ssDNA. The arrow indicates the position of minimum intensity. B) Representative normalized intensity measurement of polarized light transmitted through a liquid crystal cell with extended dsDNA decorated GPTMS. C) Sample orientation used to determine liquid crystal alignment. "A" and "P" represent the crossed analyzer and polarizer respectively. ϕ is the angle between the dipping direction (i.e. the extension direction of DNA) and the analyzer. D) Schematic representation of liquid crystal molecules aligned in the ssDNA extension direction. E) Schematic representation of liquid crystal molecules aligned at –30° with respect to the dsDNA extension direction.

3.2.3 Determination of Alignment Angle

In order to determine the liquid crystal alignment angle more accurately, the transmitted optical intensity was measured as a function of the angle between the dipping/extension direction and the analyzer direction as defined in Figure 3.3c. Figure 3.3 shows representative data for liquid crystal cells aligned by ssDNA (Figure 3.3a) and dsDNA (Figure 3.3b) respectively. In the absence of DNA, there is no systematic variation of intensity as a function of angle. In the case of ssDNA (Figure 3.3a), the intensity minimum is at an angle near 0˚ (with some sample-to-sample variation), suggesting that the nematic director is in the DNA extension direction as shown schematically in Figure 3.3d. For dsDNA (Figure 3.3b), the intensity minimum is at an angle of ~30˚, suggesting that the liquid crystal director is rotated by ~–30˚ with respect to the DNA extension direction as shown schematically in Figure 3.3e. In fact, intensity minima occur every 90˚, when the liquid crystal director is aligned with either the polarizer or the analyzer; however, a quartz wedge compensator was used to determine that liquid crystal alignment was in the directions described above, and not offset by ±90˚.

3.2.4 Effect of liquid crystal molecular properties

Interestingly, the alignment angles for two different liquid crystal materials, 5CB and MBBA, were equal within experimental error, despite the fact that the two have distinctly different molecular structures (Figure 1.7) and electrostatic properties. In particular, 5CB is highly polar, while MBBA has a negligible dipole moment.[55-57] Because of the two molecules align identically within error, despite the different polarities, these results suggest that the alignment of nematic liquid crystals by dsDNA

may be a general effect due to steric molecular interactions with the detailed topography of individual dsDNA molecules, e.g. the major and/or minor grooves. This is in distinct contrast with previous experiments using sheared dsDNA gels as alignment layers by Nakata et al. They observed an angular offset between the shearing direction and liquid crystal alignment; however, In the case of the sheared gels, the alignment direction of 5CB and MBBA was dramatically different, and the authors concluded that the effect was due to electrostatic interactions between DNA and liquid crystal molecules.[25] This suggests that the molecular-level mechanism of liquid crystal alignment by isolated DNA molecules may be fundamentally different than alignment by the surface of dense DNA gels. In particular, in the case of isolated DNA molecules, the liquid crystal molecules can interact intimately with many parts of the DNA helix that may not be accessible when DNA molecules are organized into close-packed arrays such as in an aligned gel.

3.2.5 Visualized densely packed double-stranded DNA molecules

Figure 3.4 shows a fluorescence image of labeled lambda DNA along with a graph of the optical transmission as a function of sample orientation for the same field of view. Lambda DNA was deliberately chosen because the extremely long molecules enable clear observation and measurement of both the DNA extension efficiency as well as extension direction. However, efficient combing of extremely long DNA presents significant challenges, and we generally observed that most regions exhibited a mixture of well-combed molecules and other molecules that were clumped or entangled as shown in Figure 3.4a. These clumps and entanglements are presumably due to multiple attachment points of the DNA during incubation, but before extension. It is

clear that based on this hypothesis that shortened DNA molecules would thus result in more efficient combing, but it proved difficult to obtain large amounts of DNA that would still be long enough to view extension via microscopy (several thousand base pairs).

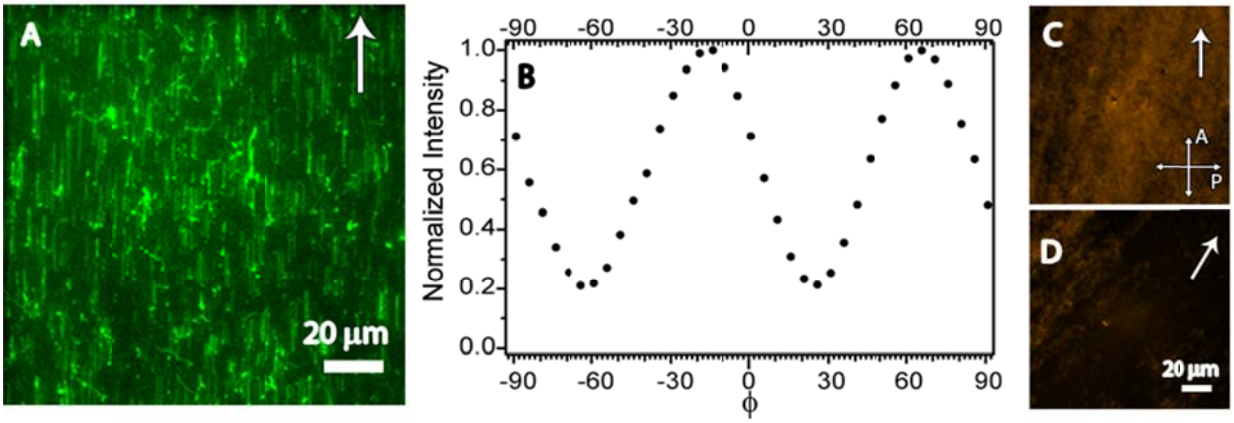

Figure 3.4: (A) A fluorescence microscope image of fluorescently-labeled combed lambda dsDNA. Approximately 70% of the molecules are aligned and extended. (B) The normalized intensity of polarized light transmitted through the liquid crystal cell with crossed polarizers for the same field of view as shown in part A. (C) Polarized light image of the same field of view 0˚ rotation. The arrow represents the dipping direction. The crossed arrows represent the directions of the crossed polarizers. (D) Polarized light image of the same field of view at 30˚ rotation. The arrow represents the dipping direction.

In a real detection application, of course, it would not be necessary to comb such large pieces of DNA. This representative image suggests that molecules were indeed extended in the combing direction (Figure 3.4a). Furthermore, the transmission intensity from co-localized regions permits us to directly correlate dsDNA extension, liquid crystal orientation, and the degree of liquid crystal alignment, as measured by the effective optical birefringence (e.g. the ratio of the maximum to minimum light intensity as a function of angle).

We found significant scatter from sample to sample in the liquid crystal orientation for both 5CB (–33˚±6˚) and MBBA (–28˚±12˚); these uncertainties are significantly larger than error associated with our ability to reproducibly measure the relative alignment angle between DNA and liquid crystal, which we estimate at ±3˚. It is not clear at this point whether this scatter is due to small variations in local DNA orientation or to DNA overstretching that could lead to subtle changes in the direction of DNA grooves with respect to the extension direction. The experimental uncertainty of the alignment angle caused by ssDNA had a somewhat different origin. Since we were unable to directly determine the exact alignment direction of individual ssDNA strands, the alignment angle was determined only by comparing macroscopic images to the nominal combing angle. Additionally, the inability to center the axis of rotation perfectly with the field of view affected the measured intensities, and thus the positions of the minima. This led to the relatively large uncertainties (±10˚) in the azimuthal alignment associated with ssDNA.

3.2.6 Visualized isolated dsDNA molecules

The angle or extent of liquid alignment was not significantly influenced by the identity of the liquid crystal material, the source of the DNA, or most importantly, the amount of DNA present. These variations are all illustrated in Figure 3.5. Figures 3.5a and 3.5c show fluorescence images for fields of view containing ~80 and ~40 molecules of calf thymus (~15,000 bp) and lambda dsDNA respectively. Figures 3.5b and 3.5d show the corresponding optical intensity versus sample orientation through crossed polarizers for liquid cells made with 5CB (Fig. 3.5b) and MBBA (Fig. 3.5d) respectively.

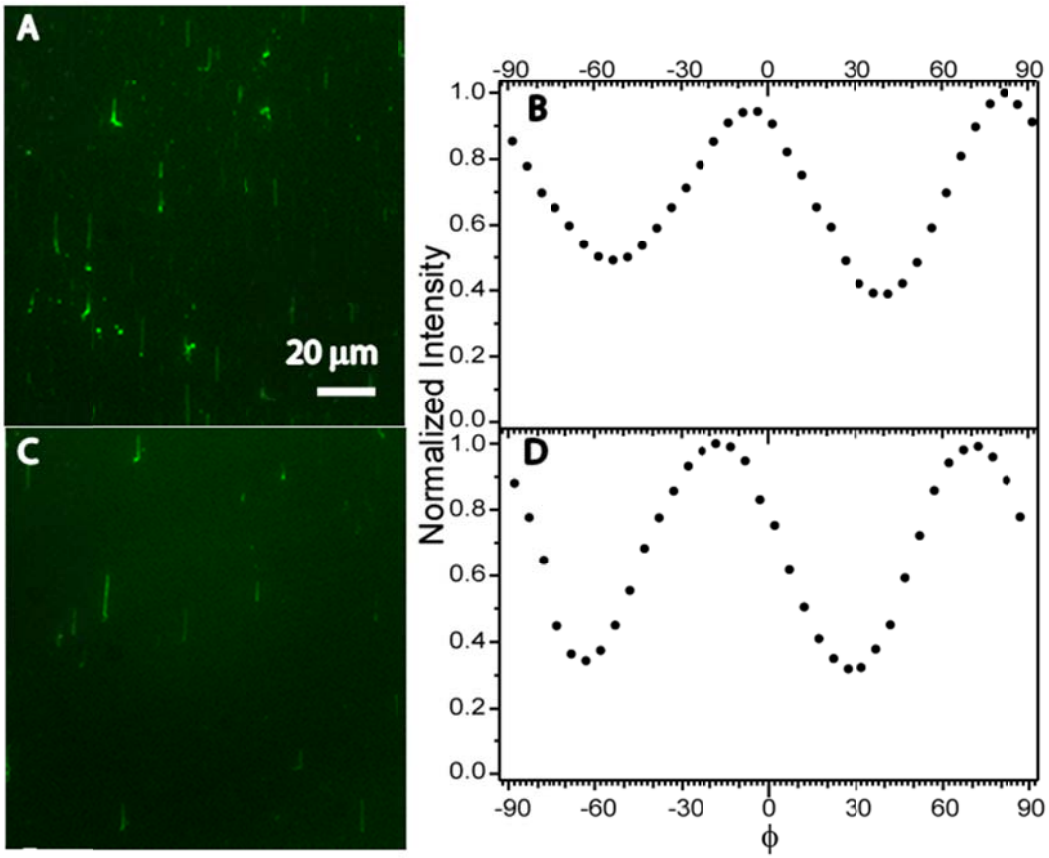

Figure 3.5: Liquid crystal alignment is demonstrated by multiple types of DNA, with multiple liquid crystals, and at various levels of DNA surface concentration. (A) Fluorescence image showing ~80 calf thymus dsDNA molecules (B) Normalized intensity of polarized light as a function of rotation angle transmitted through a 5CB liquid crystal cell corresponding to the field of view shown in part A. (C) Fluorescence image showing ~40 lambda dsDNA molecules. (D) Normalized intensity of polarized light as a function of rotation angle transmitted through an MBBA liquid crystal cell corresponding to the field of view shown in part C

In both cases, the extinction direction is at an oblique angle with respect to the dipping direction as described above. Also, in both cases, the degree of liquid crystal alignment, as indicated by the ratio of the maximum and minimum optical intensities, are similar and representative of what was observed for samples where the majority of dsDNA molecules were well-extended. Comparing Figure 3.4b to Figures 3.5b, 3.5d, and 3.6b, one can see that the response of the liquid crystal to dsDNA does not change appreciably as the dsDNA surface density decreased by an order of magnitude. This is in contrast with other detection methods, where the signal used for detection decreases systematically as the amount of analyte decreases.

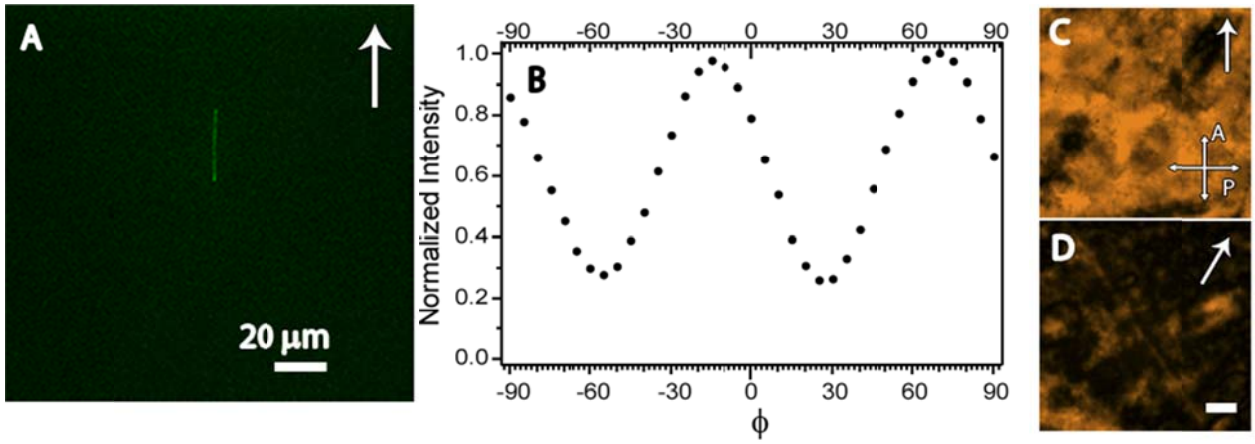

Figure 3.6: Liquid crystal alignment is demonstrated by single aligned DNA molecule, with 5CB. (A) Fluorescence image showing a single lambda dsDNA molecule. The white arrow indicates dipping direction. (B) Normalized intensity of polarized light as a function of rotation angle transmitted through a 5CB liquid crystal cell corresponding to the field of view shown in part E. (C) Polarized light image of the same field of view 0˚ rotation. The arrow represents the dipping direction. (D) Polarized light image of the same field of view at 30˚ rotation. The arrow represents the dipping direction.

Fundamentally, this is due to the fact that the liquid crystal response is due to a broken rotational symmetry, so that even a small anisotropy results in a well-correlated macroscopic response. However, this also means that the liquid crystal response requires the presence of significant surface anisotropy due to well-combed dsDNA, so regions of poorly-combed dsDNA result in weak liquid crystal alignment in random directions. This direct visual correlation of DNA extension efficiency and liquid crystal alignment confirms that the liquid crystal alignment is in fact caused by the presence of extended dsDNA and not another factor.

3.2.7 Macroscopic optical response of liquid crystal

Since the bare GPTMS surface provides such a small effect on liquid crystal orientation, in principle even a tiny amount of anisotropy will result in macroscopic alignment. We tested this by preparing surfaces with extraordinarily low surface densities of combed dsDNA, including examples where only a single dsDNA molecule appeared in a given 137µm x 137µm field of view (a DNA fractional surface coverage of only 10^{-6}), as shown in Figure 3.6a. A strong macroscopic response was always observed as long as the dsDNA was well-aligned (Figure 3.6b). In fact, the optical response was nearly as strong for one molecule (Figure 3.6b) as for 400 molecules (Figure 3.4b). The polarized optical micrographs shown in Figures 3.6c and 3.6d demonstrate that the azimuthal alignment was uniform over ~50 µm, a reasonable expectation of extrapolation length. Overall, the entire field of view was aligned sufficiently that $>10^{14}$ liquid crystal molecules responded to the presence of the single dsDNA molecule.

3.2.8 Effect of anchoring energy on optical response

The macroscopic response associated with only a single DNA molecule is likely due to the ability of GPTMS to passivate liquid crystal/surface interactions, resulting in a very small azimuthal anchoring energy associated with the GPTMS "background" [35, 38]. In fact, in a hypothetical limiting case of zero azimuthal anchoring energy, an "easy cone" rather than an easy axis for alignment is present, meaning that there is no energetic penalty for the liquid crystal to reorient along any particular azimuthal direction. This implies that upon decoration of a GPTMS surface with DNA, the liquid crystal alignment induced by extended DNA molecules propagates throughout the liquid crystal cell with no energetic penalty, thus allowing for the large amplification of signal seen in Figures 3.2, 3.4, and 3.5. In practice, there is a small, but still non-zero value of the azimuthal anchoring strength on GPTMS surfaces leads to textures with a characteristic length scale given by a quantity known as the extrapolation length, $L = K/W$, where K is the twist elastic constant of the liquid crystal and W is the azimuthal anchoring energy[58]. The sizes of correlated domains in Figures 3.2, 3.4, and 3.6 suggest an effective extrapolation length in the range of 50–100 μm, consistent with an anchoring energy of ~10^{-8} J/m^2. Interestingly, the size of the correlated domains in the liquid crystal/DNA samples suggests that the area of influence of a given DNA molecule should also be limited to an area associated with L~50 μm, consistent with what is observed in Figure 3.6.

The observed anchoring energy is consistent with previous observed values for spin-cast GPTMS films, in which films with thicknesses over 20 Å essentially eliminated anchoring energy, and in contrast with the strong azimuthal anchoring of 5CB on glass

(W~10^{-5} J/m^2). [35, 38, 59] The lowest anchoring energy recorded is $3 \cdot 10^{-10}\,\mathrm{J/m^2}$, however this is conical, not planar anchoring. Additionally, this passivation layer is swollen by the liquid crystal, so rather than avoiding liquid crystal interactions, this system depends on liquid crystal/substrate interactions.[60]

3.2.9 Statistical discussion of observations

As mentioned briefly above, the consistency of the oblique liquid crystal alignment was directly related to the quality and quantity of the combed dsDNA. For samples where the surface concentration of dsDNA was such that the average molecular separation was much smaller than the extrapolation length, the liquid crystal alignment was extremely reproducible and uniform, e.g. for surfaces with more than 100 of aligned molecules in the field of view, 5CB was aligned at an oblique angle with a value of 32º ± 4 º. However, for samples with very low surface concentrations of dsDNA, where the average molecular separation was on the same order of magnitude as the liquid crystal extrapolation length, there was greater angular uncertainty and less consistent results. In large part, this was due to the difficulty in achieving consistent dsDNA extension at very low surface coverage. We often observed clumped and/or coiled dsDNA molecules coexisting with well-combed molecules; presumably the clumping is due to the formation of multiple surface-attachment sites during the combing process. Understandably, these surfaces with a large fraction of clumped dsDNA typically gave non-uniform and/or weak liquid crystal alignment. However, even for regions where the separation between dsDNA molecules was very large (Figure 3.5c or 3.6a), when the molecules were reasonably well-aligned, the liquid crystal alignment was also consistent. Specifically, of the 5 samples with low dsDNA surface density (few

than 20 extended molecules) where over 50% of the dsDNA molecules were observed to be well-combed, 100% of these samples exhibited oblique liquid crystal alignment in the angular range 23˚–43˚.

3.3 Conclusions

The distinctive chiral liquid crystal alignment oblique to the extension direction for dsDNA provides a direct signature of hybridization, which could potentially be used as a new type of DNA sensor/microarray. Because the extent of azimuthal alignment does not appear to depend on the surface concentration, but rather on the percentage of extended DNA, optimization of the extension conditions will lead to extreme sensitivity, with the possibility of routine single molecule detection. In addition to combing, other strategies for DNA extension, including microfluidic flow [61] magnetic bead attachment [62], and electrophoretic extension[63, 64], may lead to the desired improvement in extension efficiency.

3.4 References

1. Schena, M.; Shalon, D.; Davis, R. W.; Brown, P. O., Quantitative Monitoring of Gene Expression Patterns with a Complementary DNA Microarray. *Science* **1995,** 270, (5235), 467-470.

2. Raj, A.; van den Bogaard, P.; Rifkin, S. A.; van Oudenaarden, A.; Tyagi, S., Imaging individual mRNA molecules using multiple singly labeled probes. *Nat Meth* **2008,** 5, (10), 877-879.

3. Schena, M., *Protein Microarrays*. Jones and Bartelett Publishers Sudbury, MA, 2005.

4. Ekins, R.; Chu, F. W., Microarrays: their origins and applications. *Trends in Biotechnology* **1999,** 17, (6), 217-218.

5. Kimmel, A.; Oliver, B., *Methods in Enzymology*. Elsiver: Amsterdam, 2006; Vol. 410.

6. Caruthers, M. H., GENE SYNTHESIS MACHINES - DNA CHEMISTRY AND ITS USES. *Science* **1985,** 230, (4723), 281-285.

7. Anderson, M. L. M., *Nucleic Acid Hybridization*. Springer: New York, 1999.

8. Bloomfield, V. A.; Crothers, D. M.; Ignacio Itnoco, J., *Nucleic Acids: Structure, Properties, and Functions*. University Science Books: Sausalito, CA, 2000.

9. Sassolas, A.; Leca-Bouvier, B. D.; Blum, L. J., DNA biosensors and microarrays. *Chem. Rev.* **2008,** 108, (1), 109-139.

10. Agilent http://www.genomics.agilent.com/CollectionSubpage.aspx?PageType=Product&SubPageType=ProductDetail&PageID=359. (07-06-2011),

11. Affymatrix, Microarray Products. **2011**.

12. Schena, M.; Heller, R. A.; Theriault, T. P.; Konrad, K.; Lachenmeier, E.; Davis, R. W., Microarrays: biotechnology's discovery platform for functional genomics. *Trends in Biotechnology* **1998,** 16, (7), 301-306.

13. Schena, M.; Shalon, D.; Heller, R.; Chai, A.; Brown, P. O.; Davis, R. W., Parallel human genome analysis: Microarray-based expression monitoring of 1000 genes. *Proceedings of the National Academy of Sciences of the United States of America* **1996,** 93, (20), 10614-10619.

14. Schena, M., Charting the microarray revolution. *Scientist* **2004,** 18, (19), 30-31.

15. Kennedy, G. C.; Matsuzaki, H.; Dong, S. L.; Liu, W. M.; Huang, J.; Liu, G. Y.; Xu, X.; Cao, M. Q.; Chen, W. W.; Zhang, J.; Liu, W. W.; Yang, G.; Di, X. J.; Ryder, T.; He, Z. J.; Surti, U.; Phillips, M. S.; Boyce-Jacino, M. T.; Fodor, S. P. A.; Jones, K. W., Large-scale genotyping of complex DNA. *Nature Biotechnology* **2003,** 21, (10), 1233-1237.

16. Aglient http://www.chem.agilent.com/Library/datasheets/Public/5990-6404en_lo.pdf. http://www.chem.agilent.com/Library/datasheets/Public/5990-6404en_lo.pdf (8/19/2011),

17. Illumina BeadArray. http://www.illumina.com/technology/beadarray_technology.ilmn

18. Luminex http://www.luminexcorp.com/TechnologiesScience/xMAPTechnology/index.htm

19. Illumina, TruSeq. **2011**.

20. Griffith, J. D., DNA-STRUCTURE - EVIDENCE FROM ELECTRON-MICROSCOPY. *Science* **1978,** 201, (4355), 525-527.

21. Bustamante, C.; Vesenka, J.; Tang, C. L.; Rees, W.; Guthold, M.; Keller, R., Circular DNA-Molecules Imaged in Air by Scanning Force Mircoscopy *Biochemistry* **1992,** 31, (1), 22-26.

22. Affymatrix, Product Pricing. **2011**.

23. Lai, S. L.; Tan, W. L.; Yang, K.-L., Detection of DNA Targets Hybridized to Solid Surfaces Using Optical Images of Liquid Crystals. *ACS Applied Materials & Interfaces*, null-null.

24. Chen, C. H.; Yang, K. L., Detection and Quantification of DNA Adsorbed on Solid Surfaces by Using Liquid Crystals. *Langmuir* **2010,** 26, (3), 1427-1430.

25. Nakata, M.; Zanchetta, G.; Buscaglia, M.; Bellini, T.; Clark, N. A., Liquid Crystal Alignment on a Chiral Surface: Interfacial Interaction with Sheared DNA Films. *Langmuir* **2008,** 24, (18), 10390-10394.

26. Price, A. D.; Schwartz, D. K., DNA Hybridization-Induced Reorientation of Liquid Crystal Anchoring at the Nematic Liquid Crystal/Aqueous Interface. *Journal of the American Chemical Society* **2008,** 130, (26), 8188-8194.

27. Hartono, D.; Bi, X.; Yang, K.-L.; Yung, L.-Y. L., An Air-Supported Liquid Crystal System for Real-Time and Label-Free Characterization of Phospholipases and Their Inhibitors. *Advanced Functional Materials* **2008,** 18, (19), 2938-2945.

28. Brake, J. M.; Daschner, M. K.; Luk, Y.-Y.; Abbott, N. L., Biomolecular Interactions at Phospholipid-Decorated Surfaces of Liquid Crystals. *Science* **2003,** 302, (5653), 2094-2097.

29. Brake, J. M.; Abbott, N. L., Coupling of the orientations of thermotropic liquid crystals to protein binding events at lipid-decorated interfaces. *Langmuir* **2007,** 23, (16), 8497-8507.

30. Bi, X.; Huang, S.; Hartono, D.; Yang, K.-L., Liquid-crystal based optical sensors for simultaneous detection of multiple glycine oligomers with micromolar concentrations. *Sensors and Actuators B: Chemical* **2007,** 127, (2), 406-413.

31. Price, A. D.; Schwartz, D. K., Fatty-acid monolayers at the nematic/water interface: Phases and liquid-crystal alignment. *Journal of Physical Chemistry B* **2007,** 111, (5), 1007-1015.

32. Brake, J. M.; Daschner, M. K.; Abbott, N. L., Formation and characterization of phospholipid monolayers spontaneously assembled at interfaces between aqueous phases and thermotropic liquid crystals. *Langmuir* **2005,** 21, (6), 2218-2228.

33. Malone, S. M.; Schwartz, D. K., Polar and Azimuthal Alignment of a Nematic Liquid Crystal by Alkylsilane Self-Assembled Monolayers: Effects of Chain-Length and Mechanical Rubbing

doi:10.1021/la801322x. *Langmuir* **2008,** 24, (17), 9790-9794.

34. Walba, D. M.; Liberko, C. A.; Korblova, E.; Farrow, M.; Furtak, T. E.; Chow, B. C.; Schwartz, D. K.; Freeman, A. S.; Douglas, K.; Williams, S. D.; Klittnick, A. F.; Clark, N. A., Self-assembled monolayers for liquid crystal alignment: simple preparation on glass using alkyltrialkoxysilanes. *Liquid Crystals* **2004,** 31, (4), 481 - 489.

35. Dozov, I.; Stoenescu, D. N.; Lamarque-Forget, S.; Martinot-Lagarde, P.; Polossat, E., Planar degenerated anchoring of liquid crystals obtained by surface memory passivation. *Applied Physics Letters* **2000,** 77, (25), 4124-4126.

36. Blinov, L. M.; Cigrinov, V. G., *Electrooptic effects in liquid crystal materials*. Springer: New York [etc.], 1996.

37. Rasing, T.; I., M., *Surfaces and Interfaces of Liquid Crystals*. Springer: New York, 2004.

38. Stoenescu, D. N.; Nguyen, H. T.; Barois, P.; Navailles, L.; Nobili, M.; Martinot-Lagarde, P.; Dozov, I., Optical Studies of Chiral Mesophases in Sandwich Cells with Planar Degenerated Anchoring. *Molecular Crystals and Liquid Crystals Science and Technology. Section A. Molecular Crystals and Liquid Crystals* **2001,** 358, (1), 275-286.

39. Martinon-Largarde, P.; Dozov, I.; Yvette, G. s.; Polossat, E.; Raspaud, E.; Auroy, P.; Ramdane, O. O.; Durand, G.; Forget, S. Liquid Crystal Device Comprising Anchoring Means on at Least One Confinement Plate Providing a Degenerated Orientation. 6452573, 2002.

40. Clark, N. A., Surface memory effects in liquid crystals: Influence of surface composition. *Physical Review Letters* **1985,** 55, (3), 292.

41. Ouchi, Y.; Feller, M. B.; Moses, T.; Shen, Y. R., Surface Memory Effect at the Liquid-Crystal-Polymer Interface. *Physical Review Letters* **1992,** 68, (20), 3040-3043.

42. Nespoulous, M.; Blanc, C.; Nobili, M., Ultraweak azimuthal anchoring of a nematic liquid crystal on a planar orienting photopolymer. *Journal of Applied Physics* **2007,** 102, (7), 073519.

43. Bryan-Brown, G. P.; Wood, E. L.; Sage, I. C., Weak surface anchoring of liquid crystals. *Nature* **1999,** 399, (6734), 338-340.

44. Pires, D.; Galerne, Y., Anchoring and memory of the azimuthal nematic orientation. *Applied Physics Letters* **2006,** 89, (14), 3.

45. Hoogboom, J.; Clerx, J.; Otten, M. B. J.; Rowan, A. E.; Rasing, T.; Nolte, R. J. M., Novel alignment technique for LCD-biosensors. *Chemical Communications* **2003**, (23), 2856-2857.

46. Bensimon, A.; Simon, A.; Chiffaudel, A.; Croquette, V.; Heslot, F.; Bensimon, D., Alignment and sensitive detection of DNA by a moving interface. *Science* **1994,** 265, (5181), 2096-2098.

47. Bensimon, D.; Simon, A. J.; Croquette, V.; Bensimon, A., Stretching DNA with a Receding Meniscus- Experiments and Models. *Physical Review Letters* **1995,** 74, (23), 4754-4757.

48. Berreman, D. W., Solid Surface Shape and the Alignment of an Adjacent Nematic Liquid Crystal. *Physical Review Letters* **1972,** 28, (26), 1686-1686.

49. Stohr, J.; Samant, M. G.; Cossy-Favre, A.; Diaz, J.; Momoi, Y.; Odahara, S.; Nagata, T., Microscopic origin of liquid crystal alignment on rubbed polymer surfaces. *Macromolecules* **1998,** 31, (6), 1942-1946.

50. Jiang, S.; Liu, M., Aggregation and Induced Chirality of an Anionic meso-Tetraphenylsulfonato Porphyrin (TPPS) on a Layer-by-Layer Assembled DNA/PAH Matrix. *The Journal of Physical Chemistry B* **2004,** 108, (9), 2880-2884.

51. Ferjani, S.; Choi, Y.; Pendery, J.; Petschek, R. G.; Rosenblatt, C., Mechanically Generated Surface Chirality at the Nanoscale. *Physical Review Letters* **2010,** 104, (25), 4.

52. Ferjani, S.; Pendery, J.; Rosenblatt, C., Mechanically generated surface chirality: Control of chiral strength. *Applied Physics Letters* **2010,** 97, (12), 3.'

53. Choi, Y.; Atherton, T.; Ferjani, S.; Petschek, R. G.; Rosenblatt, C., Patterning-induced surface chirality and modulation of director twist in a nematic cell. *Physical Review E* **2009,** 80, (6), 4.

54. Haaren, J. v., Wiping out dirty displays. *Nature* **2001,** 411, 29-30.

55. Bradshaw, M. J.; Raynes, E. P.; Bunning, J. D.; Faber, T. E., THE FRANK CONSTANTS OF SOME NEMATIC LIQUID-CRYSTALS. *Journal De Physique* **1985,** 46, (9), 1513-1520.

56. Raszewski, Z.; Rutkowska, J.; Kedzierski, J.; Zielinski, J.; Perkowski, P.; Piecek, W.; Zmija, J., DIELECTRIC METHOD OF DETERMINATION OF THE ASSOCIATION ENERGY BETWEEN POLAR-MOLECULES IN NEMATIC LIQUID-CRYSTAL. *Molecular Crystals and Liquid Crystals Science and Technology Section a-Molecular Crystals and Liquid Crystals* **1994,** 251, 357-365.

57. Sprokel, G. J., RESISTIVITY, PERMITTIVITY AND ELECTRODE SPACE-CHARGE OF NEMATIC LIQUID-CRYSTALS. *Molecular Crystals and Liquid Crystals* **1973,** 22, (3-4), 249-260.

58. Bai, Y.; Abbott, N. L., Recent Advances in Colloidal and Interfacial Phenomena Involving Liquid Crystals. *Langmuir* **2011,** 27, (10), 5719-5738.

59. Marinont-Legarde, P.; Dozov, I.; Polossat, E.; Raspaud, E.; Auroy, P.; Ramdane, O. O.; Durand, G.; Forget, S. Liquid crystal device comprising anchoring means on at least one confinement. 2002.

60. Ramdane, O. O.; Auroy, P.; Forget, S.; Raspaud, E.; Martinot-Lagarde, P.; Dozov, I., Memory-Free Conic Anchoring of Liquid Crystals on a Solid Substrate. *Physical Review Letters* **2000,** 84, (17), 3871.

61. Perkins, T. T.; Smith, D. E.; Chu, S., Single Polymer Dynamics in an Elongational Flow. *Science* **1997,** 276, (5321), 2016-2021.

62. Smith, S.; Finzi, L.; Bustamante, C., Direct mechanical measurements of the elasticity of single DNA molecules by using magnetic beads. *Science* **1992,** 258, (5085), 1122-1126.

63. Schurr, J. M.; Smith, S. B., Theory for the extension of a linear polyelectrolyte attached at one end in an electric field. *Biopolymers* **1990,** 29, (8-9), 1161-1165.

64. Stigter, D.; Bustamante, C., Theory for the Hydrodynamic and Electrophoretic Stretch of Tethered B-DNA. *Biophysical Journal* **1998,** 75, (3), 1197-1210.

Chapter 4

Lyotropic Linactant Self-Assembly in Two Dimensions

We observed phenomena within two-component Langmuir monolayers that are analogous to surfactant self-assembly in three-dimensional solutions. A partially-fluorinated phosphonic fatty acid, previously shown to be line-active, played the role of two-dimensional (2D) surfactant (linactant) and a perfluorinated fatty acid acted as the 2D solvent. Langmuir-Blodgett monolayers were prepared from mixtures of these compounds and examined using atomic force microscopy. Above a critical linactant mole fraction of ~0.02, distinctive monodisperse structural features were observed with a characteristic diameter of ~30 nm, and an apparent height of 1.4 nm above the background. As the linactant concentration was further increased, the number density of these features increased, while the feature size remained the same. These observations suggested that the features corresponded to self-limiting clusters composed of linactant molecules, and that the dispersed clusters represented a 2D micellar phase. Above a linactant mole fraction of 0.63, the clusters organized into a local hexagonal structure with short-range positional order indicative of a liquid crystalline phase; the correlation length increased systematically with increasing linactant concentration.

4.1 Introduction

4.1.1 Phases at the interface

Again, the three most common phases of matter are gases, liquids, and solids. A lesser known phase is liquid crystals, a mesophase that exists between the liquid and solid phases. Unsurprisingly, it is a hybrid with both liquid and crystalline properties. Liquid crystals possess long range orientational order, but also maintain the ability to flow like a liquid. Liquid crystals are classified as a three-dimensional bulk phase. Phenomenon in the bulk phase are well understood, but phase behavior at the interface is can lead to additional interesting properties.[1] The transition between compositions and properties of two distinct phases leads to unique conditions present in the bulk of neither.[2, 3] The boundary between gases and liquids, e.g. the air/water interface, is of particular interest. Certain classes of molecules partition to the interface, generally to minimize free energy due to distinct molecular moieties. These are called *surfactants*, short for surface active agent (see Figure 1.5). Surfactants act as a unique probe by specifically interacting at the interface nearly exclusively, making them particularly useful for probing interfacial conditions.

4.1.2 Monolayers

Monolayers are defined as a collection of molecules a single molecule thick. One method of formation occurs when surfactants partition to the interface. The energy minimization inherent to the partitioning imparts molecular order as well. At the air-water interface, for example, the hydrophilic headgroup is in the aqueous phase, while the hydrophobic tail group orients itself into the air, causing the orientations of all the

molecules in an equilibrated monolayer to be similar (Figure 4.1). At an oil/water interface, the hydrophobic tail would orient into the fatty phase, while the hydrophilic headgroup remained in the aqueous phase. This work will consist of studies of unique phenomena that occur within monolayers.

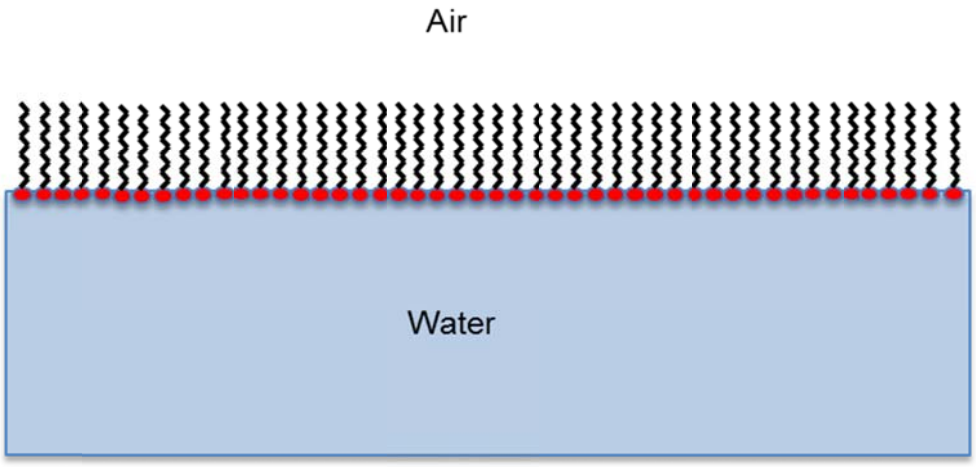

Figure 4.1: Surfactants undergoing self-assembly at the air water interface. This example represents amphiphilic molecules, which contain hydrophilic and hydrophobic regions. Hydrophobic tails orient themselves out in the air, while hydrophilic headgroups bury themselves in the aqueous phase.

Monolayers themselves are not a homogenous category (see Figure 4.2). Differing surfactant solubility results in two distinct categories of monolayers. Soluble surfactants form Gibbs monolayers, in which surfactants solvated in the bulk solution are at equilibrium with the molecules that partition to the interface. Insoluble surfactants form Langmuir monolayers. Rather than a monolayer spontaneously forming from a bulk surfactant solution, Langmuir monolayers must be deposited directly at the interface. This is done by dissolving the surfactant in an incompatible solvent, placing this solvent at the interface dropwise, and then allowing the solvent containing the surfactant to evaporate. For this class of molecules, solubility is so low that deposited molecules remain on the surface in a long-term metastable state, remaining essentially static throughout the timeframe of an experiment (typically several hours).

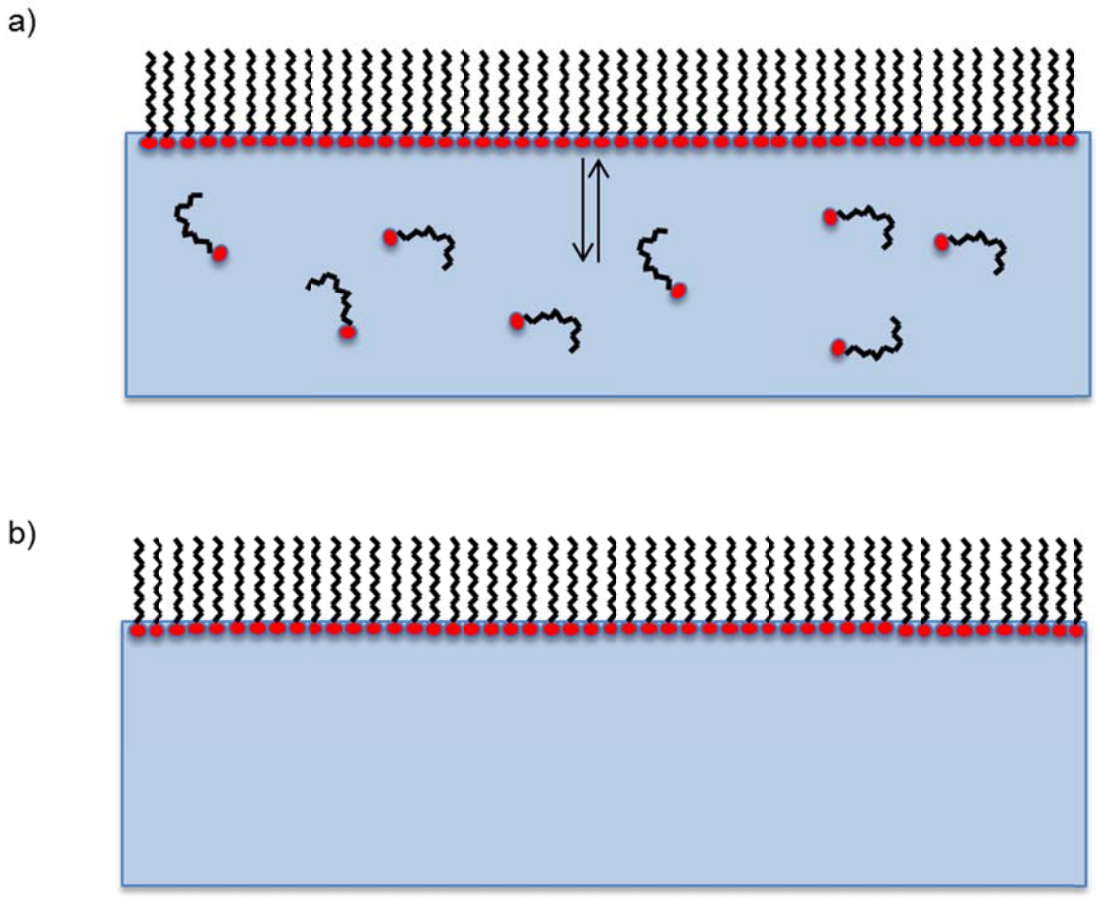

Figure 4.2: Comparison and contrast of Gibbs and Langmuir monolayers. A) A Gibbs monolayer, where equilibrium between surfactants in the bulk and the monolayer exists due to the surfactant being relatively soluble in solution. B) Langmuir monolayer, with a metastable monolayer of *insoluble* surfactants. These are directly applied to the surface to form the monolayer.

Langmuir monolayers are of particular interest because the dynamic nature of the liquid-vapor interface permits a high degree of self-organization. Additionally, thermodynamic parameters such as surface pressure and concentration can be directly measured and controlled. This allows for observation and study of multiple states of the monolayer as thermodynamic parameters are adjusted.

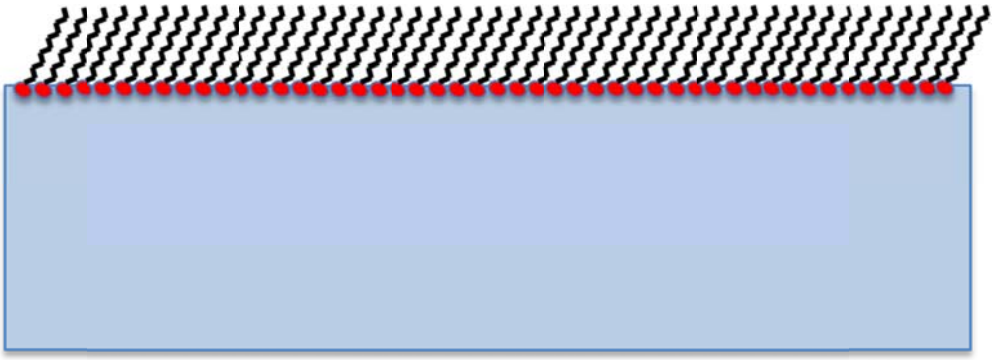

Figure 4.3: Control of parameters such as surface pressure and concentration may affect the packing structure of a monolayer. This example shows a tilted monolayer, in which hydrophobic chains take on a uniform tilt.

4.1.3 Fluorinated Surfactants

Insofar we have treated the terminology amphiphile and surfactant as interchangeable, but this is not always applicable. Amphiphiles act as ideal bridges between phases such as oil and water, and contains hydrophobic and hydrophilic moieties (Figure 1.5). A fluorinated surfactant exchanges its hydrophobic tail (generally

hydrogenated) for a fluorinated one. Fluorinated molecules are lipophobic, i.e. they are insoluble with hydrogenated phases. In addition to lipophobicity, fluorinated molecules are extremely hydrophobic. In fact, they are even less soluble in aqueous media than their hydrogenated counterparts. The incompatibility of fluorinated molecules, along with an attached hydrophilic moiety, renders them surface active, creating fluorinated surfactants. Langmuir monolayers formed by fluorinated surfactants are even more stable than monolayer formed by hydrogenated amphiphilic molecules due to the increased hydrophobicity of fluorinated surfactants.

4.1.4 Self-Assembly

It is unsurprising that surfactant composition so profoundly affects solubility. In a polar solvent, as the polarity of a hydrophilic headgroup increases, the molecule becomes increasingly soluble. Conversely, as the tail group becomes increasingly nonpolar, solubility decreases. Even seemingly small changes such as surfactant tail length are more than enough to affect solubility and self-assembly. Incompatibility with solvent encourages self-assembly of the surfactant molecules to minimize unfavorable intermolecular interactions. 3D self-assembly begins at the critical micellar concentration (CMC). Surfactants aggregate spontaneously above this concentration, and form micelles and vesicles to minimize their free energy (see Figure 4.4), sequestering hydrophobic moieties to the interior of an aggregate to minimize unfavorable interactions. The specific structure of the aggregate varies based on the shape and properties of each surfactant. When the headgroup of the amphiphile is strong compared to the hydrophobic part, micelles form. When the headgroup is

relatively weak, vesicles form.[1] As can be seen in Figure 4.4, micelles are obviously limited in size to approximately twice the molecular length, while such considerations do not affect vesicles as profoundly. Micelle formation grants many of the properties that allow surfactants to act as wetting agents, emulsifiers, foaming agents, and detergents, and are thus studied with great interest.

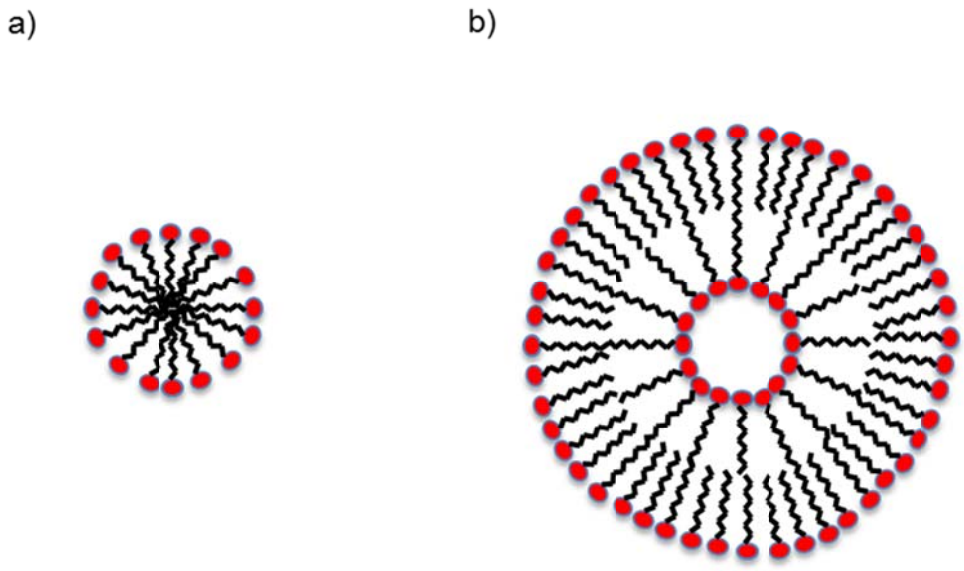

Figure 4.4: Comparison of vesicle and micelles. Micelles form when the headgroup of an amphiphilic molecule is strong compared to the hydrophobic part, and vesicles form in other cases. A) Micelle B) Vesicle.

Classical treatment of micelle thermodynamics was proposed by Debye[4], and further developed by Tanford.[5, 6] The treatment is based on mass action aggregation, where an equilibrium is established between N surfactant monomers, and aggregates with an equilibrium constant K.

$$nA \leftrightarrow A_n \quad \text{(eq 4.1)}$$

This formulation provides an accurate description of the aggregations process, and suggests an approximate value of the CMC.

$$\mathrm{CMC} \approx (\mathrm{NK})^{-1/\mathrm{n}} \quad \text{(eq 4.2)}$$

At even higher concentrations, the micelles themselves may begin to form lyotropic liquid crystals, or the surfactants themselves may adopt long range order such as a lamellar phase (see Chapter 1.1.3 for more discussion of lyotropic liquid crystals).

4.1.5 Interfacial properties

Micelle and vesicle formation, however, are bulk phenomenon. Rather than studying bulk surfactant properties such as micelles and vesicles, we restrict our self-assembly studies to the interfacial layer. New terminology must be introduced in order to thoroughly describe the thermodynamic parameters used to control interfacial phenomena. Parameters such as temperature and pressure are familiar, but the properties measured in 2D monolayers such as surface pressure and molecular area are less so. Surfactants are well-known to affect surface tension (see Chapter 5.1.8). Surface pressure tracks the differential between the surface tension of the pure liquid and the film-covered liquid. It is defined as follows:

$$(\Pi = \gamma_0 - \gamma) \text{ (eq 4.3),}$$

where Π is surface pressure, γ_o is the surface tension of the pure liquid, and γ is the surface tension of the liquid with a monolayer applied.

Surface pressure, along with the molecular area, quantifies the intermolecular forces within the monolayer. Molecular area, also referred to as area per molecule, is defined as the film area divided by the total number of molecules. It is calculated using the expression

$$a = \frac{AM}{CN_A V} \quad \text{(eq 4.4)},$$

where a is the area/molecule, A is the film area, M is the molecular weight of the monolayer material, C is the concentration of the spreading solutions in units of mass/volume, N_a is Avogadro's number, and V is the volume of the deposited solution. Molecular area greatly influences the behavior of the monolayer, and is controlled by varying the density of the molecules during an experiment in a specially designed apparatus, the Langmuir trough.

4.1.6 Langmuir trough

In a Langmuir trough, monolayers are deposited between specially designed movable barriers (see Figure 4.5). Modern troughs have a computerized feedback mechanism that allows control of barrier speed, surface pressure, and compression area. The computer also provides constant monitoring of surface pressure. The trough is generally made of Teflon or similar fluoropolymer to ensure that the trough itself is inert. This also allows for thorough cleaning, as the presence of any surface active molecule, e.g. oils or detergents, will contribute to significant error in surface pressure measurements.

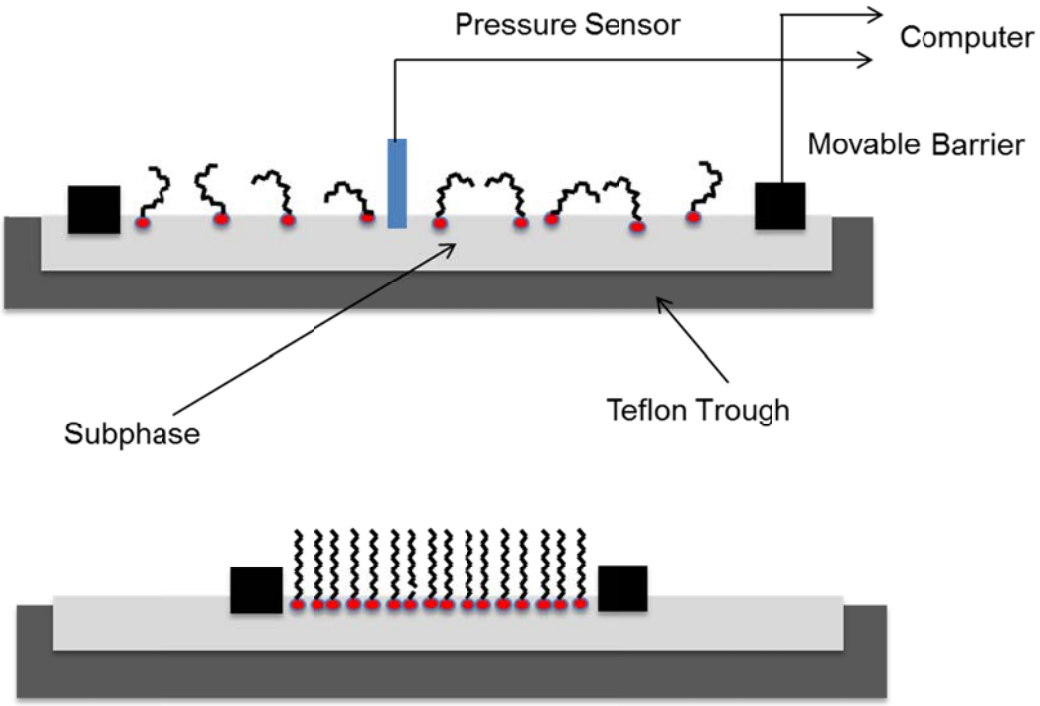

Figure 4.5: Schematic of a Langmuir trough in varying stages of monolayer compression. A) Descriptions of each working component of a Langmuir trough. B) Langmuir trough with barriers compressing the surface monolayer.

4.1.7 Langmuir-Blodgett transfer

To more closely examine monolayers, they can be transferred to a solid support so that additional characterization techniques such as atomic force microscopy (AFM) may be used[7-9]. If a Langmuir trough is designed for Langmuir-Blodgett transfer, a well is included in the design to accommodate the transfer substrate (Figure 4.6). The feedback-controlled barriers are then used to hold surface pressure steady during transfer, which minimizes transfer effects due to monolayer depletion, as removing a portion of the monolayer obviously reduces surface concentration/pressure. Langmuir-Blodgett transfer can even be repeated as a means to build up a controlled multilayer.

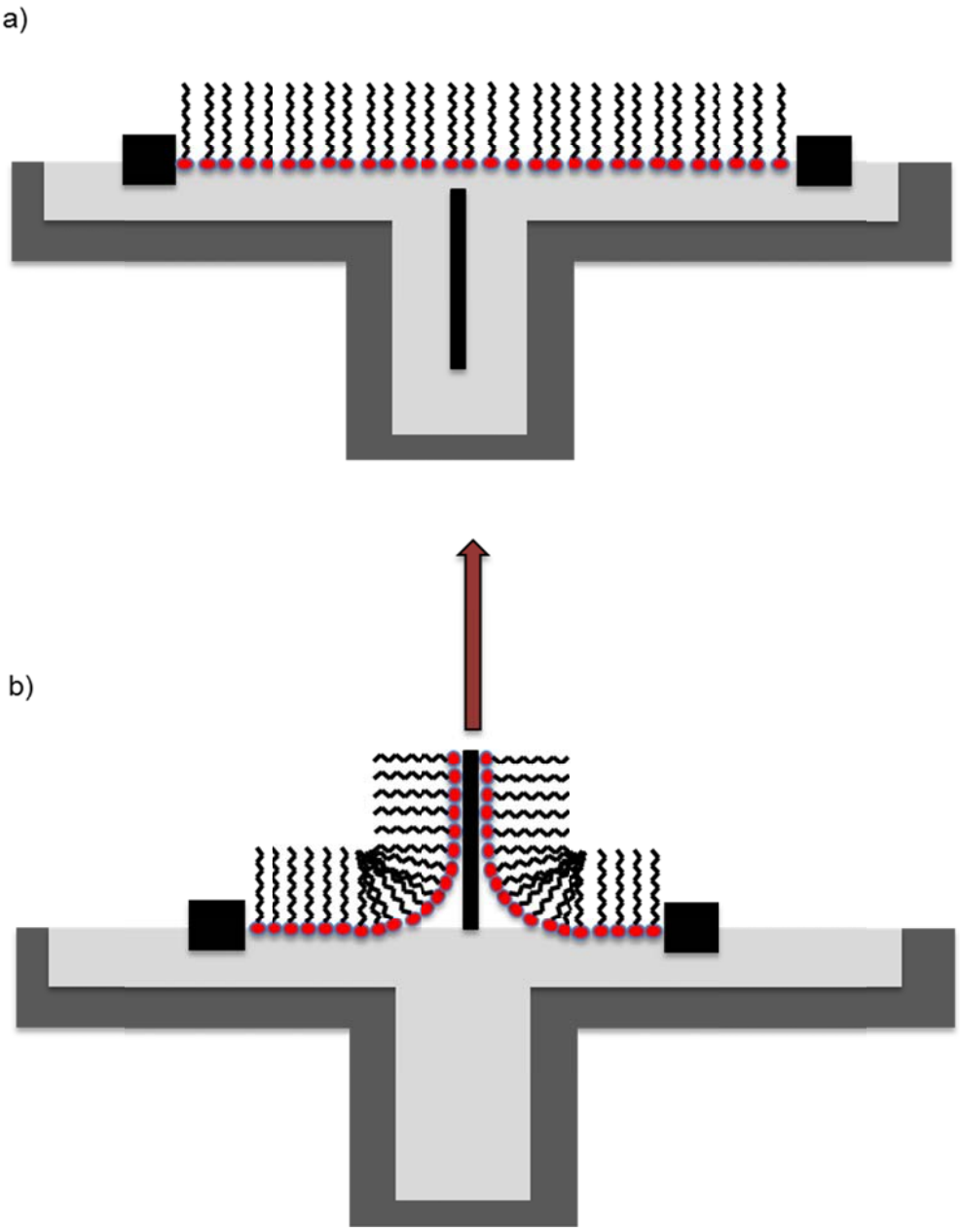

Figure 4.6: Scheme of Langmuir-Blodgett transfer. A) Monolayer is compressed to desired surface pressure B) The substrate is drawn through the interface, with the Langmuir film transferred to that surface. The movable barriers can be held at a constant pressure to facilitate even monolayer transfer.

4.1.8 Monolayer phases

Mobile trough barriers allow explicit, user-designed control of thermodynamic parameters. Increased monolayer compression (reduced molecular area) leads to varying phase behaviors within the monolayer. Just as in three dimensional materials, monolayers also exist in distinct phases. As one can imagine, gaseous, liquid-expanded, and condensed phases represent increasing levels of monolayer compression. In the "gaseous" phase, the molecules are dispersed, and the area per molecule is much larger than the dimensions of an individual molecule. Because few intermolecular interactions exist within the monolayer, this phase is considered analogous to the 3D gaseous phase. Typical molecular areas are 4 nm^2 or greater. Upon further compression, the gaseous phase transitions to the liquid-expanded phase. In this phase, the area per molecule is much less than that of the gaseous phase, but still significantly greater than what would be expected of a cylindrical fatty acid molecule. The liquid-expanded phase is often labeled as L_1. Typical molecular areas range from approximately 0.4-2 nm^2. Further compression results in the condensed phase, where molecules become well-ordered. Within the condensed phases, there are several naming anachronisms related to historical studies of LB films. Condensed phases include the L_2, L_2' (liquid condensed), LS (superliquid), S (solid), and CS (close-packed solid). These names represent historical assumptions that these states were liquid-like, though we now know that these phases exhibit distinct x-ray diffraction peaks, thus establishing solid-like molecular order. Condensed phases tend to exist from approximately 0.3-0.4 nm^2. Further compression leads to collapse, where material is forced out of the monolayer.[10-13]

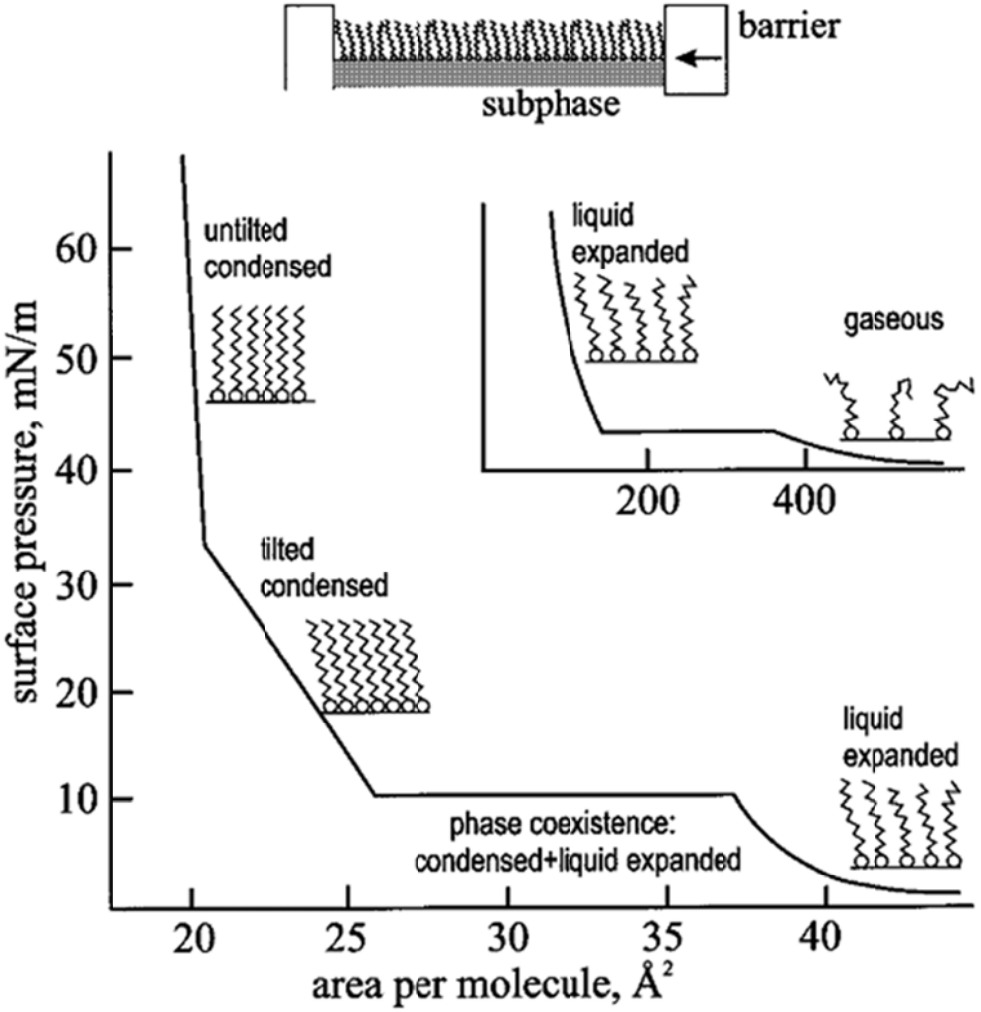

Figure 4.7: Figure representing the different phases of a compressed monolayer.[10]

4.1.9 Langmuir film applications

Monolayers and multilayer films resemble naturally occurring biological membranes which are comprised of phospholipids, an additional class of surfactant. Specifically, bilayers are used as stand-ins for cellular membrane studies; by adjusting composition, specific behaviors can be tailored.[14] It is possible to model the distinct domains that form within cell membranes, which often facilitate ion transport. Langmuir monolayers have been employed extensively as model systems for studies of thermodynamics and phase-transitions in two-dimensional biological systems including lipid rafts,[15] cell membranes,[15, 16] pulmonary surfactants,[16, 17 , 18 19] sensors,[20-22] and biomimetic applications.[13, 22, 23] Langmuir-Blodgett transfer permits creation of supported membranes for biomimetic studies, and allows additional characterization methods that are not feasible at the gas/liquid interface such as AFM.

4.1.10 Linactants

Rather than study the well-known phenomena of surfactants forming liquid crystalline mesophases, our work focuses on a lesser known species of interest, the linactant. Linactants function as a 2D analogue to surfactants. Rather than decrease surface tension, linactants work to decrease line tension (i.e. the interfacial force that favors round domains within a monolayer) in one dimension, and to reduce the interfacial energy related to domain formation in partitioned monolayers.[24-26] Line active materials are important because of their effects on models systems such as biological membranes. Current theories suggest that distinct lipid domains form within these membranes, with some molecules acting as linactants to facilitate the phase boundaries

of the system, the way a surfactant partitions to the interface in a 3D system. Chemically dissimilar molecules in a multicomponent Langmuir monolayer will phase separate within the monolayer. One such example is mixtures of hydrogenated and fluorinated surfactants. As fluorinated surfactants are lipophobic as well as hydrophobic,[27] they are immiscible with hydrogenated surfactants. This encourages the formation of distinct, immiscible domains of hydrogenated and fluorinated surfactants. Just as surfactants can act as emulsifiers and stabilizing agents between immiscible oil/water phases, linactants tend to partition between these immiscible monolayer components, decreasing the line energy, and therefore the free energy of the system.[28] It is well known that surfactants begin to self-assemble in three dimension into vesicles and micelles, and it has been suggested that 2D micelles of these linactants may be able to form at the interface[29], but this has yet to be proven definitively.

Fluorinated surfactants are used in biomedical applications[30] as well as monolayer patterning.[1] This makes previous work that linactants can be rationally designed for hydrogenated/fluorinated systems particularly interesting.[26] Previous work shows that linactants form nanoclusters and other unique molecular assemblies similar to surfactant soltions,[24, 31-37] as well as stabilize coexisting nanoscale domains by reducing line tension. We, however, will demonstrate how the observed aggregates are analogous, but also fundamentally different from 3D micelles. In order for applications to be fully realized, more extensive studies of self-assembly properties must be undertaken. As such, it is imperative to fully understand the partitioning of linactants at the liquid-vapor interface. Through observation of the linactant 12,12,13,13,14,14,15,15,16,1617,17,18,18,19,19-heptadecafluorononadecyl

phosphonic acid (F8H11) and perfluoroundecanoic acid (F10) (see Figure 4.8), it is apparent that long range order is not unique surfactants in three dimension, but is extended to the two dimensional monolayer. Langmuir-Blodgett transfer as well as atomic force microscopy (AFM) is used to explore the phase separation and packing of F10 and F8H11.

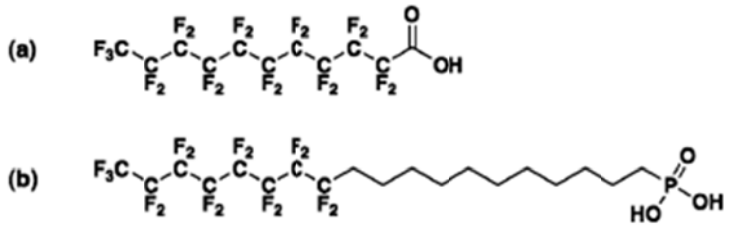

Figure 4.8: Molecular structures of F8H11 and F10

4.2 Results and Discussion

4.2.1 Isotherms of F8H11/F10 mixed monolayers

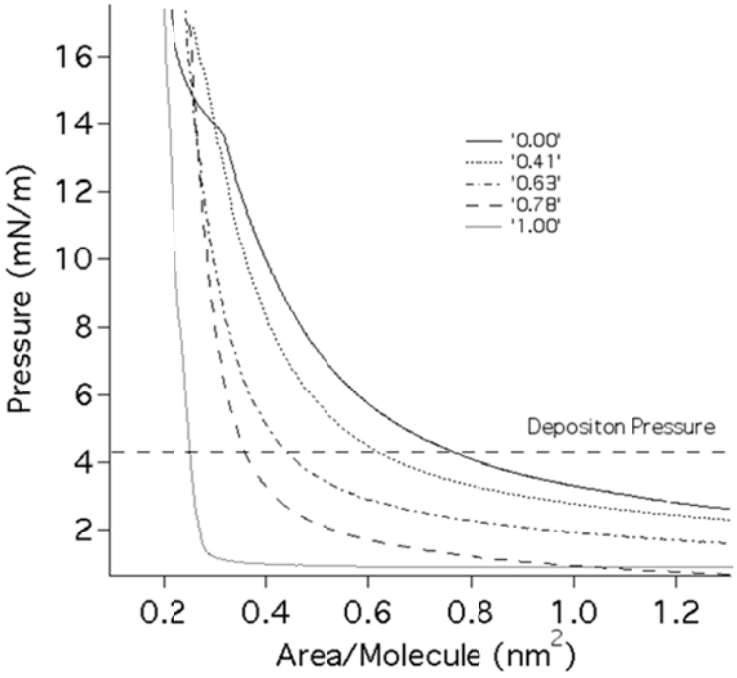

Figure 4.9: Representative isotherms of mixed F8H11 monolayers. Labels indicate the mole fraction of F8H11. The dashed lines represent the surface pressure at which films were transferred.

Measuring isotherms of the varying F8H11/F10 mixtures assists in elucidating the phase behavior of linactant mixtures by indicating the monolayer phase at a given pressure, and by testing for phase coexistence. Isotherms also allow direct comparison of the area per molecule to the phases observed via AFM. Figure 4.9 shows surface pressure versus molecular area isotherms of monolayers comprised of F10, F8H11, and several representative mixtures of the two. Labels represent the mole fraction of

F8H11. The isotherm of pure F10 (0.00) exhibits a gradual increase in surface pressure with decreasing molecular area that is suggestive of a 2D condensed phase (e.g. a 2D liquid or L_1 phase over a very large range of molecular area).[38 39] The kink in the isotherm at 14 mN/m also indicates another condensed phase, but as this is far outside of the deposition pressure of 4.3 mN/m, it is irrelevant to the current experiments. The surface pressure of F8H11, on the other hand, remains very low as the monolayer compressed until it finally rises sharply at ~0.3 nm^2/mol, which represents approximate molecular close-packing for a fluorinated surfactant.[33] This type of isotherm often indicates that the monolayer condenses into domains of a dense 2D "solid" phase, initially separated by regions of 2D vapor.[1, 40-42]

The rise in surface pressure corresponds to the area at which these solid domains come into contact. This type of transition occurs as the crystallinity of the monolayer increases. Because temperature and surface pressure is held constant throughout all measurements, only the differing molecular composition can cause the sharp transition from expanded to condensed phases. Isotherms of mixtures where the mole fraction of F8H11 is < 0.63 exhibit qualitative features similar to the pure F10 isotherm, which include gradual increase in surface pressure in the deposition regime, suggesting liquid-like behavior. Isotherms of mixtures with larger F8H11 mole fractions exhibit solid-like behavior reminiscent of pure F8H11 monolayers, indicated by the sharp increase of area per molecule compared to surface pressure at the deposition pressure.

4.2.2 AFM analysis of F8H11/F10 mixed monolayers

The solid-like behavior of F8H11 and the liquid-like behavior of F10 is confirmed with AFM analysis of the Langmuir-Blodgett films. While AFM images of pure F10 monolayers are featureless, for F8H11 mole fractions ≥0.02, AFM images exhibit roughly circular features that are raised 1.4 ± 0.3 nm above the background (see Figure 4.10). The characteristic lateral dimension of the features is 34±7 nm[37] and the features are essentially monodisperse in size. Both the apparent height and lateral dimension were found to be approximately independent of F8H11 concentration, again indicating that the packing of F8H11 and F10 did not change with concentration, but rather, only the mole fraction of the two molecules changed. This again indicates that F8H11 is close-packed in solid-like domains, while the liquid-like F10 is in an expanded phase, where its conformation is much less well defined. As fluorinated and hydrogenated amphiphiles are chemically incompatible, it is unsurprising that the fluorinated molecules phase separate.

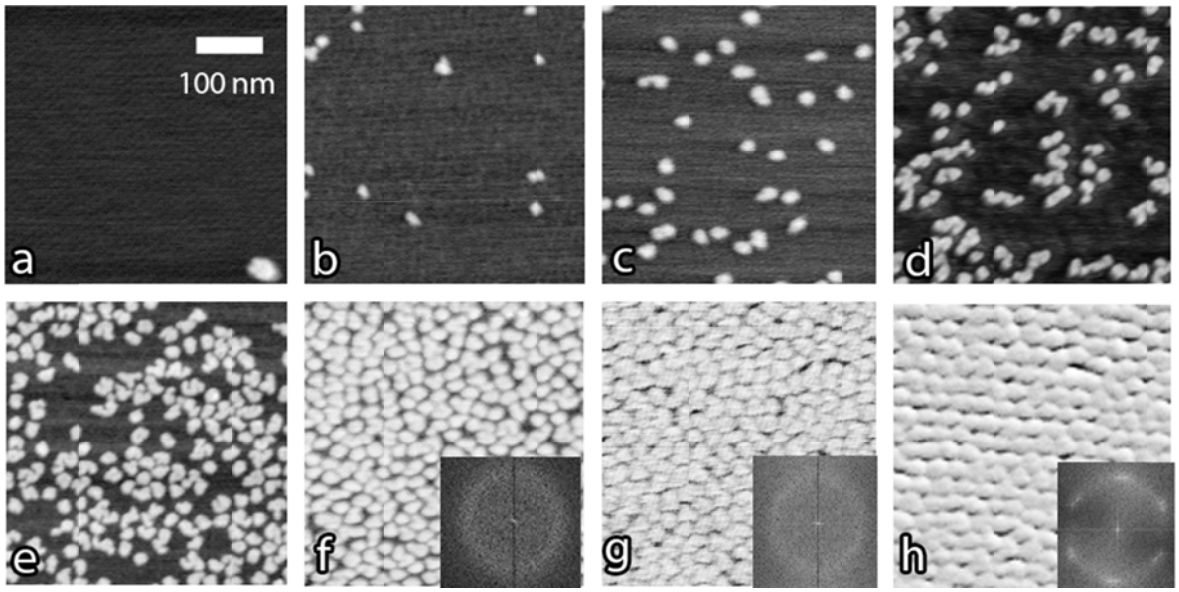

Figure 4.10: Representative AFM images of mixed F8H11/F10 LB monolayers at the specified mole fractions. The annotation indicates the F8H11 mole fraction. Fourier transforms are inset in higher F8H11 concentrations where order is found. a) 0.02 b) 0.15 c) 0.26 d) 0.41 e) 0.63 f) 0.78 g) 0.95 h)1.00

The number density of features increases systematically with the F8H11 mole fraction, as shown in Figure 4.10, again suggesting that the features may represent clusters of F8H11 molecules. At low F8H11 mole fractions (4.10 a-e), the features are dilute and randomly located, with no evidence of long-range order. However, at high F8H11 mole fractions the features are locally organized in a hexagonal arrangement, (indicated by the diffuse rings in the FFTs included as insets in Figure 4.10 f,g,h); it is interesting to note that the onset of the local hexagonal order corresponds approximately to the F8H11 concentration at which the monolayer become fairly incompressible at the experimental surface pressure, e.g. the surface pressure vs. area isotherm exhibited solid-like behavior and rapidly increases with increasing surface pressure. Figure 4.11 shows representative radial FFTs prepared as described above. While the position of the peak associated with the cluster packing changes very little with F8H11 concentration, the peak clearly narrows with increasing concentration, indicating that the degree of long range order increases with F8H11 concentration. The peaks in the figure are offset vertically for ease of interpretation. The peak locations are all very similar, indicating again that the aggregate size is independent of the cluster surface concentration. Table 4.1 gives the details cluster spacing and the correlation length of local hexagonal order obtained from analyzing the Figure 4.11.

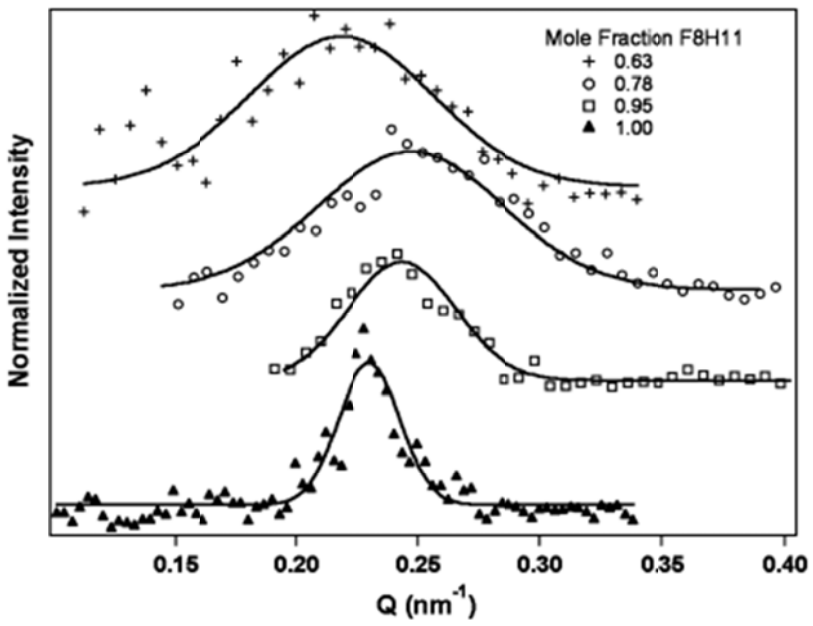

Figure 4.11: Radial Fourier transforms of reprentative AFM imagfe of FH11/F10 mixtures that exhibit hexaganol order of linactant clusteres. The annotation indicattes F8H11 mole fraction, and the lines are the best fit to a Gaussian function., Normalized represnetation of the gaussians calculated from fourier transfrms. Gaussians were normalized in the y direction and offset for comparison.

% F8H11	FWHM (from fit)	Correlation Length (nm)	Q (center of peak)	Row spacing (nm)
1.0	0.017±.004	118±28	0.235±.005	26.7±.05
0.95	0.033±0.009	61 ± 13	0.24 ±0.01	26 ±1
0.78	0.055±0.008	36 ± 5	0.23±0.01	27±1
0.63	0.049±.02	41 ± 16	0.22 ± .01	28 ±1

Table 4.1: Cluster spacing and correlation length of hexagonal packing from FFT analysis.

4.2.3 Cluster aggregation

We hypothesize that the features observed in AFM images represent self-limiting clusters composed predominantly of F8H11. Figure 4.12 shows a schematic diagram of such a cluster that is consistent with our results. Several observations support this hypothesis. For example, the apparent height of the feature in AFM images is consistent with the difference in molecular length between F8H11 and F10. Additionally, the number and area fraction of features increases systematically with F8H11 concentration. Furthermore, the lateral size of the features is highly monodisperse and does not vary with F8H11, nor is it affected by annealing time or compression speed.[25] These observations suggest that the clusters represent

equilibrium objects. If the hypothesis described above is correct, the clusters observed contain several thousand molecules ~2000.

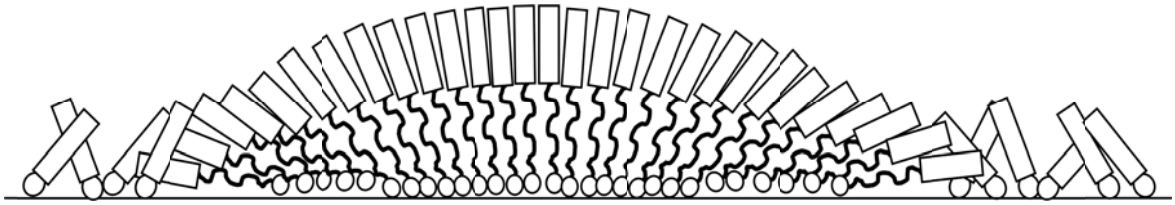

Figure 4.12: Proposed molecular configuration of nanoclusters.

In contrast to these nanoclusters, a typical 3D micelle has an aggregation number of ~50. Nevertheless, the behavior observed as a function of linactant concentration is fundamentally consistent with the thermodynamics of micelle formation. The above data leads to two independent methods to calculate the aggregation number of molecules in each cluster: one from the dependence of cluster density of F8H11 concentration, and the other from directly measurements of cluster area divided by the molecular area. Comparing the values calculated in these ways test the micelle hypothesis. The increase in number of clusters with F8H11 concentration, taken from the slope of the fit in Figure 4.13, is consistent with an aggregation number of 2000 ± 100 molecules F8H11 per cluster. Using an average size cluster area of 620 ± 90 nm^2 from AFM measurements and a molecular area of 0.28 nm^2 (from isotherms) gives an aggregation number of 2200 ± 300 nm^2. These are nominally equivalent within experimental uncertainty. The consistency of these values supports the hypothesis that the cluster molecules represent micelles composed of F8H11.

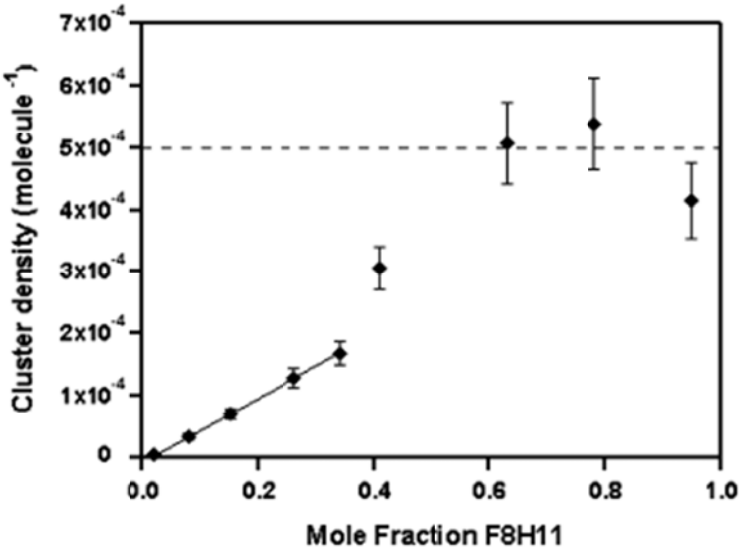

Figure 4.13: The number of features per μm^2 as a function of F8H11 mole fraction. The solid line is a linear fit to the first five data points, and the dashed line represents the approximate close packed cluster density.

4.2.4 Proposed structure due to packing frustration

We[24] ,and others[43], have previously suggested that clusters of this type may be due to an intrinsic packing frustration between hydrocarbon and fluorocarbon segments that leads to curved aggregates such as the one shown in Figure 4.12. Such aggregates are fundamentally different from surface hemimicelles (or admicelles) [44-58], which are structurally similar to 3D micelles and exhibit characteristic dimensions related to twice the molecular length. A hemimicelle is merely half of a standard 3D micelle, adsorbed onto a surface. The characteristic lateral dimension of the clusters observed here is roughly an order of magnitude larger, while 3D micelles typically have an aggregation number for 50-100. The 2D geometry of the proposed nanoclusters

permits greater flexibility in domain size, as the third embedding dimension provides additional options for structures that separate chemically incompatible moieties.

4.2.5 Hexatic liquid crystalline domains in 2D

At high linactant concentrations, local hexagonal packing of clusters was observed, and the correlation length of this hexagonal packing increased systematically with linactant concentration (4.10 f-h). These structures are consistent with a liquid crystalline (e.g. hexatic) phase of clusters. In fact, in a monolayer of 100% F8H11, correlations are sufficiently long-range that orientational order is explicitly demonstrated by the presence of diffuse spots in the FFT (in contrast with the continuous ring seen for lower concentrations). The diffuse rings at mole fractions of 0.78 and 0.95 F8H11 indicate hexagonal order, but with extremely low long range order. This says that there are many small regions with hexagonal order, but because these small domains are not close-packed, there is equivalent order in all directions. In the pure F8H11 monolayers, the diffuse spots indicate that there is only defined order in 6 directions, indicating hexagonal close-packing with long-range order. These observations suggest that the increasing area fraction of clusters leads to a 2D phase transition from an isotropic micellar phase to a liquid crystalline phase with local hexagonal packing of clusters. This packing is analogous to the lyotropic crystalline phases that are common with surfactants in 3D solutions, exhibiting long range order, with regular, defined packing of micelle-like clusters.

4.3 Conclusions

Two-component Langmuir monolayers composed of semi-fluorinated and perfluorinated amphiphiles exhibited behavior that was quantitatively consistent with the formation of 2D micelles. The semi-fluorinated compound, previously shown to be line-active at the interface between hydrocarbon and fluorocarbon domains within monolayers,[24, 26] played the role of 2D surfactant (linactant) and the perfluorinated compound acted as the 2D analogue of solvent. Above the critical linactant mole fraction of 0.013 F8H11, AFM images showed the presence of monodisperse 2D molecular clusters within these monolayers. In analogy with 3D micelles, the number of clusters increased with linactant concentration while their size remained the same. A transition from an isotropic 2D micellar phase to a phase where the clusters exhibited local hexagonal packing was observed at a linactant mole fraction of ~0.63; the correlation length of the hexagonal packing increased with linactant mole fraction. In contrast with 3D micelles, the characteristic lateral dimension of the 2D micelles was much larger than molecular dimensions, suggesting that the finite size of the aggregate was due to subtle packing incompatibility between the hydrocarbon and fluorocarbon blocks in the linactant tailgroup.

4.4 References

1. Petty, M. C., *Langmuir-Blodgett Films: An Introduction*. Cambridge University Press: Cambridge, 1996.

2. Price, A. D.; Ignes-Mullol, J.; Angels Vallve, M.; Furtak, T. E.; Lo, Y.-A.; Malone, S. M.; Schwartz, D. K., Liquid crystal anchoring transformations induced by phase transitions of a photoisomerizable surfactant at the nematic/aqueous interface. *Soft Matter* **2009,** 5, (11), 2252-2260.

3. Price, A. D.; Schwartz, D. K., Fatty-Acid Monolayers at the Nematic/Water Interface: Phases and Liquid-Crystal Alignment. *J. Phys. Chem. B* **2007,** 111, (5), 1007-1015.

4. Debye, P., Light Scattering in Soap Solutions *Annals of the New York Academy of Sciences* **1949,** 51, (4), 575-592.

5. Tanford, C., Theory of Micelle Formation in Aqueous Solutions. *Journal of Physical Chemistry* **1974,** 78, (24), 2469-2479.

6. Tanford, C., Thermodynamics of Micelle Formation - Prediction of Micelle Size and Size Distribution *Proceedings of the National Academy of Sciences of the United States of America* **1974,** 71, (5), 1811-1815.

7. Zasadzinski, J.; Viswanathan, R.; Madsen, L.; Garnaes, J.; Schwartz, D., Langmuir-Blodgett films. *Science* **1994,** 263, (5154), 1726-1733.

8. Schwartz, D. K., Langmuir-Blodgett film structure. *Surface Science Reports* **1997,** 27, (7-8), 245-334.

9. Blodgett, K. B., Films built by depositing successive monomolecular layers on a solid surface. *Journal of the American Chemical Society* **1935,** 57, (1), 1007-1022.

10. Kaganer, V. M.; Mohwald, H.; Dutta, P., Structure and phase transitions in Langmuir monolayers. *Review of Modern Physics* **1999,** 71, (3), 779-819.

11. Knobler, C. M.; Desai, R. C., Phase-Transitions in Monolayers. *Annual Review of Physical Chemistry* **1992,** 43, 207-236.

12. Knobler, C. M.; Schwartz, D. K., Langmuir and self-assembled monolayers. *Current Opinion in Colloid & Interface Science* **1999,** 4, (1), 46-51.

13. Gaines, G. L., *Insouble Monolayers at Liquid-Gas Interfaces*. Interscience Publishers: New York, 1966.

14. Guo, W.; Photos, P. J.; Vanderlick, T. K., Polymer Enhanced Fusion of Model Sperm Membranes as Induced by Calcium. *Industrial & Engineering Chemistry Research* **2006,** 45, (16), 5512-5517.

15. Rinia, H. A.; de Kruijff, B., Imaging domains in model membranes with atomic force microscopy. *FEBS Letters* **2001,** 504, (3), 194-199.

16. Benvegnu, D. J.; McConnell, H. M., Line Tension Between Liquid Domains in Lipid Monolayers. *Journal of Physical Chemistry* **1992,** 96, (16), 6820-6824.

17. Discher, B. M.; Maloney, K. M.; Grainger, D. W.; Hall, S. B., Effect of neutral lipids on coexisting phases in monolayers of pulmonary surfactant. *Biophys. Chem.* **2002,** 101, 333-345.

18. Ding, J. Q.; Doudevski, I.; Warriner, H. E.; Alig, T.; Zasadzinski, J. A., Nanostructure changes in lung surfactant monolayers induced by interactions between palmitoyloleoylphosphatidylglycerol and surfactant protein B. *Langmuir* **2003,** 19, (5), 1539-1550.

19. Gopal, A.; Lee, K. Y. C., Morphology and collapse transitions in binary phospholipid monolayers. *J. Phys. Chem. B* **2001,** 105, (42), 10348-10354.

20. Zou, L. N.; Li, Y. M.; Ye, B. X., Voltammetric sensing of guanine and adenine using a glassy carbon electrode modified with a tetraoxocalix[2]arene[2]triazine Langmuir-Blodgett film. *Microchim. Acta* 173, (3-4), 285-291.

21. Charych, D. H.; Nagy, J. O.; Spevak, W.; Bednarski, M. D., Direct Colorimetric Detection of A Receptor-Ligand Interaction by a Polymerized Bilayer Assembly *Science* **1993,** 261, (5121), 585-588.

22. Caseli, L.; Perinotto, A. C.; Viitala, T.; Zucolotto, V.; Oliveira, O. N., Immobilization of Alcohol Dehydrogenase in Phospholipid Langmuir-Blodgett Films To Detect Ethanol. *Langmuir* **2009,** 25, (5), 3057-3061.

23. Aoki, P. H. B.; Volpati, D.; Riul, A.; Caetano, W.; Constantino, C. J. L., Layer-by-Layer Technique as a New Approach to Produce Nanostructured Films Containing Phospholipids as Transducers in Sensing Applications. *Langmuir* **2009,** 25, (4), 2331-2338.

24. Trabelsi, S.; Zhang, S.; Lee, T. R.; Schwartz, D. K., Linactants: Surfactant analogues in two dimensions. *Physical Review Letters* **2008,** 1, (3).

25. Trabelsi, S.; Zhang, S. S.; Zhang, Z. C.; Lee, T. R.; Schwartz, D. K., Semi-fluorinated phosphonic acids form stable nanoscale clusters in Langmuir-Blodgett and self-assembled monolayers. *Soft Matter* **2009,** 5, (4), 750-758.

26. Trabelsi, S.; Zhang, Z.; Zhang, S.; Lee, T. R.; Schwartz, D. K., Correlating Linactant Efficiency and Self-Assembly: Structural Basis of Line Activity in Molecular Monolayers. *Langmuir* **2009,** 25, (14), 8056-8061.

27. Riess, J. G.; Krafft, M. P., Fluorinated materials for in vivo oxygen transport (blood substitutes), diagnosis and drug delivery. *Biomaterials* **1998,** 19, (16), 1529-1539.

28. Brewster, R.; Pincus, P. A.; Safran, S. A., Hybrid Lipids as a Biological Surface-Active Component. *Biophysical Journal* **2009,** 97, (4), 1087-1094.

29. Israelachvili, J., Self-Assembly in 2 Dimensions - Surface Micelles and DOmain Formation in Monolayers *Langmuir* **1994,** 10, (10), 3774-3781.

30. Krafft, M. P.; Riess, J. G., Highly fluorinated amphiphiles and colloidal systems, and their applications in the biomedical field. A contribution. *Biochimie* **1998,** 80, (5-6), 489-514.

31. Mourran, A.; Tartsch, B.; Gallyamov, M.; Magonov, S.; Lambreva, D.; Ostrovskii, B. I.; Dolbnya, I. P.; de Jeu, W. H.; Moeller, M., Self-assembly of the perfluoroalkyl-alkane F14H20 in ultrathin films. *Langmuir* **2005,** 21, (6), 2308-2316.

32. Maaloum, M.; Muller, P.; Krafft, M. P., Lateral and vertical nanophase separation in Langmuir-Blodgett films of phospholipids and semifluorinated alkanes. *Langmuir* **2004,** 20, (6), 2261-2264.

33. Krafft, M. P.; Goldmann, M., Monolayers made from fluorinated amphiphiles. *Current Opinion in Colloid & Interface Science* **2003,** 8, (3), 243-250.

34. Kato, T.; Kameyama, M.; Ehara, M.; Iimura, K., Monodisperse two-dimensional nanometer size clusters of partially fluorinated long-chain acids. *Langmuir* **1998,** 14, (7), 1786-1798.

35. Zhang, G. F.; Maaloum, M.; Muller, P.; Benoit, N.; Krafft, M. P. In *Surface micelles of semifluorinated alkanes in Langmuir-Blodgett monolayers*, 2004; 2004; pp 1566-1569.

36. Trabelsi, S.; Zhang, Z.; Zhang, S.; Lee, T. R.; Schwartz, D. K., Correlating Linactant Efficiency and Self-Assembly: Structural Basis of Line Activity in Molecular Monolayers

doi:10.1021/la900565m. *Langmuir* **0,** 0, (0).

37. Trabelsi, S.; Zhang, S.; Lee, T. R.; Schwartz, D. K., Swelling of a cluster phase in Langmuir monolayers containing semi-fluorinated phosphonic acids. *Soft Matter* **2007,** 3, (12), 1518-1524.

38. Hifeda, Y. F.; Rayfield, G. W., Evidence for first-order phase transitions in lipid and fatty acid monolayers. *Langmuir* **1992,** 8, (1), 197-200.

39. Pallas, N. R.; Pethica, B. A., Liquid-expanded to liquid-condensed transition in lipid monolayers at the air/water interface. *Langmuir* **1985,** 1, (4), 509-513.

40. Barton, S. W.; Goudot, A.; Bouloussa, O.; Rondelez, F.; Lin, B. H.; Novak, F.; Acero, A.; Rice, S. A., Structural Transitions in a Monolayer of Fluorinated Amphiphile Molecules *Journal of Chemical Physics* **1992,** 96, (2), 1343-1351.

41. Fainerman, V. B.; Vollhardt, D., Equation of state for monolayers under consideration of the two-dimensional compressibility in the condensed state. *Journal of Physical Chemistry B* **2003,** 107, (14), 3098-3100.

42. Riviere, S.; Henon, S.; Meunier, J.; Schwartz, D. K.; Tsao, M. W.; Knobler, C. M., Textures and Phase Transitinos in Langmuir Monolayers of Fatty Acids - A Comparative Brewster-Angle Microscope and Polarized Fluorescence Microscope Study *Journal of Chemical Physics* **1994,** 101, (11), 10045-10051.

43. Pineiro, A.; Prieto, G.; Ruso, J. M.; Verdes, P. V.; Sarmiento, F., Surface films of short fluorocarbon-hydrocarbon diblocks studied by molecular dynamics simulations: Spontaneous formation of elongated hemimicelles. *Journal of Colloid and Interface Science* **2009,** 329, (2), 351-356.

44. Fuerstenau, D. W., Streaming Potential Studies on Quartz in Solutions of Aminium Acetates in Relation to the Formation of Hemi- micelles at the Quartz-Solution Interface. *The Journal of Physical Chemistry* **1956,** 60, (7), 981-985.

45. Gu, T.; Rupprecht, H., Hemimicelle shape and size. *Colloid & Polymer Science* **1990,** 268, (12), 1148-1150.

46. Cain, N.; Van Bogaert, J.; Gin, D. L.; Hammond, S. R.; Schwartz, D. K., Self-organization of a wedge-shaped surfactant in monolayers and multilayers. *Langmuir* **2007,** 23, (2), 482-487.

47. Ducker, W. A.; Wanless, E. J., Surface-aggregate shape transformation. *Langmuir* **1996,** 12, (24), 5915-5920.

48. Fuerstenau, D. W., Equilibrium and nonequilibrium phenomena associated with the adsorption of ionic surfactants at solid-water interfaces. *Journal of Colloid and Interface Science* **2002,** 256, (1), 79-90.

49. Fuerstenau, D. W.; Colic, M., Self-association and reverse hemimicelle formation at solid-water interfaces in dilute surfactant solutions. *Colloids and Surfaces a-Physicochemical and Engineering Aspects* **1999,** 146, (1-3), 33-47.

50. Grant, L. M.; Ducker, W. A., Effect of substrate hydrophobicity on surface-aggregate geometry: Zwitterionic and nonionic surfactants. *Journal of Physical Chemistry B* **1997,** 101, (27), 5337-5345.

51. Manne, S.; Cleveland, J. P.; Gaub, H. E.; Stucky, G. D.; Hansma, P. K., Direct Visualizatino of Surfactant Hemimicelles by Forrce Microscopy of the Electrical Double-Layer *Langmuir* **1994,** 10, (12), 4409-4413.

52. Manne, S.; Gaub, H. E., Molecular-Organization of Surfactants at Solid-Liquid Interfaces *Science* **1995,** 270, (5241), 1480-1482.

53. Manne, S.; Schaffer, T. E.; Huo, Q.; Hansma, P. K.; Morse, D. E.; Stucky, G. D.; Aksay, I. A., Gemini surfactants at solid-liquid interfaces: Control of interfacial aggregate geometry. *Langmuir* **1997,** 13, (24), 6382-6387.

54. Nelson, M.; Cain, N.; Taylor, C. E.; Ocko, B. M.; Gin, D. L.; Hammond, S. R.; Schwartz, D. K., Periodic arrays of interfacial cylindrical reverse micelles. *Langmuir* **2005,** 21, (22), 9799-9802.

55. Patrick, H. N.; Warr, G. G.; Manne, S.; Aksay, I. A., Surface micellization patterns of quaternary ammonium surfactants on mica. *Langmuir* **1999,** 15, (5), 1685-1692.

56. Wanless, E. J.; Davey, T. W.; Ducker, W. A., Surface aggregate phase transition. *Langmuir* **1997,** 13, (16), 4223-4228.

57. Wanless, E. J.; Ducker, W. A., Weak influence of divalent ions on anionic surfactant surface-aggregation. *Langmuir* **1997,** 13, (6), 1463-1474.

58. Wolgemuth, J. L.; Workman, R. K.; Manne, S., Surfactant aggregates at a flat, isotropic hydrophobic surface. *Langmuir* **2000,** 16, (7), 3077-3081.

Chapter 5

Experimental Details

5.1 Alkyl Chain Length affects Polar and Azimuthal Alignment

5.1.1 Liquid phase SAM preparation

Soda-lime glass slides (Fisher Scientific) were cleaned with piranha solution, which is comprised of 30% aqueous hydrogen peroxide (H_2O_2) and concentrated sulphuric acid (H_2SO_4), at a 1:3 volume ratio. This was then heated to 100˚C. Piranha solution reacts strongly with organic compounds and should be handled with extreme caution. Do not store solution in closed container. Alkylsilane self-assembled monolayers (SAMs) were prepared using the amine-catalyzed approach as described by Walba et al[1]. For discrete alkyl chain length SAMs, Octadecyltriethoxysilane (OTS or C18) decyltriethoxysilane (C10), hexyltriethoxysilane (C6), pentyltriethoxysilane (C5), butyltriethoxysilane (C4), propyltriethoxysilane (C3), ethyltriethoxysilane (C2), and methyltriethoxysilane (C1) were all manufactured. All silane compounds were obtained from Gelest at 97% purity and used as received.

After piranha cleaning, the slides are transferred to a micro-90 cleaned staining dish containing Milli-Q water (18.2 MΩ). The piranha-cleaned dish is then thoroughly dried in the oven to drive off any residual moisture. Coplin staining dishes are used because they allow processing of multiple microscope slides, but any glass vessel that

can withstand rapid heating is adequate. The reaction solution is primarily comprised of toluene, with 1.5 w/w% ethoxysilane, and 0.4 w/w% butylamine. For the specific case of the Coplin staining jar, this results in 60 mL toluene, 0.3 mL butylamine, 0.9 mL ethoxysilane. The reaction solution is then held at 60°C for 30 minutes. Other silanes can be used for this attachment chemistry, including -ethoxysilanes, -methoxysilanes, and -chlorosilanes. The prefix to the silane merely describes the leaving group, so all moieties result in chemically identical monolayers. The previous leaving silane leaving groups are listed in order of reactivity, from smallest to largest. Silanes with a higher reactivity react more quickly, but the increased reactivity leads to greater degree of polymerization rather than SAM formation.

This reaction is partially catalyzed by water in the system; Walba et al [1] have shown that the ideal amount of water is the trace amount already in the solvents. Additional water will result in polymerization both in the bulk of the reaction solution, as well as on the surface of the glass slides. The previously piranha-cleaned microscope slides are rinsed thoroughly with fresh Millipore water, and dried under nitrogen. They are then rinsed with toluene and placed in the previously warmed solution. The slides are then incubated for 30-60 minutes at 60 °C. Slides are then rinsed with toluene, and dried under nitrogen. SAMs are then stored under vacuum until use. The quality of these SAMs can be measured via contact angle goniometry.

5.1.2 Vapor Phase TMS SAM preparation

Trimethylsilane (TMS) SAMs were prepared by catalyst-free vapor deposition. Slides were piranha cleaned, then exposed to hexamethydisilazine vapor (99.8% purity, Acros Organic) for approximately 12 hours. The substrate was held approximately 2 cm above the liquid reserve.

5.1.3 SAM photolytic degradation

Substrates with a continuous gradient of surface properties were prepared as described previously. OTS SAM slides were cut in half and degraded by placing the slide adjacent to a mercury pen lamp (254 nm) for 7 minutes. The intensity was 3.6 $\frac{mW}{cm^2}$ at the point the sample was in contact with the lamp, and this dropped off to 0.3$\frac{mW}{cm^2}$ at the far end of the sample, ~4 cm away. This range of intensity is similar to other work with silane degradation[2-4]. The gradual decrease of the irradiation intensity as a function of distance from the lamp resulted in a continuous gradient of surface properties. There was some variability from sample to sample, therefore each substrate had contact angles independently measured along the gradient direction[5].

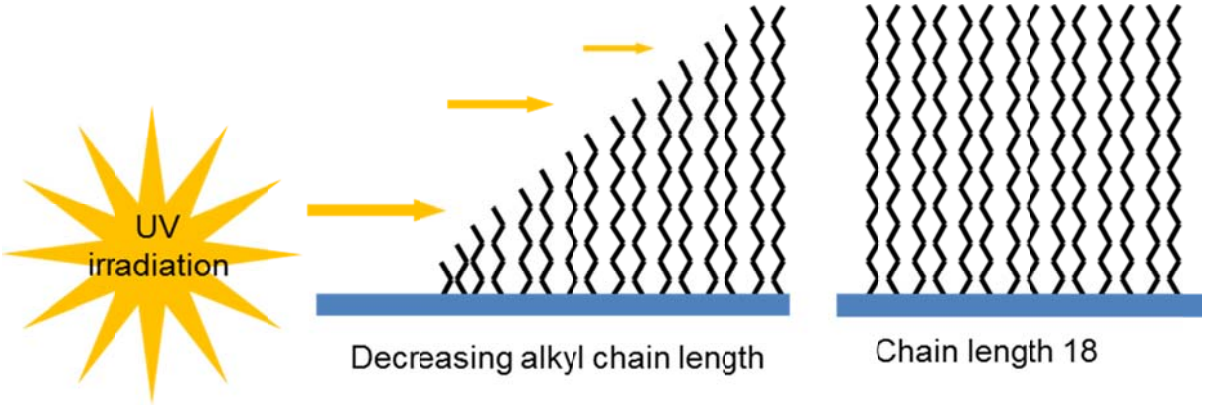

Figure 5.1: Schematic of UV irradiation for degrading octadecyltriethoxsilane SAMs. Irradiation was adjacent to sample, and increasing distance from UV source decreased UV intensity

5.1.4 Mechanical rubbing

Mechanical rubbing was performed using a custom-built rotating brush apparatus (Winston & Newton Series 240 brush). Each sample was brushed 100 times for uniformity. Samples were then placed in an ultrasonic cleaner in a solution of micro-90 and water for 10 minutes to remove any surface contamination, followed by rinsing in clean Millipore water. Samples were then blown dry with filtered nitrogen. For some substrates, half of the SAM was brushed, while half of the sample was shielded from brushing by covering with a piranha-cleaned glass slide to act as an internal control. Averages and standard deviations were calculated from six independent short chain SAMs and three irradiated SAMs. Chain lengths shorter than 18 (C1-C10 and TMS) were not irradiated.

5.1.5 Liquid crystal cell preparation

Hybrid aligned nematic (HAN) cells were made by cementing two SAMs with 10 μm glass fibers blended into 5 minute epoxy. The cells were then clamped with binder clips while the epoxy cured, while the glass fibers in the epoxy maintained uniform spacing. One bounding surface of each HAN cell was always an un-degraded OTS layer, producing uniform homeotropic anchoring. This was chosen because strong anchoring allows for a known polar boundary condition for birefringence calculation, and because it will not bias any azimuthal alignment induced by rubbing the opposite substrate. The other side of the HAN cell was the substrate of interest in each experiment: either a degraded OTS gradient SAM or an un-degraded shorter chain length SAM. Cell thickness was measured using interference fringes from monochromatic light transmitted through air.[6, 7] The HAN cells were filled with 4-n-pentyl-4'-cyanobiphenyl (5CB, Alfa Aesar, N-I transition 35.5 $^{\circ}$C) by capillary action while heating 5CB above its N-I transition to eliminate any flow alignment.

In cells that were not controlled for thickness, the above procedure was used with the following modifications: No epoxy was used to determine a finalized thickness of the cell. Approximate thickness was estimated using the Michel-Levy diagram (See Figure 1.9) and the known birefringence of 5CB. Thickness was determined to be 20-25 microns.

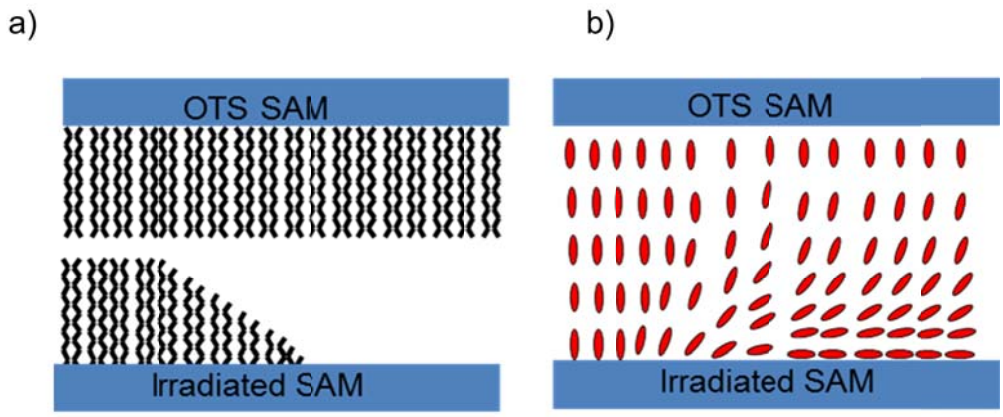

Figure 5.2: Schematic representation of Hybrid aligned nematic cell. a) SAMs associated with irradiated an OTS SAM in a HAN cell. b) Liquid crystal alignment associated with HAN cell.

5.1.6 Polarized light visualization (macroscopic)

After sample preparation, the HAN cells were viewed between crossed polarizers using a Lightbox light table. Images were captured with either a Cohu or an Artray digital CCD, with magnification up to 5x using a standard zoom lens. Light from the Lightbox table was not columnated, disallowing complete extinction from the liquid crystal cells.

5.1.7 Bereck compensator

Quantitative birefringence values were calculated from retardation measurements with an Olympus UCT-B Bereck compensator, illuminated with monochromatic light. Each data point reflects the mean and standard deviation of six individual measurements. Because of the changing tilt throughout the HAN cell, effective, rather than absolute birefringence, is measured. The optical effective

birefringence $\bar{n} = \bar{n}_e - n_o$ can be directly related to the tilt angle at the surface of interest,[8]

$$\bar{n}_e = \frac{1}{\theta_2 - \theta_1} \int_{\theta_1}^{\theta_2} \frac{n_\parallel n_\perp}{\sqrt{n_\parallel^2 cos^2\theta + n_\perp^2 sin^2\theta}} d\theta \quad \text{(eq. 5.1)},$$

where $n_\perp = n_o$ and is the index of refraction perpendicular to the optical axis, $n_\parallel$ is the index of refraction parallel to the optical axis[8]. This was integrated numerically by Mathematica to obtain values for θ_1. $\theta_2$was set to be 0.01, as the second surface of the HAN cell is known to give homeotropic alignment, but equation 5.1 is undefined if $\theta_2 = 0$. The refractive indices used were 1.523 and 1.729 for $n_\perp$and $n_\parallel$ respectively.[9]

5.1.8 Contact angle goniometry

Contact angle measurements were made using a custom built goniometer, using static drops[10] of Millipore water (18.2 MΩ). For gradient substrates, measurements were taken at 3 mm intervals along the gradient direction. Contact angle measurements were made on a minimum of three independent SAMs with ten samples at random positions on each SAM. According to Young's equation[11],

$$\gamma_{LV} cos\phi = \gamma_{SV} - \gamma_{SL}, \quad \text{(eq 5.2)}$$

where ϕ is the contact angle of water, γ_{LV}, γ_{SV}, γ_{SL} are the interfacial energies between the liquid/vapor, solid/vapor, and solid/liquid interfaces, respectively. The interfacial energy of the liquid/vapor interface is also known as the surface tension of the sample[12]. This shows that interfacial energy directly correlates to the cosine of the contact angle of the liquid.

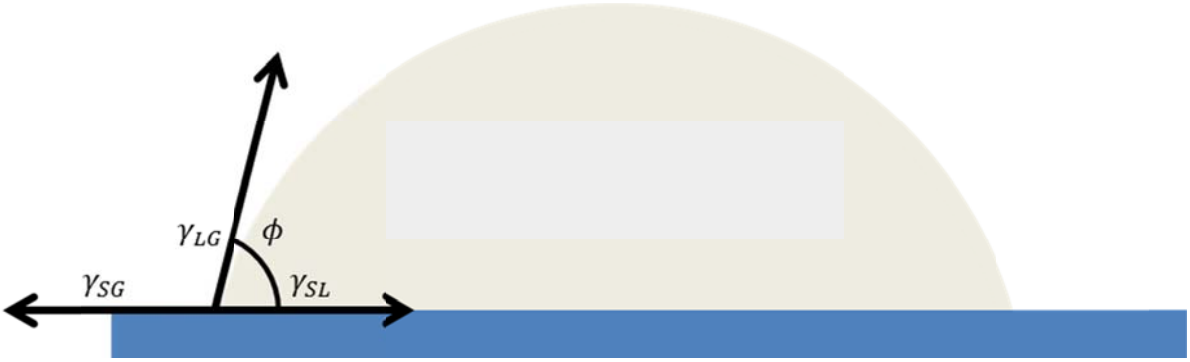

Figure 5.3: Schematic representation of Young's equation on a sessile drop for contact angle measurement. S is solid, L is liquid, and G is gas. Each surface energy represents the intersection between two phases.

5.2 Liquid Crystal Response to Isolated DNA Helices

5.2.1 DNA extension

DNA was diluted in a 1mM potassium phosphate dibasic buffer, with the pH adjusted to 8.0 using NaOH. Calf thymus (variable length, average 15,000 base pairs) and lambda phage (48,490 base pairs) DNA was extended using the molecular combing method.[13, 14] Calf thymus DNA was purified using phenol, chloroform, isoamyl alcohol extraction (25:24:1) and reconstituted using DNAase-free water. DNAase free water was created by autoclaving a 0.01% DEPC (diethylpyrocarbonate) solution, then autoclaving a second time to remove ethanol residue. Lambda DNA was used without any further purification. Specifically, glycidoxypropyltrimethoxysilane (GPTMS) SAMs were incubated 6–30 minutes in DNA solution before being drawn through the air-water interface at a rate of 10 mm/min. Solution concentrations ranging from 1 fM to 1 nM of lambda DNA resulted in surface concentrations ranging from 1–600 molecules in a 137

μm x 137 μm field of view. Prior to combing, dsDNA was labeled with YOYO-1 iodide (Invitrogen) at an approximate density of 20 base pairs per dye molecule. Company-supplied labeling protocols provide by the manufacturer were followed, i.e. labeling prior to solution at pH 8, and avoiding glass containers due the cationic dye binding irreversible with glass surfaces. Denatured/ssDNA was prepared by boiling lambda DNA in 2M urea at pH 8 for 30 minutes, followed by quenching the DNA solution in an ice bath. Teflon vessels were used for incubation to minimize DNA adsorption from solution.

Interfacial forces act to extend the combed DNA molecules. It is related to the surface tension of the aqueous buffer, where $F = \gamma\pi D$. γ is the surface tension of water, and D is the diameter of double-stranded DNA (2.2 nm). The force at the interfaces is calculated to be 440 pN, which is two orders of magnitude larger than entropic forces that cause DNA in solution to remain in a random coil[15, 16]. DNA begins to lose its B-form helix at forces of 60-70 pN. Additionally, the breaking force of a covalent bond is approximately 1nN, therefore, DNA is expected to stretch, not break during combing. Lambda phage DNA (48,490 bp) has a contour length of 16.1 μm, but has exhibited extension to 21.5 μm, while we have observed lambda DNA as long as 31 μm. This is consistent with our and others' experiments, where DNA is observed to stretch 1.5-2.1 times its contour length[14, 17-19].

5.2.2 DNA/liquid crystal cells

Hybrid liquid crystal cells were assembled with surfaces consisting of OTS and GPTMS SAMs. Physical spacers were not used. Interference colors from the Michel-Levy diagram indicated thickness of 5-10 μm. The OTS layer is known to induce homeotropic anchoring. Previous work using cast films of polymerized GPTMS [20] found planar anchoring; we observed the same with GPTMS SAMs. Cells were filled with 4-*n*-pentyl-4'-cyanobiphenyl (5CB) or n-(4-methoxybenzylidene)-4-butylaniline (MBBA) using capillary action, and heated above the isotropic point to eliminate shear alignment before slow cooling to room temperature for measurements in the nematic phase.

5.2.3 Vapor phase GPTMS SAM preparation

Vapor deposition approach was used to minimize background fluorescence for imaging purposes. Self-assembled monolayers (SAMs) of 3-glycidoxypropyltrimethoxysilane (GPTMS) and octadecyltriethoxysilane (OTS) were prepared on fused silica wafers and borosilicate microscope slides using either standard solution-phase deposition[1, 21] or solvent-assisted amine-catalyzed vapor deposition. Either fused silica cover slips or microscope slides were piranha cleaned,[21] followed by UV-ozone exposure for ~60 minutes with a Boekel UV Clean model 1335500. The slides were then exposed to the vapor from a mixture of toluene, GPTMS, and n-butylamine in a 60:3:1 volume ratio for 17-24 hours at room temperature. Deposition occurs at atmospheric pressure, but slightly improved results occur when a vacuum is pulled momentarily before sealing the reaction chamber (vacuum desiccators). This is presumably due to evacuation of extraneous water from the reaction. SAM quality was

determined using contact angle goniometry. A contact angle of ~65˚ indicated a GPTMS monolayer.

5.2.4 Liquid phase GPTMS SAM preparation

GPTMS SAMs were prepared similarly to OTS SAMs, as described in section 5.1.1. 3-glycidoxypropyltrimethoxysilane (GPTMS) was used in place of alkyl silanes. GPTMS was obtained from both Gelest and Fisher at 97% purity. No difference was observed related to supplier. An additional final rinse of isopropanol before vacuum storage removes residual GPTMS, as it is only marginally soluble in toluene. Slides are stored under vacuum until use.

5.2.5 Quartz wedge compensator

LC orientation was confirmed with a quartz wedge compensator. This is accomplished by comparing birefringence colors before and after compensation. First, the sample is turned 45˚ from the crossed polarizers in order to obtain maximum intensity. If birefringence increases, the fast axis on the compensator is aligned with the fast axis on the liquid crystal. If birefringence decreases, the fast axis on the compensator is aligned with the slow axis on the liquid crystal.

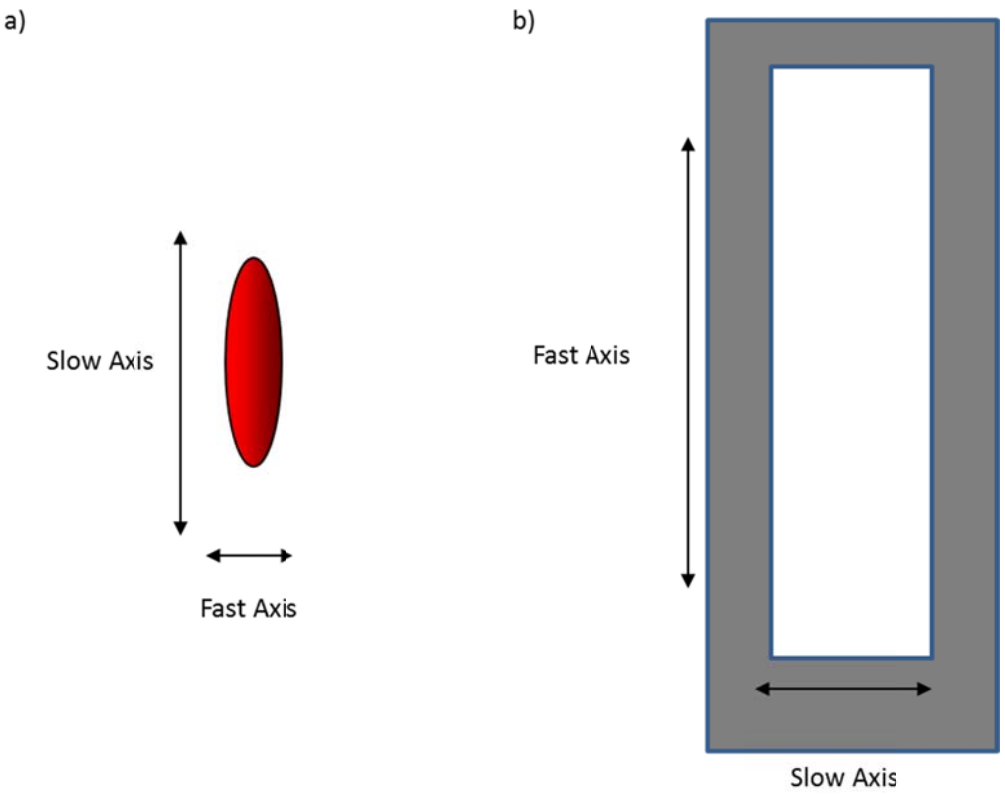

Figure 5.4: Schematic description of quartz wedge compensator use. a) Fast and slow axis of a calamatic liquid crystal with positive birefringence (the case for both MBBA and 5CB). b) Fast and slow axis of a quartz wedge compensator.

5.2.6 Fluorescent microscopy

Fluorescently-labeled dsDNA was visualized using epifluorescence on a Nikon Ti-E inverted microscope with a 60x objective. The microscope was capable of both fluorescence and polarized light modes, allowing direct observation of the effect of extended DNA molecules on the local LC orientation. YOYO-labeled DNA was captured using a standard fluorescein set of emission filters. 10x images were obtained using and Olympus BH2-UMA microscope modified for transmission mode incorporating crossed polarizers. The extinction direction of LC was determined by recording the average light intensity through crossed polarizers as the sample was rotated with respect to the polarizer direction, and fitting the data to a sinusoidal function.

5.3 Lyotropic Self-Assembly of line-active compounds in two dimensions

5.3.1 Langmuir trough

Monolayers are formed in a dual-barrier Nima Technologies Langmuir-Blodgett trough. Monolayers were formed by dropwise addition of perfluoroundecanoic acid (F10) (Oakwood Products, Inc) solutions of 0.5g/L in chloroform (Fisher) and F8H11 (synthesis previously described, see Figure 4.8)[22] solutions ranging from 0.1 to 1.0 g/L in tetrahydrofuran (THF, Fisher). Prior to filling, the trough is repeatedly cleaned with isopropanol and chloroform. The subphase consisted of Millipore water (18.2MΩ) adjusted to pH 3 with HCl (Malinckrodt). After spreading, monolayers were left for 15 minutes to allow for solvent evaporation. Surface pressure was maintained at a constant 4.3 mN/m during transfer with a barrier speed of 20 mm/min. Langmuir-

Blodgett films were transferred onto freshly cleaved mica. Mica was freshly cleaved using scotch tape to achieve an atomically flat surface. Surface pressure was monitored using paper Wilhelmy plates. Dipping occurred at 10 mm/min on the upstroke.

5.3.2 Particle analysis

The distinctive features (representing 2D micelles) on the AFM images were counted using ImageJ for mole fractions of 0.63 or less and with Mathematica for concentrations greater than 0.63. Error bars represent standard error for at least eight distinct images. For samples at very high F8H11 mole fraction (≥0.95), where features were close-packed, the lateral sizes were determined by measuring the peak-to-peak distance from image cross-sections. For lower concentrations, where features were isolated, the lateral size of features was determined by measuring the width of a feature before the height profile returned to baseline of many individual features from AFM image cross-sections. AFM images that exhibited periodic structures were further analyzed by performing Fourier transforms (FT) using Image SXM software. Angular averages were performed of these “powder pattern” FTs, and a linear background was subtracted.

5.3.3 AFM

Samples were imaged with a Nanoscope III (Digital Instruments, now Bruker) multi-mode AFM. Images were obtained using tapping mode under ambient conditions, using silicon tips with a nominal spring constant of 40 N/m and a nominal tip radius of

10 nm. Images were taken in tapping mode using height contrast at room temperature (23 ± 1 ˚C).

5.3.4. Fourier analysis

Fourier transforms were executed using Image SXM software. The images were radially averaged, and a linear background was subtracted out to obtain a peak. For pure F8H11 monolayer where distinct spots were observed, line averages were used rather than radial averages. The position, Q_0, and half-width at half max (HWHM) was determined by a Gaussian fit from the resulting peaks; the row spacing was calculated as $2\pi/Q_0$ and the correlation length as 1/HWHM.

5.4 Liquid crystal anchoring transitions induced by phase transitions of photisomerizable surfactant at the nematic/aqueous interface (Appendix A)

5.4.1 Sample Preparation

Borosilicate glass slides were cleaned with a fresh piranha solution composed of 30% aqueous H_2O_2 and concentrated H_2SO_4 (1:3 v/v) for 1 h at 70 ˚C. (Warning: piranha solution reacts strongly with organic compounds and should be handled with extreme caution; do not store solution in closed containers.) An octadecyltriethoxysilane (OTS) (Gelest, Inc.) self-assembled monolayer (SAM) was deposited on the glass following the procedure described by Walba et al.[23] Briefly, clean glass slides were rinsed with acetone and toluene and submerged in a solution of toluene, OTS, and butylamine (200:3:1 v/v) for 30 min at 60 ˚C. Following this deposition, the glass slides were rinsed with toluene, dried with a stream of nitrogen, and stored under a vacuum at room temperature for 24 h prior to use. This produced a surface with a water contact

angle ~95˚ as measured optically by the sessile drop method with a goniometer; sufficient to induce homeotropic alignment of the liquid crystal. The slides were cut into small rectangles measuring approximately 0.75 X 0.50 in.

The liquid crystal material used for microscopy experiments was E7 ($n_{\perp}$=1.57, $n_{||}$=1.73, Merck Ltd.), a four-component liquid crystal mixture of cyanobiphenyls and a cyanoterphenyl with a nematic to isotropic (N-I) transition temperature of 60 ˚C. For spectroscopy experiments, the liquid crystal 5CB (4-n-pentyl-4'-cyanobiphenyl, Alfa Aesar) was used because of its lower nematic-isotropic transition temperature (35.5 ˚C). The fatty acid derivative (4-(8-alkyl)-4'-(carboxy-(3-alkyl)-oxy)azobenzene (8Az3, see Figure A.1) was custom-synthesized[24]. 8Az3 dissolved in chloroform was added to the liquid crystal material, briefly mixed with a glass pipette, then dried under a stream of nitrogen. Chloroform disrupts the liquid crystalline order of the fluid, and is fully removed when the liquid changes from clear to cloudy. This deposition strategy was chosen because of the extremely low solubility of 8Az3 in the aqueous phase. The final concentrations of 8Az3 in the liquid crystal were 8.22 mM, 12.33 mM, 16.44 mM, and 20.55 mM. Following a protocol first reported by Brake and Abbott [25], the liquid crystal was drawn into a 25 μm capillary tube and used to fill a TEM grid via capillary action by contacting the capillary tube to a TEM grid laying flat on a rectangle of SAM-coated glass. The TEM grid (SPI Supplies) used was a gold-coated copper, square mesh grid with hole sizes of 205 μm. Following the introduction of the liquid crystal into the grid the liquid crystal was heated above its N-I transition temperature and slowly cooled back to room temperature. This resulted in a liquid crystal layer of approximately 20 μm in thickness.

Chamber slides (Lab-Tek) were filled with ultrapure water (resistivity of 18.2 MΩ-cm) and heated to 55 ˚C. Liquid crystal -filled TEM grids on SAM-coated glass were submerged in the water for 60 minutes, sufficient time for an 8Az3 monolayer at the liquid crystal/aqueous interface to reach a steady-state surface coverage. The solution was held constant at 55 ˚C throughout the formation of the monolayer. A cover was placed on the chamber to limit evaporation.

In Langmuir-Blodgett experiments, clean glass slides (measuring approximately 10 x 20 mm) were used to transfer 8Az3 Langmuir monolayers using a KSV Minitrough at constant temperature and surface pressure. The dipping speed was 2 mm/min. Liquid crystal cells (E7) were assembled by securing one LB-coated plate with a larger plate (approximately 20x30 mm) treated for homeotropic anchoring, with pieces of 13 μm-thick mylar (Goodfellow) setting the cell spacing, and were subsequently filled by capillarity. For proper visualization of the azimuthal inhomogeneities in the sample, the anchoring strength of the liquid crystal at the homeotropic plate must not be much stronger than at the 8Az3-coated plate. Homeotropic anchoring with an appropriate strength was obtained by transferring a stearic acid Langmuir monolayer in a hexatic phase onto a ITO-coated glass plate, following a procedure described by Fazio et al.[26]

5.4.2 Polarized light microscopy

The liquid crystal orientation and textures were observed using plane-polarized light with an Olympus BH2-UMA microscope modified for transmission mode incorporating crossed polarizers. The chamber slide containing the liquid crystal setup was placed on a rotating stage with an attached custom heating and cooling stage. The

stage was located between the polarizers. All images were captured using a Lumenera Infinity 1-C digital video camera mounted on the microscope and positioned so its x and y axes were aligned with those of the polarizer and analyzer. Homeotropic orientation was determined by the absence of transmitted light during a full 360˚ rotation of the sample. In the absence of homeotropic orientation, zenithal tilt angle at the nematic/water interface was determined by comparing the observed colors to those on a Michel-Levy chart (Figure 1.9). This yielded the birefringence, from which we were then able to determine $\theta_{n/w}$, the zenithal angle of the liquid crystal director at the nematic/water interface, from the following equation [27]:

$$\Delta n_e = \frac{1}{\theta_{n/w} - \theta_{n/SAM}} \int_{\theta_{n/SAM}}^{\theta_{n/w}} \frac{n_{\parallel} n_{\perp} \, d\theta}{\sqrt{n_{\parallel}^2 \cos^2\theta + n_{\perp}^2 \sin^2\theta}} - n_{\perp}$$

where Δn_e is the effective average birefringence, $n_{\parallel}$ is the index of refraction for E7 parallel to the optical axis, and $n_{\perp}$ is the index of refraction for E7 perpendicular to the optical axis. $\theta_{n/SAM}$ is the zenithal angle of the liquid crystal director at the nematic/SAM interface and was assumed to always have a value of 0 (homeotropic anchoring). The azimuthal angle was determined by rotating the sample to extinction.

Observation of the liquid crystal cells containing the LB aligning plate was performed in a Nikon E400Pol optical microscope between crossed polarizers. Images were acquired with an Olympus E400 digital camera. Langmuir monolayers were observed by a custom-made Brewster angle microscope [28] prior to their transfer onto glass plates.

5.4.3 UV/Vis excitation

Samples were irradiated with UV or visible light isolated from spectral lines of a mercury-arc lamp (power = 100 W). Wavelengths were isolated using bandpass filters (Chroma Tech.) with maximum transmissions at 365 nm, 405 nm, and 436 nm and full width half max ranges of 10 nm, 10 nm, and 20 nm respectively. Power density was moderated using 0.5 and 0.2 neutral density filters. The irradiation was incident from the aqueous side of the sample onto the interface. In order to examine the behavior of 8Az3 in the *trans* state, the liquid crystal /8Az3 mixture was kept in the dark for at least 24 hrs prior to use. By thermal relaxation, the *cis* isomer of 8Az3 isomerized to the *trans* state in the absence of any light. Immediately upon immersion of the liquid crystal-filled grid in ultrapure water the liquid crystal appeared highly birefringent as is usual for a liquid crystal aqueous interface in the absence of an adsorbed monolayer. The sample was kept immersed in the dark for at least 60 minutes, allowing a monolayer to form at the interface.

Langmuir monolayer experiments were performed following a similar protocol. For all-*trans* monolayers, the ~1 mM chloroform spreading solution was prepared under dim red light and stored in the dark for 24h prior to spreading the monolayer. LB transfer was also performed in the dark. Subsequent handling of the LB films did not affect the textures observed in the liquid crystal cells, i.e., there was no need to handle the plates in the dark. To prepare monolayers with a maximum presence of cis isomer, the system was continuously irradiated with a 365 nm UV lamp. An intermediate composition was achieved by working under room light photostationary conditions. In previous work [24], we found that this state corresponded to approximately 40% *cis* isomer.

5.4.4. UV/Vis Spectroscopy

Samples consisting of 50 μM 8Az3 in 5CB were contained in 1 cm square 4-window quartz cuvettes and heated into the isotropic phase (~37 ˚C). Throughout the experiments, the samples were held at this temperature and stirred vigorous using a cylindrical magnetic stirrer designed for use in cuvettes. UV/Vis spectra were measured using a fiber optic coupled probe beam involving Ocean Optics equipment (LS-1 tungsten-halogen source, S2000 multichannel spectrometer) using pure 5CB as the reference. To minimize disturbance of the isomer distribution, light from the tungsten-halogen lamp was blocked until immediately before a measurement. A spectral acquisition was initiated within 2s of the onset of illumination by the probe beam, and completed with a 3s exposure, after which the probe beam was again blocked. The spectrum of the nearly all *trans* state was obtained by permitting the sample to relax thermally in total darkness overnight prior to the measurement. In order to obtain spectra associated with various photostationary states, the cuvette was continuously pumped with an intense beam incident along a direction perpendicular to the probe beam. The pump beam originated with an Osram HBO 100W compact arc Hg lamp operating under current control. The wavelength range was restricted to individual Hg emission lines by bandpass filters centered at 365 nm, 405 nm, and 436 nm. In each case the sample was pumped for several minutes in order to ensure that a photostationary state had been reached (experiments suggested that this occurred within a minute or so), and then a spectrum was captured. Thermal relaxation kinetics experiments were performed by first establishing a photostationary state with the 365nm pump beam. At t = 0s the pump beam was blocked. The sample was then allowed to

relax in the dark. UV/Vis spectra were acquired at approximately 30min intervals, using the minimal irradiation protocol, i.e. the spectrometer beam was blocked except for the 3s required to acquire one spectrum each 30 minutes.

5.5 Future Work (Appendix B)

5.5.1 GPTMS Vapor Phase SAMs

GPTMS SAMs vapor phase SAMs were created as described in section 5.2.3 on fused silica.

5.5.2 DNA oligonucleotide sequences

Oligonucleotide sequences are as follows, from 5' to 3' end. These sequences were chosen for low self-complementarity. Sequences were ordered from Eurofins Operon.

Table 5.1: DNA oligonucleotide sequences used for attachment/hybridization studies

Name	Sequence	5' modifier	3' modifier
A16	AGA AAA AAC TTC GTG C		
A16comp	GCA CGA AGT TTT TTC T		
A32	AGA AAA AAC TTC GTG CCC TTC ATC CCC TAA TA		
A32complement	TAT TAG GGG ATG AAG GGC ACG AAG TTT TTT CT		
A32mismatch	CGT GTC CTC CCC CCA GAA GCA CCA AAA GCC CG		
Amine_32_488	AGA AAA AAC TTC GTG CCC TTC ATC CCC TAA TA	Amino C6 Linker	6-Fam (Fluorescein)
A_32Comp_647	TAT TAG GGG ATG AAG GGC ACG AAG TTT TTT CT	AminoC6+Alexa647	

5.5.2 Epoxide-Amine coupling

Epoxide-amine coupling was attempted in order to reliably end-couple DNA oligonucleotides. It is well known that under basic conditions (generally above pH 9), that and amine group will act as a nucleophile for a strained epoxide group, thus covalently binding to a substrate. Unfortunately, it has also been shown that epoxide rings are under an extreme amount of strain, and that under basic conditions, water itself can act as a nucleophile, effectively outcompeting an amine-terminated molecules, and likely resulting in the inconsistencies of the epoxide/amine oligonucleotide coupling[29-32]. This can account for the inconsistencies in attaching amine-terminated oligonucleotides to a GPTMS SAM.

5.5.3 Streptavidin-Biotin coupling

Streptavidin-Biotin coupling was attempted as an alternative to epoxide/amine coupling of oligonucleotides. It is among the strongest non-covalent interactions known, and is stable as long as the proteins are not denature (below 70 degrees)[30]. Coupling was attempted in water, PBS, 1x SSC (sodium saline citrate), 6x SSC at room temperature. Streptavidin coated class was obtained from Xenopore (VPX 000).

Name	Sequence	5' modifier	3' modifier
Biotin_A32_488	AGA AAA AAC TTC GTG CCC TTC ATC CCC TAA TA	Bio-Teg	6-Fam (Fluorescein)
A_32Comp_647	TAT TAG GGG ATG AAG GGC ACG AAG TTT TTT CT	AminoC6+Alexa647	

Table 5.2: DNA oligonucleotide sequences used for streptavidin/biotin attachment/hybridization studies

5.5.4 Measurement of attachment

Attachment was measured on a Nikon Ti-E inverted microscope with a 10X objective. Overall intensity was captured from individual images, with illuminating conditions optimized, then held constant. Background was subtracted from images with no added fluorescent activity. Background noise was determined to be approximately $\pm$500 counts.

5.5.5 Oligonucleotide hybridization

Hybridization buffers included 1 M NaCl, 1x SSC, 6x SSC, PBS (pH 7.4), potassium phosphate dibasic (pH 8), and Millipore water. Commercial hybridization solutions (Unihyb, Hybit from Arrayit) were also attempted. Hybridization temperatures were kept at 5-10 ºC below $T_{m.}$ Hybridization was indistinguishable from nonspecific adsorption, including after rinsing.

5.5.6 Agarose Gel Electrophoresis

Agarose gel electrophoresis was performed to determine fragment size of shortened lambda DNA fragments. Gels were 1% agarose in TAE buffer (0.5 g agarose, 50 mL TAE, 2.5 μL ethidium bromide). Ethidium bromide was used to visualize DNA under UV illumination. Gels were run at 120 V, for 30 minutes or longer, based on the expected length of DNA fragments in order to obtain good separation. Gels were run with approximately 10 ng of DNA per well to avoid smearing of the DNA bands from overloaded gels. DNA was loaded with 2 μL of “blue juice”, (0.25% bromophenol blue 40% w/v sucrose) [33], designed to add density the DNA solution to cause it to sink in the agarose wells, as well as a dye to give a visual aid as to how far the DNA bands had progressed under the electric field.

5.5.7 ssDNA labeling

DNA was labeled according to the Ulysis protocol. The denaturation step was skipped in order to decrease labeling efficiency. Separation was attempted with both Bio-Rad Micro Bio Spin P-30 columns, as well as Princeton Separations Centri-Sep columns. Silica based systems such as Qiagen products are to be avoided, as they bind to the fluorescent dye. Separations proved problematic for the labeled DNA. Excessive fluorescent dye causes binding to the resin of either type of acceptable separation column. Increasing the amount of DNA in the protocol without adjusting any other parameters leads to a decrease in labeling, which is ideal for separations, as the kit suggests avoiding lengths over 1000 bp to avoid aggregation. A linear relationship between initial mass of DNS and labeling efficiency was found when adding up to 6 μg of DNA. Additionally, the columns do not pass DNA over 1000 base pairs efficiently.

5.6 References

1. Walba, D. M.; Liberko, C. A.; Korblova, E.; Farrow, M.; Furtak, T. E.; Chow, B. C.; Schwartz, D. K.; Freeman, A. S.; Douglas, K.; Williams, S. D.; Klittnick, A. F.; Clark, N. A., Self-assembled monolayers for liquid crystal alignment: simple preparation on glass using alkyltrialkoxysilanes. *Liquid Crystals* **2004,** 31, (4), 481 - 489.

2. Ye, T.; McArthur, E. A.; Borguet, E., Mechanism of UV Photoreactivity of Alkylsiloxane Self-Assembled Monolayers. *The Journal of Physical Chemistry B* **2005,** 109, (20), 9927-9938.

3. Ye, T.; Wynn, D.; Dudek, R.; Borguet, E., Photoreactivity of Alkylsiloxane Self-Assembled Monolayers on Silicon Oxide Surfaces. *Langmuir* **2001,** 17, (15), 4497-4500.

4. Hong, L.; Sugimura, H.; Furukawa, T.; Takai, O., Photoreactivity of alkylsilane self-assembled monolayers on silicon surfaces and its application to preparing micropatterned ternary monolayers. *Langmuir* **2003,** 19, (6), 1966-1969.

5. Uyama, Y.; Inoue, H.; Ito, K.; Kishida, A.; Ikada, Y., Comparison of Different Methods for Contact-Angle Measurement *Journal of Colloid and Interface Science* **1991,** 141, (1), 275-279.

6. Manifacier, J. C.; Gasiot, J.; Fillard, J. P., Simple Method for Determination of Optical Constants n,k, and Thickness of a Weakly Absorbing Thin Film *Journal of Physics E-Scientific Instruments* **1976,** 9, (11), 1002-1004.

7. Huibers, P. D. T.; Shah, D. O., Multispectral determination of soap film thickness. *Langmuir* **1997,** 13, (22), 5995-5998.

8. Van Doorn, C. Z.; Gerritsma, C. J.; deKlerk, J. J. M. J., *Influence of the Device Parameters on the Performance of Twisted-Nematic Liquid Crystal Matrix Displays*. Plenium Press: New York, 1980.

9. Dunmar, D.; Fukuda, A.; Luckhurst, G., *Physical Properties of Liquid Crystals: Nematics*. INSPEC, The Institution of Electrical Engineers: London, 2001.

10. Uyama, Y.; Inoue, H.; Ito, K.; Kishida, A.; Ikada, Y., Comparison of different methods for contact angle measurement. *Journal of Colloid and Interface Science* **1991,** 141, (1), 275-279.

11. Israelachvili, J. N., *Intermolecular And Surface Forces*. Academic Press: 1991.

12. Safran, S. A., *Statistical Thermodynamics of Surfaces, Interfaces, and Membranes*. Addison-Wesley Publishing Company: Reading, Massachusetts, 1994; Vol. 90.

13. Bensimon, A.; Simon, A.; Chiffaudel, A.; Croquette, V.; Heslot, F.; Bensimon, D., Alignment and sensitive detection of DNA by a moving interface. *Science* **1994,** 265, (5181), 2096-2098.

14. Bensimon, D.; Simon, A. J.; Croquette, V.; Bensimon, A., Stretching DNA with a Receding Meniscus- Experiments and Models. *Physical Review Letters* **1995,** 74, (23), 4754-4757.

15. Smith, S.; Finzi, L.; Bustamante, C., Direct mechanical measurements of the elasticity of single DNA molecules by using magnetic beads. *Science* **1992,** 258, (5085), 1122-1126.

16. Bustamante, C.; Marko, J.; Siggia, E.; Smith, S., Entropic elasticity of lambda-phage DNA. *Science* **1994,** 265, (5178), 1599-1600.

17. Clausen-Schaumann, H.; Rief, M.; Tolksdorf, C.; Gaub, H. E., Mechanical stability of single DNA molecules. *Biophysical Journal* **2000,** 78, (4), 1997-2007.

18. Punkkinen, O.; Hansen, P. L.; Miao, L.; Vattulainen, I., DNA Overstretching Transition: Ionic Strength Effects. *Biophysical Journal* **2005,** 89, (2), 967-978.

19. Cluzel, P.; Lebrun, A.; Heller, C.; Lavery, R.; Viovy, J. L.; Chatenay, D.; Caron, F., DNA: An extensible molecule. *Science* **1996,** 271, (5250), 792-794.

20. Dozov, I.; Stoenescu, D. N.; Lamarque-Forget, S.; Martinot-Lagarde, P.; Polossat, E., Planar degenerated anchoring of liquid crystals obtained by surface memory passivation. *Applied Physics Letters* **2000,** 77, (25), 4124-4126.

21. Malone, S. M.; Schwartz, D. K., Polar and Azimuthal Alignment of a Nematic Liquid Crystal by Alkylsilane Self-Assembled Monolayers: Effects of Chain-Length and Mechanical Rubbing

doi:10.1021/la801322x. *Langmuir* **2008,** 24, (17), 9790-9794.

22. Trabelsi, S.; Zhang, S.; Lee, T. R.; Schwartz, D. K., Swelling of a cluster phase in Langmuir monolayers containing semi-fluorinated phosphonic acids. *Soft Matter* **2007,** 3, (12), 1518-1524.

23. Walba, D. M.; Liberko, C. A.; Korblova, E.; Farrow, M.; Furtak, T. E.; Chow, B. C.; Schwartz, D. K.; Freeman, A. S.; Douglas, K.; Williams, S. D.; Klittnick, A. F.; Clark, N. A., Self-assembled monolayers for liquid crystal alignment: simple preparation on glass using alkyltrialkoxysilanes. *Liquid Crystals* **2004,** 31, (4), 481-489.

24. Crusats, J.; Albalat, R.; Claret, J.; Ignes-Mullol, J.; Sagues, F., Influence of temperature and composition on the mesoscopic textures of azobenzene Langmuir monolayers. *Langmuir* **2004,** 20, (20), 8668-8674.

25. Brake, J. M.; Abbott, N. L., An experimental system for imaging the reversible adsorption of amphiphiles at aqueous-liquid crystal interfaces. *Langmuir* **2002,** 18, (16), 6101-6109.

26. Fazio, V. S. U.; Nannelli, F.; Komitov, L., Sensitive methods for estimating the anchoring strength of nematic liquid crystals on Langmuir-Blodgett monolayers of fatty acids. *Physical Review E* **2001,** 63, (6).

27. Price, A. D.; Schwartz, D. K., Anchoring of a nematic liquid crystal on a wettability gradient. *Langmuir* **2006,** 22, (23), 9753-9759.

28. Ignes-Mullol, J.; Claret, J.; Sagues, F., Star defects, boojums, and cardioid droplet shapes in condensed dimyristoylphosphatidylethanolamine monolayers. *Journal of Physical Chemistry B* **2004,** 108, (2), 612-619.

29. Cloarec, J. P.; Deligianis, N.; Martin, J. R.; Lawrence, I.; Souteyrand, E.; Polychronakos, C.; Lawrence, M. F., Immobilization of homooligonucleotide probe layers onto Si/SiO2 substrates: characterization by electrochemical impedance measurements and radiolabelling. *Biosensors & Bioelectronics* **2002,** 17, (5), 405-412.

30. Hermanson, G. T., *Bioconjugate Techniques*. 2 ed.; Elsiver Academic Press: Amsterdam, Boston, 2008.

31. Lindroos, K.; Liljedahl, U.; Raitio, M.; Syvanen, A.-C., Minisequencing on oligonucleotide microarrays: comparison of immobilisation chemistries. *Nucl. Acids Res.* **2001,** 29, (13), e69-.

32. Lamture, J. B.; LBeattie, K.; Burke, B. E.; Eggers, M. D.; Ehrlich, D. J.; Fowler, R.; Hollis, M. A.; Kosicki, B. B.; Reich, R. K.; Smith, S. R.; Varma, R. S.; Hogan, M. E., Direct detection of nucleic acid hybridization on the surface of a charge coupled device. *Nucleic Acids Res.* **1994,** 22, (11), 2121-2125.

33. Sambrook, J., *Molecular Cloning: A laboratory Manual*. 3 ed.; Cold Spring Harbor Laboratory Press: 2001; Vol. 1.

Bibliography

1. Affymatrix, Microarray Products. 2011.

2. Affymatrix, Product Pricing. 2011.

3. Agilent http://www.genomics.agilent.com/CollectionSubpage.aspx?PageType=Product&SubPageType=ProductDetail&PageID=359. (07-06-2011),

4. Aglient http://www.chem.agilent.com/Library/datasheets/Public/5990-6404en_lo.pdf. http://www.chem.agilent.com/Library/datasheets/Public/5990-6404en_lo.pdf (8/19/2011),

5. Akerman, B.; Tuite, E., Single- and double-strand photocleavage of DNA by YO, YOYO and TOTO. Nucl. Acids Res. 1996, 24, (6), 1080-1090.

6. Alexe-Ionescu, A. L.; Barbero, G.; Ignatov, A.; Miraldi, E., Surface transitions in nematic liquid crystals oriented with Langmuir-Blodgett films. Applied Physics A: Materials Science & Processing 1993, 56, (5), 453-455.

7. Alkhairalla, B.; Allinson, H.; Boden, N.; Evans, S. D.; Henderson, J. R., Anchoring and orientational wetting of nematic liquid crystals on self-assembled monolayer substrates: An evanescent wave ellipsometric study. Physical Review E 1999, 59, (3), 3033-3039.

8. Anderson, M. L. M., Nucleic Acid Hybridization. Springer: New York, 1999.

9. Aoki, P. H. B.; Volpati, D.; Riul, A.; Caetano, W.; Constantino, C. J. L., Layer-by-Layer Technique as a New Approach to Produce Nanostructured Films Containing Phospholipids as Transducers in Sensing Applications. Langmuir 2009, 25, (4), 2331-2338.

10. Aronzon, D.; Levy, E. P.; Collings, P. J.; Chanishvili, A.; Chilaya, G.; Petriashvili, G., rans-cis isomerization on an azoxybenzene liquid crystal. Liquid Crystals 2007, 34, 707-718.

11. Asano, T.; Okada, T., Thermal Z-E Isomerization of Azobenzenes. The Pressure, Solvent, and Substituent Effects. Journal of Organic Chemistry 1984, 49, 4387-4391.

12. Bai, Y.; Abbott, N. L., Recent Advances in Colloidal and Interfacial Phenomena Involving Liquid Crystals. Langmuir 2011, 27, (10), 5719-5738.

13. Bain, C. D.; Whitesides, G. M., Depth sensitivity of wetting: monolayers of .omega.-mercapto ethers on gold. J. Am. Chem. Soc. 1988, 110, (17), 5897-5898.

14. Ban, B. S.; Kim, Y. B., Materials and Rubbing Dependence on Azimuthal Anchoring Energy of Rubbed Polyimide Surfaces. J. Phys. Chem. B 1999, 103, (19), 3869-3871.

15. Barton, S. W.; Goudot, A.; Bouloussa, O.; Rondelez, F.; Lin, B. H.; Novak, F.; Acero, A.; Rice, S. A., Structural Transitions in a Monolayer of Fluorinated Amphiphile Molecules Journal of Chemical Physics 1992, 96, (2), 1343-1351.

16. Beattie, K.; Beattie, W.; Meng, L.; Turner, S.; Coral-Vazquez, R.; Smith, D.; McIntyre, P.; Dao, D., Advances in genosensor research. Clin Chem 1995, 41, (5), 700-706.

17. Beattie, W.; Meng, L.; Turner, S.; Varma, R.; Dao, D.; Beattie, K., Hybridization of DNA targets to glass-tethered oligonucleotide probes. Molecular Biotechnology 1995, 4, (3), 213-225.

18. Behdani, M.; Keshmiri, S. H.; Soria, S.; Bader, M. A.; Ihlemann, J.; Marowsky, G.; Rasing, T., Alignment of liquid crystals with periodic submicron structures ablated in polymeric and indium tin oxide surfaces. Appl. Phys. Lett. 2003, 82, (16), 2553-2555.

19. Behdani, M.; Rastegar, A.; Keshmiri, S. H.; Missat, S. I.; Vlieg, E.; Rasing, T., Submicron liquid crystal pixels on a nanopatterned indium tin oxide surface. Appl. Phys. Lett. 2002, 80, (24), 4635-4637.

20. Bensimon, A.; Simon, A.; Chiffaudel, A.; Croquette, V.; Heslot, F.; Bensimon, D., Alignment and sensitive detection of DNA by a moving interface. Science 1994, 265, (5181), 2096-2098.

21. Bensimon, D.; Simon, A. J.; Croquette, V.; Bensimon, A., Stretching DNA with a Receding Meniscus- Experiments and Models. Physical Review Letters 1995, 74, (23), 4754-4757.

22. Benvegnu, D. J.; McConnell, H. M., Line Tension Between Liquid Domains in Lipid Monolayers. Journal of Physical Chemistry 1992, 96, (16), 6820-6824.

23. Berreman, D. W., Solid Surface Shape and the Alignment of an Adjacent Nematic Liquid Crystal. Physical Review Letters 1972, 28, (26), 1686-1686.

24. Bi, X.; Huang, S.; Hartono, D.; Yang, K.-L., Liquid-crystal based optical sensors for simultaneous detection of multiple glycine oligomers with micromolar concentrations. Sensors and Actuators B: Chemical 2007, 127, (2), 406-413.

25. Blanchette, C. D.; Lin, W. C.; Orme, C. A.; Ratto, T. V.; Longo, M. L., Domain nucleation rates and interfacial line tensions in supported bilayers of ternary mixtures containing galactosylceramide. Biophysical Journal 2008, 94, (7), 2691-2697.

26. Blinov, L. M.; Cigrinov, V. G., Electrooptic effects in liquid crystal materials. Springer: New York [etc.], 1996.

27. Blodgett, K. B., Films built by depositing successive monomolecular layers on a solid surface. Journal of the American Chemical Society 1935, 57, (1), 1007-1022.

28. Bloomfield, V. A.; Crothers, D. M.; Ignacio Itnoco, J., Nucleic Acids: Structure, Properties, and Functions. University Science Books: Sausalito, CA, 2000.

29. Bloss, D. F., An Introduction to the Methods of Optical Crystallography. Holt, Rinehart and Winston: New York, Chicago, San Francisco, Toronto, London, 1961.

30. Bradshaw, M. J.; Raynes, E. P.; Bunning, J. D.; Faber, T. E., THE FRANK CONSTANTS OF SOME NEMATIC LIQUID-CRYSTALS. Journal De Physique 1985, 46, (9), 1513-1520.

31. Brake, J. M.; Abbott, N. L., An experimental system for imaging the reversible adsorption of amphiphiles at aqueous-liquid crystal interfaces. Langmuir 2002, 18, (16), 6101-6109.

32. Brake, J. M.; Abbott, N. L., Coupling of the orientations of thermotropic liquid crystals to protein binding events at lipid-decorated interfaces. Langmuir 2007, 23, (16), 8497-8507.

33. Brake, J. M.; Daschner, M. K.; Abbott, N. L., Formation and Characterization of Phospholipid Monolayers Spontaneously Assembled at Interfaces between Aqueous Phases and Thermotropic Liquid Crystals. Langmuir 2005, 21, (6), 2218-2228.

34. Brake, J. M.; Daschner, M. K.; Luk, Y.-Y.; Abbott, N. L., Biomolecular Interactions at Phospholipid-Decorated Surfaces of Liquid Crystals. Science 2003, 302, (5653), 2094-2097.

35. Brake, J. M.; Mezera, A. D.; Abbott, N. L., Active Control of the Anchoring of 4'-Pentyl-4-cyanobiphenyl (5CB) at an Aqueous-Liquid Crystal Interface By Using a Redox-Active Ferrocenyl Surfactant. Langmuir 2003, 19, (21), 8629-8637.

36. Brewster, R.; Pincus, P. A.; Safran, S. A., Hybrid Lipids as a Biological Surface-Active Component. Biophysical Journal 2009, 97, (4), 1087-1094.

37. Bryan-Brown, G. P.; Wood, E. L.; Sage, I. C., Weak surface anchoring of liquid crystals. Nature 1999, 399, (6734), 338-340.

38. Bustamante, C.; Marko, J.; Siggia, E.; Smith, S., Entropic elasticity of lambda-phage DNA. *Science* 1994, 265, (5178), 1599-1600.

39. Bustamante, C.; Vesenka, J.; Tang, C. L.; Rees, W.; Guthold, M.; Keller, R., Circular DNA-Molecules Imaged in Air by Scanning Force Mircoscopy Biochemistry 1992, 31, (1), 22-26.

40. Cain, N.; Van Bogaert, J.; Gin, D. L.; Hammond, S. R.; Schwartz, D. K., Self-organization of a wedge-shaped surfactant in monolayers and multilayers. Langmuir 2007, 23, (2), 482-487.

41. Carlsson, C.; Larsson, A.; Jonsson, M.; Albinsson, B.; Norden, B., Optical and Photophysical Properties of the Oxazole Yellow DNA Probes YO and YOYO. Journal of Physical Chemistry 1994, 98, (40), 10313-10321.

42. Caruthers, M. H., GENE SYNTHESIS MACHINES - DNA CHEMISTRY AND ITS USES. Science 1985, 230, (4723), 281-285.

43. Caseli, L.; Perinotto, A. C.; Viitala, T.; Zucolotto, V.; Oliveira, O. N., Immobilization of Alcohol Dehydrogenase in Phospholipid Langmuir-Blodgett Films To Detect Ethanol. Langmuir 2009, 25, (5), 3057-3061.

44. Cassie, A. B. D.; Baxter, S., Wettability of porous surfaces. Transactions of the Faraday Society 1944, 40, 546-551.

45. Charych, D. H.; Nagy, J. O.; Spevak, W.; Bednarski, M. D., Direct Colorimetric Detection of A Receptor-Ligand Interaction by a Polymerized Bilayer Assembly Science 1993, 261, (5121), 585-588.

46. Chaudhari, P.; Lacey, J.; Doyle, J.; Galligan, E.; Lien, S.-C. A.; Callegari, A.; Hougham, G.; Lang, N. D.; Andry, P. S.; John, R.; Yang, K.-H.; Lu, M.; Cai, C.; Speidell, J.; Purushothaman, S.; Ritsko, J.; Samant, M.; Stohr, J.; Nakagawa, Y.; Katoh, Y.; Saitoh, Y.; Sakai, K.; Satoh, H.; Odahara, S.; Nakano, H.; Nakagaki, J.; Shiota, Y., Atomic-beam alignment of inorganic materials for liquid-crystal displays. 2001, 411, (6833), 56-

47. Chen, C. H.; Yang, K. L., Detection and Quantification of DNA Adsorbed on Solid Surfaces by Using Liquid Crystals. Langmuir 2010, 26, (3), 1427-1430.

48. Choi, Y.; Atherton, T.; Ferjani, S.; Petschek, R. G.; Rosenblatt, C., Patterning-induced surface chirality and modulation of director twist in a nematic cell. Physical Review E 2009, 80, (6), 4.

49. Clare, B. H.; Abbott, N. L., Orientations of Nematic Liquid Crystals on Surfaces Presenting Controlled Densities of Peptides: Amplification of Protein-Peptide Binding Events. Langmuir 2005, 21, (14), 6451-6461.

50. Clare, B. H.; Efimenko, K.; Fischer, D. A.; Genzer, J.; Abbott, N. L., Orientations of Liquid Crystals in Contact with Surfaces that Present Continuous Gradients of Chemical Functionality. Chem. Mater. 2006, 18, (9), 2357-2363.

51. Clare, B. H.; Guzman, O.; dePablo, J.; Abbott, N. L., Anchoring Energies of Liquid Crystals Measured on Surfaces Presenting Oligopeptides. Langmuir 2006, 22, (18), 7776-7782.

52. Clark, N. A., Surface memory effects in liquid crystals: Influence of surface composition. Physical Review Letters 1985, 55, (3), 292.

53. Clausen-Schaumann, H.; Rief, M.; Tolksdorf, C.; Gaub, H. E., Mechanical stability of single DNA molecules. *Biophysical Journal* 2000**,** 78, (4), 1997-2007.

54. Cloarec, J. P.; Deligianis, N.; Martin, J. R.; Lawrence, I.; Souteyrand, E.; Polychronakos, C.; Lawrence, M. F., Immobilization of homooligonucleotide probe layers onto Si/SiO2 substrates: characterization by electrochemical impedance measurements and radiolabelling. Biosensors & Bioelectronics 2002, 17, (5), 405-412.

55. Cluzel, P.; Lebrun, A.; Heller, C.; Lavery, R.; Viovy, J. L.; Chatenay, D.; Caron, F., DNA: An extensible molecule. Science 1996, 271, (5250), 792-794.

56. Collings, P. J.; Hird, M., Introduction to Liquid Crystals Chemistry and Physics. Taylor and Francis: Bristol, PA, 1997.

57. Crawford, G. P.; Ondris-Crawford, R. J.; Doane, J. W., Systematic study of orientational wetting and anchoring at a liquid-crystal-surfactant interface. Physical Review E 1996, 53, (4), 3647-3662.

58. Crusats, J.; Albalat, R.; Claret, J.; Ignes-Mullol, J.; Sagues, F., Influence of temperature and composition on the mesoscopic textures of azobenzene Langmuir monolayers. Langmuir 2004, 20, (20), 8668-8674.

59. Debye, P., Light Scattering in Soap Solutions Annals of the New York Academy of Sciences 1949, 51, (4), 575-592.

60. Ding, J. Q.; Doudevski, I.; Warriner, H. E.; Alig, T.; Zasadzinski, J. A., Nanostructure changes in lung surfactant monolayers induced by interactions between palmitoyloleoylphosphatidylglycerol and surfactant protein B. Langmuir 2003, 19, (5), 1539-1550.

61. Discher, B. M.; Maloney, K. M.; Grainger, D. W.; Hall, S. B., Effect of neutral lipids on coexisting phases in monolayers of pulmonary surfactant. Biophys. Chem. 2002, 101, 333-345.

62. Doorn, C. Z. v., Dynamic behavior of twisted nematic liquid-crystal layers in switched fields. J. Appl. Phys. 1975, 46, (9), 3738-3745.

63. Dozov, I.; Stoenescu, D. N.; Lamarque-Forget, S.; Martinot-Lagarde, P.; Polossat, E., Planar degenerated anchoring of liquid crystals obtained by surface memory passivation. Appl. Phys. Lett. 2000, 77, (25), 4124-4126.

64. Drawhorn, R. A.; Abbott, N. L., Anchoring of Nematic Liquid-Crystals on Self-Assembled Monolayers Formed from Alkanethiols on Semitransparent Films of Gold. Journal of Physical Chemistry 1995, 99, (45), 16511-16515.

65. Ducker, W. A.; Wanless, E. J., Surface-aggregate shape transformation. Langmuir 1996, 12, (24), 5915-5920.

66. Dunmar, D.; Fukuda, A.; Luckhurst, G., Physical Properties of Liquid Crystals: Nematics. INSPEC, The Institution of Electrical Engineers: London, 2001.

67. Durbin, M. K.; Malik, A.; Richter, A. G.; Yu, C. J.; Eisenhower, R.; Dutta, P., Ordered phases in Langmuir monolayers of an azobenzene derivative. Langmuir 1998, 14, (4), 899-903.

68. Ekins, R.; Chu, F. W., Microarrays: their origins and applications. Trends in Biotechnology 1999, 17, (6), 217-218.

69. Faetti, S., Azimuthal anchoring energy of a nematic liquid crystal at a grooved interface. Physical Review A 1987, 36, (1), 408-410.

70. Fainerman, V. B.; Vollhardt, D., Equation of state for monolayers under consideration of the two-dimensional compressibility in the condensed state. Journal of Physical Chemistry B 2003, 107, (14), 3098-3100.

71. Fang, J. Y.; Gehlert, U.; Shashidar, R.; Knobler, C. M., Imaging the azimuthal tilt order in monolayers by liquid crystal optical amplification. Langmuir 1999, 15, (2), 297-299.

72. Fazio, V. S. U.; Komitov, L.; Lagerwall, S. T., Alignment of nematic liquid crystals on mixed Langmuir-Blodgett monolayers. Thin Solid Films 1998, 329, 681-685.

73. Fazio, V. S. U.; Nannelli, F.; Komitov, L., Sensitive methods for estimating the anchoring strength of nematic liquid crystals on Langmuir-Blodgett monolayers of fatty acids. Physical Review E 2001, 63, (6).

74. Ferjani, S.; Choi, Y.; Pendery, J.; Petschek, R. G.; Rosenblatt, C., Mechanically Generated Surface Chirality at the Nanoscale. Physical Review Letters 2010, 104, (25), 4.

75. Ferjani, S.; Pendery, J.; Rosenblatt, C., Mechanically generated surface chirality: Control of chiral strength. Appl. Phys. Lett. 2010, 97, (12), 3.

76. Filas, R. W.; Patel, J. S., Chemically induced high-tilt surfaces for liquid crystals. Applied Physics Letters 1987, 50, (20), 1426-1428.

77. Fischer, E., Calculation of photostationary states in systems A<=>B when only A is known. Journal of Physical Chemistry 1967, 71, 3704-3706.

78. Fonseca, J. G.; Galerne, Y., Simple method for measuring the azimuthal anchoring strength of nematic liquid crystals. Appl. Phys. Lett. 2001, 79, (18), 2910-2912.

79. Frank, F. C., I. Liquid crystals. On the theory of liquid crystals. Discussions of the Faraday Society 1958, 25, 19-28.

80. Fuerstenau, D. W., Equilibrium and nonequilibrium phenomena associated with the adsorption of ionic surfactants at solid-water interfaces. Journal of Colloid and Interface Science 2002, 256, (1), 79-90.

81. Fuerstenau, D. W., Streaming Potential Studies on Quartz in Solutions of Aminium Acetates in Relation to the Formation of Hemi- micelles at the Quartz-Solution Interface. The Journal of Physical Chemistry 1956, 60, (7), 981-985.

82. Fuerstenau, D. W.; Colic, M., Self-association and reverse hemimicelle formation at solid-water interfaces in dilute surfactant solutions. Colloids and Surfaces a-Physicochemical and Engineering Aspects 1999, 146, (1-3), 33-47.

83. Fukuda, J.-i.; Yoneya, M.; Yokoyama, H., Consistent numerical evaluation of the anchoring energy of a grooved surface. Physical Review E 2009, 79, (1), 011705.

84. Gaines, G. L., Insouble Monolayers at Liquid-Gas Interfaces. Interscience Publishers: New York, 1966.

85. Geary, J. M.; Goodby, J. W.; Kmetz, A. R.; Patel, J. S., The Mechanism of Polymer Alignment of Liquid-Crystal Materials. J. Appl. Phys. 1987, 62, (10), 4100-4108.

86. Gopal, A.; Lee, K. Y. C., Morphology and collapse transitions in binary phospholipid monolayers. J. Phys. Chem. B 2001, 105, (42), 10348-10354.

87. Grant, L. M.; Ducker, W. A., Effect of substrate hydrophobicity on surface-aggregate geometry: Zwitterionic and nonionic surfactants. Journal of Physical Chemistry B 1997, 101, (27), 5337-5345.

88. Griffith, J. D., DNA-STRUCTURE - EVIDENCE FROM ELECTRON-MICROSCOPY. Science 1978, 201, (4355), 525-527.

89. Gu, T.; Rupprecht, H., Hemimicelle shape and size. Colloid & Polymer Science 1990, 268, (12), 1148-1150.

90. Guo, W.; Photos, P. J.; Vanderlick, T. K., Polymer Enhanced Fusion of Model Sperm Membranes as Induced by Calcium. Industrial & Engineering Chemistry Research 2006, 45, (16), 5512-5517.

91. Gupta, J. K.; Meli, M. V.; Teren, S.; Abbott, N. L., Elastic energy-driven phase separation of phospholipid monolayers at the nematic liquid-crystal-aqueous interface. Physical Review Letters 2008, 1, (4).

92. Gupta, V. K.; Abbott, N. L., Azimuthal anchoring transition of nematic liquid crystals on self-assembled monolayers formed from odd and even alkanethiols. Physical Review E 1996, 54, (5), R4540-R4543.

93. Gupta, V. K.; Abbott, N. L., Design of Surfaces for Patterned Alignment of Liquid Crystals on Planar and Curved Substrates Science 1997, 276, (5318), 1533-1536.

94. Gupta, V. K.; Skaife, J. J.; Dubrovsky, T. B.; Abbott, N. L., Optical Amplification of Ligand-Receptor Binding Using Liquid Crystals. Science 1998, 279, (5359), 2077-2080.

95. Gurrieri, S.; Wells, K. S.; Johnson, I. D.; Bustamante, C., Direct visualization of individual DNA molecules by fluorescence microscopy: Characterization of the factors affecting signal/background and optimization of imaging conditions using YOYO. Analytical Biochemistry 1997, 249, (1), 44-53.

96. Haaren, J. v., Wiping out dirty displays. Nature 2001, 411, 29-30.

97. Hartono, D.; Bi, X.; Yang, K.-L.; Yung, L.-Y. L., An Air-Supported Liquid Crystal System for Real-Time and Label-Free Characterization of Phospholipases and Their Inhibitors. Advanced Functional Materials 2008, 18, (19), 2938-2945.

98. Hartono, D.; Xue, C.-Y.; Yang, K.-L.; Yung, L.-Y. L., Decorating Liquid Crystal Surfaces with Proteins for Real-Time Detection of Specific Protein-Protein Binding. Advanced Functional Materials 2009, 19, (22), 3574-3579.

99. Hermanson, G. T., Bioconjugate Techniques. 2 ed.; Elsiver Academic Press: Amsterdam, Boston, 2008.

100. Hifeda, Y. F.; Rayfield, G. W., Evidence for first-order phase transitions in lipid and fatty acid monolayers. Langmuir 1992, 8, (1), 197-200.

101. Hiltrop, K.; Stegemeyer, H., On the Orientation of Liquid Crystals by Monolayers of Amphiphilic Molecules. Berichte der Bunsengesellschaft für physikalische Chemie 1981, 85, (7), 582-588.

102. Holmberg, A.; Blomstergren, A.; Nord, O.; Lukacs, M.; Lundeberg, J.; Uhlén, M., The biotin-streptavidin interaction can be reversibly broken using water at elevated temperatures. Electrophoresis 2005, 26, (3), 501-510.

103. Hong, L.; Sugimura, H.; Furukawa, T.; Takai, O., Photoreactivity of alkylsilane self-assembled monolayers on silicon surfaces and its application to preparing micropatterned ternary monolayers. Langmuir 2003, 19, (6), 1966-1969.

104. Hoogboom, J.; Clerx, J.; Otten, M. B. J.; Rowan, A. E.; Rasing, T.; Nolte, R. J. M., Novel alignment technique for LCD-biosensors. Chem. Commun. 2003, (23), 2856-2857.

105. Huibers, P. D. T.; Shah, D. O., Multispectral determination of soap film thickness. Langmuir 1997, 13, (22), 5995-5998.

106. Ichimura, K., Photoalignment of liquid-crystal systems. Chemical Reviews 2000, 100, (5), 1847-1873.

107. Ichimura, K.; Hayashi, Y.; Ishizuki, N., Photocontrol of Inplane Alignment of a Nematic Liquid-Crystal by a Photochromic Spiropyran Monolayer Absorbing Linearly Polarized-Light. Chemistry Letters 1992, (6), 1063-1066.

108. Ichimura, K.; Suzuki, Y.; Seki, T.; Hosoki, A.; Aoki, K., Reversible Change in Alignment Mode of Nematic Liquid-Crystals Regulated Photochemically by Command Surfaces Modified with an Azobenzene Monolayer. Langmuir 1988, 4, (5), 1214-1216.

109. Ichimura, K.; Tomita, H.; Kudo, K., Command surfaces .14. Photoregulation of in-plane alignment of a liquid crystal by the photoisomerization of stilbenes chemisorbed on a substrate silica surface. Liquid Crystals 1996, 20, (2), 161-169.

110. Ignes-Mullol, J.; Claret, J.; Albalat, R.; Crusats, J.; Reigada, R.; Romero, M. T. M.; Sagues, F., Texture changes inside smectic-C droplets in azobenzene langmuir monolayers. Langmuir 2005, 21, (7), 2948-2955.

111. Ignes-Mullol, J.; Claret, J.; Sagues, F., Star defects, boojums, and cardioid droplet shapes in condensed dimyristoylphosphatidylethanolamine monolayers. Journal of Physical Chemistry B 2004, 108, (2), 612-619.

112. Iimura, Y.; Kobayashi, N.; Kobayashi, S., A New Method for Measuring the Azimuthal Anchoring Energy of a Nematic Liquid Crystal. Japanese Journal of Applied Physics 1994, 33, (Part 2, No. 3B), L434.

113. Illumina BeadArray. http://www.illumina.com/technology/beadarray_technology.ilmn

114. Illumina, TruSeq. 2011.

115. Ishihara, S.; Wakemoto, H.; Nakazima, K.; Matsuo, Y., The effect of rubbed polymer films on the liquid crystal alignment. Liq. Cryst. 1989, 4, (6), 669 - 675.

116. Israelachvili, J. N., Intermolecular And Surface Forces. Academic Press: 1991.

117. Israelachvili, J., Self-Assembly in 2 Dimensions - Surface Micelles and DOmain Formation in Monolayers Langmuir 1994, 10, (10), 3774-3781.

118. Ito, Y.; Heydari, M.; Hashimoto, A.; Konno, T.; Hirasawa, A.; Hori, S.; Kurita, K.; Nakajima, A., The Movement of a Water Droplet on a Gradient Surface Prepared by Photodegradation. Langmuir 2007, 23, (4), 1845-1850.

119. Jerome, B., Surface Effects and Anchoring in Liquid-Crystals. Rep. Prog. Phys. 1991, 54, (3), 391-451.

120. Jiang, S.; Liu, M., Aggregation and Induced Chirality of an Anionic meso-Tetraphenylsulfonato Porphyrin (TPPS) on a Layer-by-Layer Assembled DNA/PAH Matrix. The Journal of Physical Chemistry B 2004, 108, (9), 2880-2884.

121. Kaganer, V. M.; Mohwald, H.; Dutta, P., Structure and phase transitions in Langmuir monolayers. Review of Modern Physics 1999, 71, (3), 779-819.

122. Kato, T.; Kameyama, M.; Ehara, M.; Iimura, K., Monodisperse two-dimensional nanometer size clusters of partially fluorinated long-chain acids. Langmuir 1998, 14, (7), 1786-1798.

123. Kennedy, G. C.; Matsuzaki, H.; Dong, S. L.; Liu, W. M.; Huang, J.; Liu, G. Y.; Xu, X.; Cao, M. Q.; Chen, W. W.; Zhang, J.; Liu, W. W.; Yang, G.; Di, X. J.; Ryder, T.; He, Z. J.; Surti, U.; Phillips, M. S.; Boyce-Jacino, M. T.; Fodor, S. P. A.; Jones, K. W., Large-scale genotyping of complex DNA. Nature Biotechnology 2003, 21, (10), 1233-1237.

124. Kim, M. H.; Im, S. H.; Park, O. O., Rapid fabrication of two- and three-dimensional colloidal crystal films via confined convective assembly. Adv. Funct. Mater. 2005, 15, (8), 1329-1335.

125. Kim, S. R.; Abbott, N. L., Rubbed Films of Functionalized Bovine Serum Albumin as Substrates for the Imaging of Protein–Receptor Interactions Using Liquid Crystals. Advanced Materials 2001, 13, (19), 1445-1449.

126. Kim, Y. B., Atomic force microscopy of rubbed polyimide aligning films for liquid crystal displays. Mol. Cryst. Liq. Cryst. Sci. Technol. Sect. A-Mol. Cryst. Liq. Cryst. 1995, 262, 89-98.

127. Kim, Y. B., Atomic force microscopy of rubbed polyimide aligning films for liquid crystal displays. Mol. Cryst. Liq. Cryst. Sci. Technol. Sect. A-Mol. Cryst. Liq. Cryst. 1995, 262, 89-98.

128. Kim, Y. J.; Zhuang, Z.; Patel, J. S., Effect of multidirection rubbing on the alignment of nematic liquid crystal. Appl. Phys. Lett. 2000, 77, (4), 513-515.

129. Kimmel, A.; Oliver, B., Methods in Enzymology. Elsiver: Amsterdam, 2006; Vol. 410.

130. Knobler, C. M.; Desai, R. C., Phase-Transitions in Monolayers. Annual Review of Physical Chemistry 1992, 43, 207-236.

131. Knobler, C. M.; Schwartz, D. K., Langmuir and self-assembled monolayers. Current Opinion in Colloid & Interface Science 1999, 4, (1), 46-51.

132. Krafft, M. P.; Goldmann, M., Monolayers made from fluorinated amphiphiles. Current Opinion in Colloid & Interface Science 2003, 8, (3), 243-250.

133. Krafft, M. P.; Riess, J. G., Highly fluorinated amphiphiles and colloidal systems, and their applications in the biomedical field. A contribution. Biochimie 1998, 80, (5-6), 489-514.

134. Kreatech http://www.kreatech.com/us/products/ulstm-labeling-kits/general-labeling-kits.html.

135. Lai, S. L.; Tan, W. L.; Yang, K.-L., Detection of DNA Targets Hybridized to Solid Surfaces Using Optical Images of Liquid Crystals. ACS Applied Materials & Interfaces,

136. Lamture, J. B.; LBeattie, K.; Burke, B. E.; Eggers, M. D.; Ehrlich, D. J.; Fowler, R.; Hollis, M. A.; Kosicki, B. B.; Reich, R. K.; Smith, S. R.; Varma, R. S.; Hogan, M. E., Direct detection of nucleic acid hybridization on the surface of a charge coupled device. Nucleic Acids Res. 1994, 22, (11), 2121-2125.

137. Larsson, A.; Carlsson, C.; Jonsson, M.; Albinsson, B., Charachterization of the Binding of the Fluorecent Dyes YO and YOYO to DNA by Polarized-LIght Spectroscopy Journal of the American Chemical Society 1994, 116, (19), 8459-8465.

138. Lee, B.-W.; Clark, N. A., Alignment of Liquid Crystals with Patterned Isotropic Surfaces. Science 2001, 291, (5513), 2576-2580.

139. Lee, E. S.; Vetter, P.; Miyashita, T.; Uchida, T., Orientation of Polymer-Molecules in Rubbed Alignment Layer and Surface Anchoring of Liquid-Crystals Japanese Journal of Applied Physics Part 2-Letters 1993, 32, (9B), L1339-L1341.

140. Lee, S. H.; Yoon, T. H.; Kim, J. C., Determination of azimuthal anchoring energy in a twisted nematic liquid crystal. Physical Review E 2005, 72, (6).

141. Lemieux, B.; Aharoni, A.; Schena, M., Overview of DNA chip technology. Molecular Breeding 1998, 4, (4), 277-289.

142. Lindroos, K.; Liljedahl, U.; Raitio, M.; Syvanen, A.-C., Minisequencing on oligonucleotide microarrays: comparison of immobilisation chemistries. Nucl. Acids Res. 2001, 29, (13), e69-.

143. Liu, X.; Krull, U. J., DNA hybridization on silica microbeads that are physically adsorbed as arrays on glass surfaces. Anal. Chim. Acta 2006, 562, (1), 1-8.

144. Lockwood, N. A.; Abbott, N. L., Self-assembly of surfactants and phospholipids at interfaces between aqueous phases and thermotropic liquid crystals. Current Opinion in Colloid & Interface Science 2005, 10, (3-4), 111-120.

145. Lockwood, N. A.; dePablo, J. J.; Abbott, N. L., Influence of Surfactant Tail Branching and Organization on the Orientation of Liquid Crystals at Aqueous-Liquid Crystal Interfaces. Langmuir 2005, 21, (15), 6805-6814.

146. Luk, Y.-Y.; Tingey, M. L.; Hall, D. J.; Israel, B. A.; Murphy, C. J.; Bertics, P. J.; Abbott, N. L., Using Liquid Crystals to Amplify Protein-Receptor Interactions: Design of Surfaces with Nanometer-Scale Topography that Present Histidine-Tagged Protein Receptors. Langmuir 2003, 19, (5), 1671-1680.

147. Luminex http://www.luminexcorp.com/TechnologiesScience/xMAPTechnology/index.htm

148. Luzzati, V.; Husson, F., STRUCTURE OF LIQUID-CRYSTALLINE PHASES OF LIPID-WATER SYSTEMS. J. Cell Biol. 1962, 12, (2), 207-&.

149. Maaloum, M.; Muller, P.; Krafft, M. P., Lateral and vertical nanophase separation in Langmuir-Blodgett films of phospholipids and semifluorinated alkanes. Langmuir 2004, 20, (6), 2261-2264.

150. Malone, S. M.; Schwartz, D. K., Polar and Azimuthal Alignment of a Nematic Liquid Crystal by Alkylsilane Self-Assembled Monolayers: Effects of Chain-Length and Mechanical Rubbing Langmuir 2008, 24, (17), 9790-9794.

151. Manifacier, J. C.; Gasiot, J.; Fillard, J. P., Simple Method for Determination of Optical Constants n,k, and Thickness of a Weakly Absorbing Thin Film Journal of Physics E-Scientific Instruments 1976, 9, (11), 1002-1004.

152. Manne, S.; Cleveland, J. P.; Gaub, H. E.; Stucky, G. D.; Hansma, P. K., Direct Visualization of Surfactant Hemimicelles by Force Microscopy of the Electrical Double-Layer Langmuir 1994, 10, (12), 4409-4413.

153. Manne, S.; Gaub, H. E., Molecular-Organization of Surfactants at Solid-Liquid Interfaces Science 1995, 270, (5241), 1480-1482..

154. Manne, S.; Schaffer, T. E.; Huo, Q.; Hansma, P. K.; Morse, D. E.; Stucky, G. D.; Aksay, I. A., Gemini surfactants at solid-liquid interfaces: Control of interfacial aggregate geometry. Langmuir 1997, 13, (24), 6382-6387.

155. Marinont-Legarde, P.; Dozov, I.; Polossat, E.; Auroy, E. R. P.; Ramdane, O. O.; Durand, G.; Forget, S. Liquid crystal device comprising anchoring means on at least one confinement. 2002.

156. Moon, D. W.; Kurokawa, A.; Ichimura, S.; Lee, H. W.; Jeon, I. C., Ultraviolet-ozone jet cleaning process of organic surface contamination layers. Journal of Vacuum Science & Technology A: Vacuum, Surfaces, and Films 1999, 17, (1), 150-154..

157. Mourran, A.; Tartsch, B.; Gallyamov, M.; Magonov, S.; Lambreva, D.; Ostrovskii, B. I.; Dolbnya, I. P.; de Jeu, W. H.; Moeller, M., Self-assembly of the perfluoroalkyl-alkane F14H20 in ultrathin films. Langmuir 2005, 21, (6), 2308-2316.

158. Murauski, A.; Chigrinov, V.; Muravsky, A.; Yeung, F. S.-Y.; Ho, J.; Kwok, H.-S., Determination of liquid-crystal polar anchoring energy by electrical measurements. Physical Review E 2005, 71, (6), 061707.

159. Nakajima, Y.; Saito, K.; Murata, M.; Uekita, M., The Pretitlt Angle Controllable Polyimide Langmuir-Blodgett-Film for Nematic Liquid Crystals Mol. Cryst. Liq. Cryst. Sci. Technol. Sect. A-Mol. Cryst. Liq. Cryst. 1993, 237, 111-119.

160. Nakata, M.; Zanchetta, G.; Buscaglia, M.; Bellini, T.; Clark, N. A., Liquid Crystal Alignment on a Chiral Surface: Interfacial Interaction with Sheared DNA Films. Langmuir 2008, 24, (18), 10390-10394.

161. Nelson, M.; Cain, N.; Taylor, C. E.; Ocko, B. M.; Gin, D. L.; Hammond, S. R.; Schwartz, D. K., Periodic arrays of interfacial cylindrical reverse micelles. Langmuir 2005, 21, (22), 9799-9802.

162. Nespoulous, M.; Blanc, C.; Nobili, M., Ultraweak azimuthal anchoring of a nematic liquid crystal on a planar orienting photopolymer. J. Appl. Phys. 2007, 102, (7), 073519.

163. Nosonovsky, M.; Bhushan, B., Cassie-Wenzel Wetting Regime Transition Multiscale Dissipative Mechanisms and Hierarchical Surfaces. In Springer Berlin Heidelberg: 2008; pp 153-167.

164. Ogawa, K.; Mino, N.; Nakajima, K., Control of Pretilt Angles of Liquid Crystal Molecules in a Liquid Crystal Cell Using a Chemically Adsorbed Monolayer as an Alignment Film. Japanese Journal of Applied Physics 1990, 29, (9), L1689-L1692.

165. Ouchi, Y.; Feller, M. B.; Moses, T.; Shen, Y. R., Surface Memory Effect at the Liquid-Crystal-Polymer Interface. Physical Review Letters 1992, 68, (20), 3040-3043.

166. Pallas, N. R.; Pethica, B. A., Liquid-expanded to liquid-condensed transition in lipid monolayers at the air/water interface. Langmuir 1985, 1, (4), 509-513.

167. Papoular, M.; Rapini, A., Ondes de Surface Dans Un Cristal Liquode Nematique. J. Phys. Colloques 1970, 31, (C1), C1-27-C1-28.

168. Park, S. J.; Jang, C. H., Using liquid crystals to detect DNA hybridization on polymeric surfaces with continuous wavy features. Nanotechnology 2010, 21, (42), 7.

169. Patrick, H. N.; Warr, G. G.; Manne, S.; Aksay, I. A., Surface micellization patterns of quaternary ammonium surfactants on mica. Langmuir 1999, 15, (5), 1685-1692..

170. Perkins, T. T.; Smith, D. E.; Chu, S., Single Polymer Dynamics in an Elongational Flow. Science 1997, 276, (5321), 2016-2021.

171. Petty, M. C., Langmuir-Blodgett Films: An Introduction. Cambridge University Press: Cambridge, 1996.

172. Pineiro, A.; Prieto, G.; Ruso, J. M.; Verdes, P. V.; Sarmiento, F., Surface films of short fluorocarbon-hydrocarbon diblocks studied by molecular dynamics simulations: Spontaneous formation of elongated hemimicelles. Journal of Colloid and Interface Science 2009, 329, (2), 351-356.

173. Pires, D.; Galerne, Y., Anchoring and memory of the azimuthal nematic orientation. Appl. Phys. Lett. 2006, 89, (14), 3.

174. Price, A. D.; Ignes-Mullol, J.; Angels Vallve, M.; Furtak, T. E.; Lo, Y.-A.; Malone, S. M.; Schwartz, D. K., Liquid crystal anchoring transformations induced by phase transitions of a photoisomerizable surfactant at the nematic/aqueous interface. Soft Matter 2009, 5, (11), 2252-2260.

175. Price, A. D.; Schwartz, D. K., Anchoring of a nematic liquid crystal on a wettability gradient. Langmuir 2006, 22, (23), 9753-9759.

176. Price, A. D.; Schwartz, D. K., DNA Hybridization-Induced Reorientation of Liquid Crystal Anchoring at the Nematic Liquid Crystal/Aqueous Interface. J. Am. Chem. Soc. 2008, 130, (26), 8188-8194.

177. Price, A. D.; Schwartz, D. K., Fatty-Acid Monolayers at the Nematic/Water Interface: Phases and Liquid-Crystal Alignment. J. Phys. Chem. B 2007, 111, (5), 1007-1015.

178. Punkkinen, O.; Hansen, P. L.; Miao, L.; Vattulainen, I., DNA Overstretching Transition: Ionic Strength Effects. Biophysical Journal 2005, 89, (2), 967-978.

179. Raj, A.; van den Bogaard, P.; Rifkin, S. A.; van Oudenaarden, A.; Tyagi, S., Imaging individual mRNA molecules using multiple singly labeled probes. Nat Meth 2008, 5, (10), 877-879.

180. Ramdane, O. O.; Auroy, P.; Forget, S.; Raspaud, E.; Martinot-Lagarde, P.; Dozov, I., Memory-Free Conic Anchoring of Liquid Crystals on a Solid Substrate. Physical Review Letters 2000, 84, (17), 3871.

181. Rasing, T.; I., M., Surfaces and Interfaces of Liquid Crystals. Springer: New York, 2004.

182. Raszewski, Z.; Rutkowska, J.; Kedzierski, J.; Zielinski, J.; Perkowski, P.; Piecek, W.; Zmija, J., DIELECTRIC METHOD OF DETERMINATION OF THE ASSOCIATION ENERGY BETWEEN POLAR-MOLECULES IN NEMATIC LIQUID-CRYSTAL. Molecular Crystals and Liquid Crystals Science and Technology Section a-Molecular Crystals and Liquid Crystals 1994, 251, 357-365.

183. Rau, H.; Greiner, G.; Gauglitz, G.; Meier, H., Photochemical Quantum yields in the A(+hv)<=>B (+hv,delta) system when only the spectrum of A is known. Journal of Physical Chemistry 1990, 94, 6523-6524.

184. Reuter, M.; Dryden, D. T. F., The kinetics of YOYO-1 intercalation into single molecules of double-stranded DNA. Biochemical and Biophysical Research Communications 403, (2), 225-229.

185. Riess, J. G.; Krafft, M. P., Fluorinated materials for in vivo oxygen transport (blood substitutes), diagnosis and drug delivery. Biomaterials 1998, 19, (16), 1529-1539.

186. Rinia, H. A.; de Kruijff, B., Imaging domains in model membranes with atomic force microscopy. FEBS Letters 2001, 504, (3), 194-199.

187. Riviere, S.; Henon, S.; Meunier, J.; Schwartz, D. K.; Tsao, M. W.; Knobler, C. M., Textures and Phase Transitinos in Langmuir Monolayers of Fatty Acids - A Comparative Brewster-Angle Microscope and Polarized Fluorescence Microscope Study Journal of Chemical Physics 1994, 101, (11), 10045-10051.

188. Ruetschi, M.; Grutter, P.; Funfschilling, J.; Guntherodt, H. J., Creation of Liquid-Crystal Wave-Guides wiht Scanning Force Microscopy. Science 1994, 265, (5171), 512-514.

189. Rye, H. S.; Yue, S.; Wemmer, D. E.; Quesada, M. A.; Haugland, R. P.; Mathies, R. A.; Glazer, A. N., Stable fluorescent complexes of double-stranded DNA with bis-intercalating asymmetric cyanine dyes: properties and applications. Nucleic Acids Research 1992, 20, (11), 2803-2812.

190. Safran, S. A., Statistical Thermodynamics of Surfaces, Interfaces, and Membranes. Addison-Wesley Publishing Company: Reading, Massachusetts, 1994; Vol. 90.

191. Sakamoto, K.; Arafune, R.; Ito, N.; Ushioda, S.; Suzuki, Y.; Morokawa, S., Molecular Orienatation fo Rubbed an Unrubbed Polyimide Films Determined by Polarized Infrared Absorption. Japanese Journal of Applied Physics 1994, 33, L1323-L1326.

192. Sambrook, J., Molecular Cloning: A laboratory Manual. 3 ed.; Cold Spring Harbor Laboratory Press: 2001; Vol. 1.

193. Sassolas, A.; Leca-Bouvier, B. D.; Blum, L. J., DNA biosensors and microarrays. Chem. Rev. 2008, 108, (1), 109-139.

194. Sato, Y.; Sato, K.; Uchida, T., RELATIONSHIP BETWEEN RUBBING STRENGTH AND SURFACE ANCHORING OF NEMATIC LIQUID-CRYSTAL. Japanese Journal of Applied Physics Part 2-Letters 1992, 31, (5A), L579-L581.

195. Schadt, M.; Schmitt, K.; Kozinkov, V., Surface Induced Parallel Alignment of LIquid Crystals by Linearly Polymerized Photopolymers. Japanese Journal of Applied Physics 1992, 31, 2155-2164.

196. Schena, M., Charting the microarray revolution. Scientist 2004, 18, (19), 30-31.

197. Schena, M., Microarray Analysis. Wiley-Liess: 2003.

198. Schena, M., Protein Microarrays. Jones and Bartelett Publishers Sudbury, MA, 2005.

199. Schena, M.; Heller, R. A.; Theriault, T. P.; Konrad, K.; Lachenmeier, E.; Davis, R. W., Microarrays: biotechnology's discovery platform for functional genomics. Trends in Biotechnology 1998, 16, (7), 301-306.

200. Schena, M.; Shalon, D.; Davis, R. W.; Brown, P. O., Quantitative Monitoring of Gene Expression Patterns with a Complementary DNA Microarray. Science 1995, 270, (5235), 467-470.

201. Schena, M.; Shalon, D.; Heller, R.; Chai, A.; Brown, P. O.; Davis, R. W., Parallel human genome analysis: Microarray-based expression monitoring of 1000 genes. Proceedings of the National Academy of Sciences of the United States of America 1996, 93, (20), 10614-10619.

202. Schurr, J. M.; Smith, S. B., Theory for the extension of a linear polyelectrolyte attached at one end in an electric field. Biopolymers 1990, 29, (8-9), 1161-1165.

203. Schwartz, D. K., Langmuir-Blodgett film structure. Surface Science Reports 1997, 27, (7-8), 245-334.

204. Seo, D. S.; Kobayashi, S.; Kang, D. Y.; Yokoyama, H., Effects of Rubbing and Temperature-Dependence of Polar Anchoring Strength of Homogeneously Aligned Nematic Liquid-Crystal on Polyimide Langmuir-Blodgett Orientation Films Japanese Journal of Applied Physics Part 1-Regular Papers Brief Communications & Review Papers 1995, 34, (7A), 3607-3611.

205. Seo, D.-S., Investigation of surface anchoring strength and pretilt angle in NLC on rubbed polythiophene surfaces with alkyl chain lengths.Liquid Crystals 1999, 26, (11), 1621-1624.

206. Seo, D.-S.; Choi, J.-H., Preliminary communication Generation of high pretilt angle in a nematic liquid crystal with single oblique polarized UV light irradiation on polyimide surfaces. Liquid Crystals 1999, 26, (2), 291-293.

207. Seo, D.-S.; Han, J.-M., Generation of pretilt angle in NLCs and EO characteristics of a photo-aligned TN-LCD with oblique non-polarized UV light irradiation on a polyimide surface. Liq. Cryst. 1999, 26, (7), 959-964.

208. Seo, D.-S.; Hwang, L.-Y.; Lee, B.-H. In A study on mechanism of pretilt angle generation in nematic liquid crystal for rubbed polyimide surfaces, Properties and Applications of Dielectric Materials, 1997., Proceedings of the 5th International Conference on, 1997; Hwang, L.-Y., Ed. 1997; pp 946-948 vol.2.

209. Singh, V.; Zharnikov, M.; Gulino, A.; Gupta, T., DNA immobilization, delivery and cleavage on solid supports. Journal of Materials Chemistry 2011, 21, (29), 10602-10618.

210. Sinha, G. P.; Wen, B.; Rosenblatt, C., Large, continuously controllable nematic pretilt from vertical orientation. Applied Physics Letters 2001, 79, (16), 2543-2545.

211. Smith, S.; Finzi, L.; Bustamante, C., Direct mechanical measurements of the elasticity of single DNA molecules by using magnetic beads. Science 1992, 258, (5085), 1122-1126.

212. Sonin, A. A., The Surface Physics of Liquid Crystals. Gordon and Breach Publishers: New York, 1995.

213. Sprokel, G. J., RESISTIVITY, PERMITTIVITY AND ELECTRODE SPACE-CHARGE OF NEMATIC LIQUID-CRYSTALS. Molecular Crystals and Liquid Crystals 1973, 22, (3-4), 249-260.

214. Stigter, D.; Bustamante, C., Theory for the Hydrodynamic and Electrophoretic Stretch of Tethered B-DNA. Biophysical Journal 1998, 75, (3), 1197-1210.

215. Stoenescu, D. N.; Nguyen, H. T.; Barois, P.; Navailles, L.; Nobili, M.; Martinot-Lagarde, P.; Dozov, I., Optical Studies of Chiral Mesophases in Sandwich Cells with Planar Degenerated Anchoring. Molecular Crystals and Liquid Crystals Science and Technology. Section A. Molecular Crystals and Liquid Crystals 2001, 358, (1), 275-286.

216. Stohr, J.; Samant, M. G., Liquid crystal alignment by rubbed polymer surfaces: a microscopic bond orientation model. Journal of Electron Spectroscopy and Related Phenomena 1999, 99, 189-207.

217. Stohr, J.; Samant, M. G.; Cossy-Favre, A.; Diaz, J.; Momoi, Y.; Odahara, S.; Nagata, T., Microscopic origin of liquid crystal alignment on rubbed polymer surfaces. Macromolecules 1998, 31, (6), 1942-1946.

218. Tanford, C., Theory of Micelle Formation in Aqueous Solutions. Journal of Physical Chemistry 1974, 78, (24), 2469-2479.

219. Tanford, C., Thermodynamics of Micelle Formation - Prediction of Micelle Size and Size Distribution Proceedings of the National Academy of Sciences of the United States of America 1974, 71, (5), 1811-1815.

220. Trabelsi, S.; Zhang, S. S.; Zhang, Z. C.; Lee, T. R.; Schwartz, D. K., Semi-fluorinated phosphonic acids form stable nanoscale clusters in Langmuir-Blodgett and self-assembled monolayers. Soft Matter 2009, 5, (4), 750-758.

221. Trabelsi, S.; Zhang, S.; Lee, T. R.; Schwartz, D. K., Linactants: Surfactant analogues in two dimensions. Physical Review Letters 2008, 1, (3).

222. Trabelsi, S.; Zhang, S.; Lee, T. R.; Schwartz, D. K., Swelling of a cluster phase in Langmuir monolayers containing semi-fluorinated phosphonic acids. Soft Matter 2007, 3, (12), 1518-1524.

223. Trabelsi, S.; Zhang, Z.; Zhang, S.; Lee, T. R.; Schwartz, D. K., Correlating Linactant Efficiency and Self-Assembly: Structural Basis of Line Activity in Molecular Monolayers Langmuir

224. Uchida, T.; Hirano, M.; Sakai, H., Director Orientation of a Ferroelectric Liquid-Crystal on Substrates with Rubbing Treatment - The Effect of Surface Anchoring Strength Liq. Cryst. 1989, 5, (4), 1127-1137.

225. Uyama, Y.; Inoue, H.; Ito, K.; Kishida, A.; Ikada, Y., Comparison of Different Methods for Contact-Angle Measurement Journal of Colloid and Interface Science 1991, 141, (1), 275-279.

226. Van Doorn, C. Z.; Gerritsma, C. J.; deKlerk, J. J. M. J., Influence of the Device Parameters on the Performance of Twisted-Nematic Liquid Crystal Matrix Displays. Plenium Press: New York, 1980.

227. Vanaerle, N.; Barmentlo, M.; Hollering, R. W. J., Effect of Rubbingon the Molecular-Orientation Within Polyimide Orienting Layers of Liquid-Crystal Displays J. Appl. Phys. 1993, 74, (5), 3111-3120.

228. Vaughn, K. E.; Sousa, M.; Kang, D.; Rosenblatt, C., Continuous control of liquid crystal pretilt angle from homeotropic to planar. Applied Physics Letters 2007, 90, (19), 194102.

229. Walba, D. M.; Liberko, C. A.; Korblova, E.; Farrow, M.; Furtak, T. E.; Chow, B. C.; Schwartz, D. K.; Freeman, A. S.; Douglas, K.; Williams, S. D.; Klittnick, A. F.; Clark, N. A., Self-assembled monolayers for liquid crystal alignment: simple preparation on glass using alkyltrialkoxysilanes. Liq. Cryst. 2004, 31, (4), 481 - 489.

230. Walba, D. M.; Liberko, C. A.; Shao, R.; Clark, N. A., Smectic liquid crystal alignment using mechanically rubbed n-octadecylsiloxane self-assembled monolayers. Liq. Cryst. 2002, 29, (8), 1015 - 1024.

231. Wan, J. T. K.; Tsui, O. K. C.; Kwok, H.-S.; Sheng, P., Liquid crystal pretilt control by inhomogeneous surfaces. Physical Review E 2005, 72, 021711 1-4.

232. Wanless, E. J.; Davey, T. W.; Ducker, W. A., Surface aggregate phase transition. Langmuir 1997, 13, (16), 4223-4228.

233. Wanless, E. J.; Ducker, W. A., Weak influence of divalent ions on anionic surfactant surface-aggregation. Langmuir 1997, 13, (6), 1463-1474.

234. Wei, X.; Hong, S.-C.; Zhuang, X.; Goto, T.; Shen, Y. R., Nonlinear optical studies of liquid crysral alignment on a rubbed polyvinyl alcohol surface. Physical Review E 2000, 62, (4), 5160-5172.

235. Wenzel, R. N., Resistance of Solid Surfaces to Wetting by Water Industrial & Engineering Chemistry 1936, 28, (8), 988-994.

236. Wolgemuth, J. L.; Workman, R. K.; Manne, S., Surfactant aggregates at a flat, isotropic hydrophobic surface. Langmuir 2000, 16, (7), 3077-3081.

237. Ye, T.; McArthur, E. A.; Borguet, E., Mechanism of UV Photoreactivity of Alkylsiloxane Self-Assembled Monolayers. The Journal of Physical Chemistry B 2005, 109, (20), 9927-9938.

238. Ye, T.; McArthur, E. A.; Borguet, E., Mechanism of UV Photoreactivity of Alkylsiloxane Self-Assembled Monolayers. The Journal of Physical Chemistry B 2005, 109, (20), 9927-9938.

239. Ye, T.; Wynn, D.; Dudek, R.; Borguet, E., Photoreactivity of Alkylsiloxane Self-Assembled Monolayers on Silicon Oxide Surfaces. Langmuir 2001, 17, (15), 4497-4500.

240. Yim, K. S.; Fuller, G. G., Influence of phase transition and photoisomerization on interfacial rheology. Physical Review E 2003, 67, (4).

241. Zasadzinski, J.; Viswanathan, R.; Madsen, L.; Garnaes, J.; Schwartz, D., Langmuir-Blodgett films. Science 1994, 263, (5154), 1726-1733.

242. Zhang, G. F.; Maaloum, M.; Muller, P.; Benoit, N.; Krafft, M. P. In Surface micelles of semifluorinated alkanes in Langmuir-Blodgett monolayers, 2004; 2004; pp 1566-1569.

243. Zhuang, X.; Marrucci, L.; Shen, Y. R., Surface-Monolayer-Induced Bulk Alignment of Liquid Crystals. Physical Review Letters 1994, 73, 1513-1516.

244. Zou, L. N.; Li, Y. M.; Ye, B. X., Voltammetric sensing of guanine and adenine using a glassy carbon electrode modified with a tetraoxocalix[2]arene[2]triazine Langmuir-Blodgett film. Microchim. Acta 173, (3-4), 285-291.

Appendix A

Liquid Crystal Anchoring Transitions Induced by Phase Transitions of Photisomerizable Surfactant at the Nematic/Aqueous Interface

A photoisomerizable fatty acid (containing an azobenzene unit) was dissolved in a nematic liquid crystal and adsorbed at the liquid crystal /water interface, influenceing the anchoring of the liquid crystal material. The liquid crystalline phase was observed to reorient upon exposure to different irradiation wavelengths. Homeotropic, tilted, and planar anchoring were all observed under various thermodynamic and illumination conditions. Lateral coexistence between regions displaying different anchoring was often observed, as were dynamic and reversible transitions between the various states. These observations suggest that adsorbed monolayers of the azobenzene-fatty acid (probably in equilibrium with the same surfactant in solution) display a rich binary phase diagram, where the relative fractions of cis and trans isomers are determined by the photostationary state associated with the illumination wavelength. The morphology of these phase diagrams has been determined as a function of three variables—bulk concentration, temperature, and composition (cis:trans ratio) of the dissolved surfactant—and six distinct interfacial phases were identified, including five condensed phases and a dilute interfacial vapor phase. This phase diagram is distinct from the behavior of Langmuir monolayers of the same amphiphile at the air/water interface, which exhibits only two condensed phases.

A.1 Introduction

We have previously introduced the topic of alignment layers in respect to liquid crystalline polar alignment. While we have previously focused on liquid crystal alignment at the solid/liquid crystal interface, alignment is also commonly studied at the liquid/liquid crystal interface[1-3]. Physical and chemical properties of surface (alignment layer) define a preferred orientation of neighboring liquid crystal molecules, which the bulk will then align in concert with.[4, 5] Monolayers partitioning to aqueous/liquid crystal interface have been shown to affect liquid crystal alignment.[6 7] What is more subtle, however, is their ability to amplify changes within the monolayer. This amplification allows extremely sensitive detection of interfacial properties. All liquid crystals devices exploit this sensitivity to surface conditions by using alignment layers to impart the desired anchoring for application purposes. Of particular interest are dynamic alignment layers that cause liquid crystal alignment switching in response to a stimulus. Photo-responsive surfaces are a classic example, in which surface coatings are prepared from molecules containing photoisomerizable moieties such as azobenzenes, stilbenes, or spiropyrans.[8-11] Typically, these molecules are immobilized on a solid surface, and the conformational change associated with isomerization can switch the adjacent liquid crystal phase between two orientational states. However, study of these molecules at the liquid/liquid crystal interface provides allows more facile reorientation of the liquid crystals, and can lead to further understanding of intermolecular liquid crystal anchoring mechanisms. While there is a significant literature involving two-dimensional phase diagrams of amphiphilic monolayers at the air/water interface,[12] monolayers at the liquid/liquid or liquid/liquid crystal interface are less well-understood.

Recent work suggests that the presence of an adjacent nematic phase may have a significant effect on the phase behavior of a monolayer. This group has previously showed that the phase diagrams of fatty acid monolayers shift dramatically at the nematic/water interface.[7] For example, a particular triple point was nearly 40 ˚C lower at the nematic/water interface than at the air/water interface. Recently, Abbot and coworkers observed phase coexistence in the phospholipid monolayer at the nematic/water interface under thermodynamic conditions where no coexistence was observed at the air/water or isotropic liquid crystal/water interfaces.[13]

In this work, the photoisomerizable molecules are azobenezene-containing amphiphilic fatty acids. The cis or trans isomers are switchable by exposure to radiation of varying wavelengths. These are dissolved in the liquid crystal phase and allowed to adsorb at the fluid interface between a nematic liquid crystal and water. We observe a variety of orientational states of the liquid crystal: as a function of surfactant concentration, temperature, and wavelength of irradiation (which establishes the relative *trans* and *cis* isomer composition) – as well as lateral coexistence between many of these states under appropriate conditions. Continuous and discontinuous transitions are observed between these states upon changing irradiation wavelengths. This suggests that upon steady exposure to a particular wavelength of light, a specific binary mixture of *cis* and *trans* isomers is reached at the interface, in equilibrium with the photostationary state mixture in solution (whose composition we measure). In general, the *cis/trans* composition in solution and at the interface need not be identical, as it cannot be assumed that cis/trans isomers have the same equilibrium constant. The surface layer adopts an equilibrium two-dimensional phase (or mixture of phases) at the

interface depending on the temperature, surface concentration and cis/trans composition. The orientation and texture of the adjacent liquid crystal phase reflects the molecular arrangement of these interfacial phases. In this chapter, we report systematic observations of this phenomenology as a function of temperature, surfactant concentration, and photostationary state composition, and show that interaction of a surfactant monolayer with a bulk nematic phase can not only shift the phase behavior of the monolayer from that at the air/water interface, it can also induce the appearance of entirely new phases and modify the lateral miscibility of monolayer components.

Previous work on azo-fatty acid monolayers at the air/water interface showed the formation of an isotropic liquid phase for *cis*-rich monolayers and a smectic C phase for pure *trans* monolayers.[14] The two phases coexisted at all temperatures and over a wide range of compositions in mixed *cis/trans* monolayers, revealing a remarkable immiscibility of the two isomeric components at the air/water interface. The structures and phase behavior at the air/water interface are faithfully transferred onto a solid support, and visualized in a liquid crystal cell[15]. In contrast, the current work at the liquid crystal/water interface reveals the existence of two phases where the two isomers in the mixed monolayers are totally miscible.

A.2 Results

A.2.1 Photostationary State Spectra and Thermal Relaxation

The spectra of the thermally-relaxed, nearly all *trans* state, and of the three photostationary states associated with illumination by 436 nm, 405 nm, and 365 nm radiation of the azobenzene monolayer are shown in Figure A.2. Optical pumping at these wavelengths determines the cis/trans ratio, thus enforcing new photostationary states.

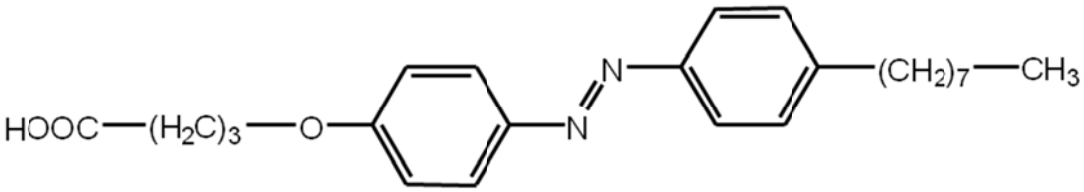

Figure A.1: Structure of the azobenzene fatty acid (8Az3) used in this work.

The *trans* isomer exhibits an absorbance peak at ~370 nm, while the *cis* isomer is characterized by a broad absorbance peak centered at ~450 nm. The minor dips in the absorbance spectra at the pump wavelength for a particular photostationary state are artifacts caused by a small amount pump light that enters the spectrometer optics. The progression of spectra with decreasing pumping wavelength qualitatively indicates an increasing fraction of the *cis* isomer. Quantitative values of the *cis* isomer fraction were determined using the method of Fischer and Rau,[16-18] which involves comparing the dark spectrum to photostationary state spectra acquired with two pumping wavelengths. Since we obtained spectra of three photostationary states, we were able

to calculate each composition using two independent pairs of spectra as a consistency check. The *cis* isomer fractions of the photostationary states are given in Table A.1.

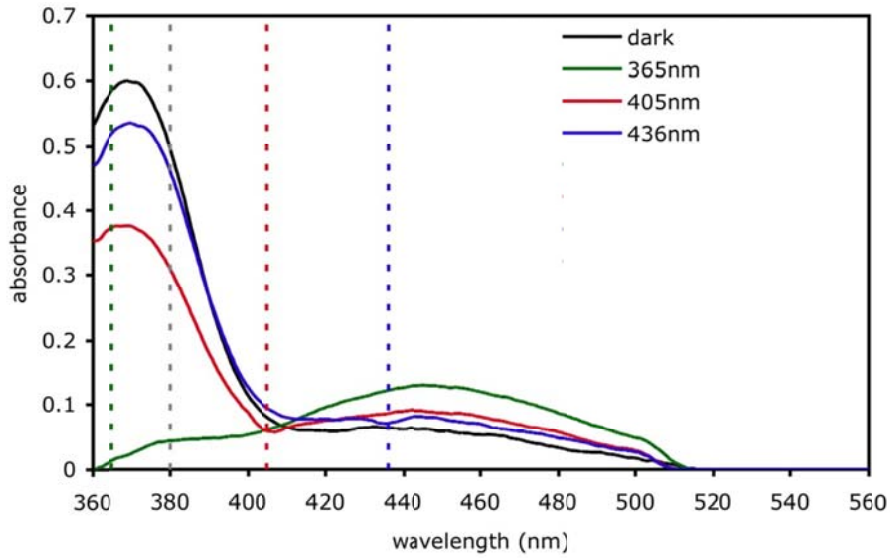

Figure A.2: UV/Vis spectra of the various photostationary states examined in this work. The legend labels identify the wavelength of the simultaneous pump illumination, with "dark" referring to the thermally-relaxed state. The vertical lines indicate the optical pumping wavelengths that used for *cis/trans* composition calculations. The minor dips in the absorbance spectra at the pump wavelength for a particular photostationary state are artifacts caused by a small amount pump light that enters the spectrometer optics.

Table A.1: Isomeric compositions of photostationary states.

	Photostationary states used in calculation			
	436 nm / 405 nm	436 nm / 365 nm	405 nm / 365 nm	average
cis fraction @ 436 nm	0.087	0.076	X	0.082
cis fraction @ 405 nm	0.457	X	0.398	0.428
cis fraction @ 365 nm	X	0.977	0.975	0.976

The kinetics of thermal relaxation was also measured by following the intensity at 380 nm as the sample was allowed to relax in darkness from an initial condition of the 365-nm photostationary state. The kinetic data are shown in Figure A.3 suggest first-order relaxation kinetics with a time constant of 6800s or 113 min. This relaxation time is typical of azobenzene-based materials in relatively nonpolar solvents.[19] The long relaxation suggests that the *cis* isomer fraction is defined only by the wavelength of the pump illumination and that the system reaches a true photostationary state, even at the significantly higher concentrations used in the microscopy experiments.

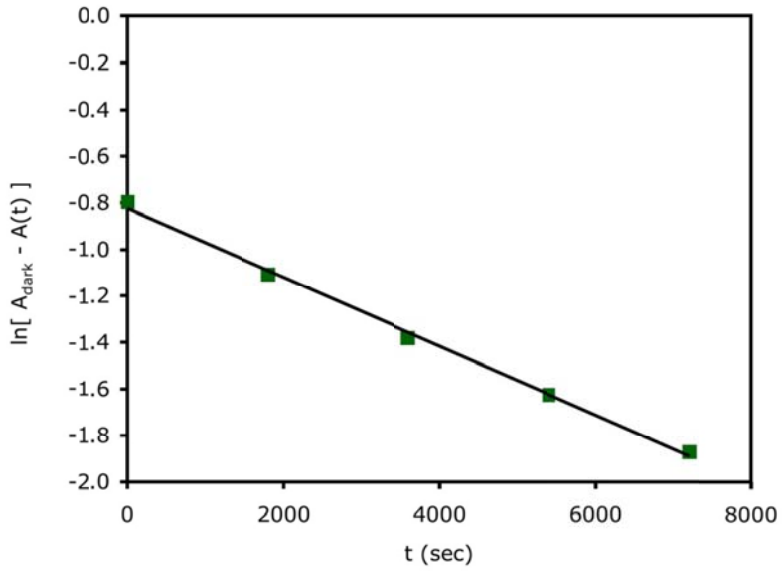

Figure A.3: Thermal relaxation kinetics data showing the recovery of the spectral intensity at 380nm from the value associated with the 365-nm photostationary state to that of the dark state. The data are consistent with first-order kinetics with a time constant of ~113min.

A.2.2 Polarized light microscopy observations

As described previously, immediately upon immersion of the liquid crystal-filled grid in ultrapure water, the liquid crystal appeared highly birefringent as is usual for a liquid crystal/aqueous interface in the absence of an adsorbed monolayer. The sample was kept immersed in the dark for at least 60 minutes to allow interfacial adsorption to occur. Following this procedure, the liquid crystal phase adopted characteristic textures and birefringence colors depending on the specific experimental conditions (8Az3 concentration, temperature, and illumination wavelength). Anchoring effects due to the gold-coated grid surface were limited to a small region within a few μm of the grid edge. Given the distinctive liquid crystal anchoring, the amphiphilic nature of 8Az3, and the hydrophobic/hydrophilic character of the liquid crystal/water interface, it is reasonable to

assume that 8Az3 molecules adsorb to the interface in the standard surfactant orientation to form a (partial or complete) interfacial monolayer.

We found that the liquid crystal appearance changed dynamically when the irradiation wavelength was varied. Representative behavior is illustrated in Figure A.4, where the initial condition, associated with the stationary state induced by 436 nm illumination, involved the coexistence of small homeotropic regions (black) and regions with weak birefringence (light gray). When the illumination wavelength was switched abruptly to 365 nm, a distinctive sequence of textures was observed over a period of ~60 seconds. First, the birefringent regions grew to cover the entire sample. Then the weakly-birefringent texture abruptly became homeotropic. Finally, strongly birefringent regions (blue/green and pink) appeared within the homeotropic sample and grew to cover a significant fraction of the sample. This final state was stable upon continued illumination at 365 nm. If the illumination wavelength was switched back to 436 nm, the sequence occurred in reversed order.

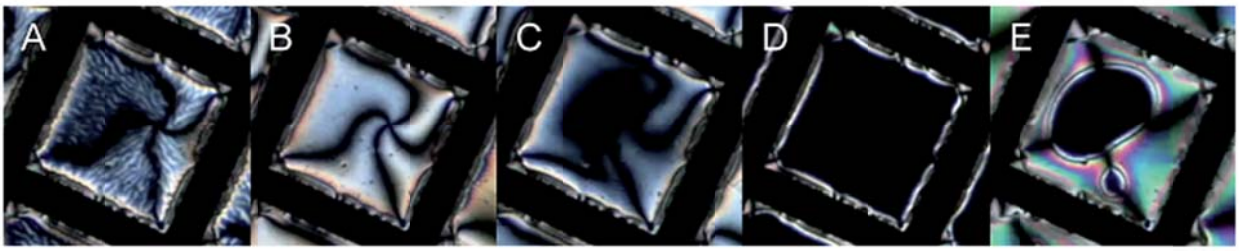

Figure A.4: Polarized microscope images (using crossed polarizers) of a nematic/water optical cell with 16.44 mM 8Az3 dissolved in the nematic phase at 25 ˚C. These representative images illustrate dynamic changes that occur over a period of 60 s when the wavelength of illumination is switched from 436 nm to 365 nm. (A) Photostationary state associated with illumination at 436 nm. (B–D) Intermediate dynamic states following illumination at 365 nm. (E) Photostationary state associated with illumination at 365 nm.

According to the results presented above, the stationary state associated with 436 nm illumination is 92% *trans* in solution, while that associated with 365 nm is 98% *cis* in solution. One does not necessarily expect the interfacial composition to be identical to that of the bulk for several reasons. Since the polarity of the interfacial environment is not identical to that of bulk solution, the photostationary state at the interface may be different from that in solution. Furthermore, the two isomers may partition somewhat differently to the interface. However, since the adsorbed 8Az3 isomers at the interface are in equilibrium with those dissolved in the bulk solution phase, as the bulk *cis/trans* ratio increases, so necessarily does the *cis/trans* ratio of the interfacial layer in equilibrium. Thus we hypothesized that the sequence of images shown in Figure A.4 represented the response of the liquid crystal to a series of phases associated with the

interfacial layer of 8Az3, as the composition gradually became richer in the *cis* isomer. To test this hypothesis, we characterized the appearance of the liquid crystal in contact with an interfacial layer of 8Az3 in equilibrium with a solution under four distinct steady illumination conditions: dark (all *trans*), 436 nm (8% *cis*), 405 nm (43% *cis*), and 365 nm (97% *cis*). Figure A.5 shows these photostationary states under the same thermodynamic conditions as Figure A.4 (16.44 mM 8Az3, 25 ˚C).

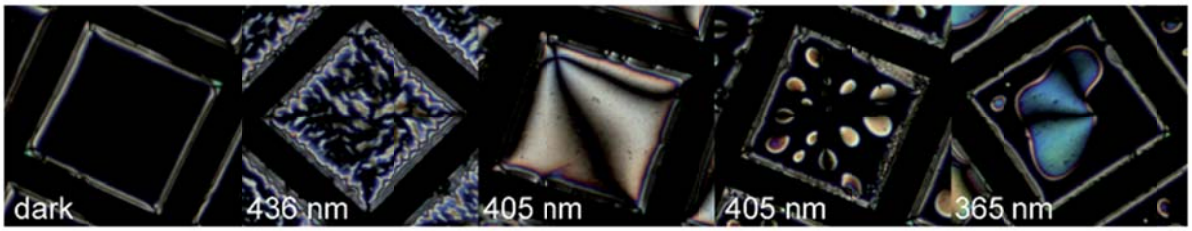

Figure A.5: Polarized microscope images (through crossed polarizers) of a liquid crystal/water optical cell with 16.44 mM 8Az3 dissolved in the nematic phase at 25 ˚C. These are representative images of photostationary states associated with irradiation at the respective annotated wavelengths. The appearance associated with the 405 nm illumination displays hysteresis depending on whether the prior illumination is at a longer (left image) or shorter (right image) wavelength.

We note that the sequences of liquid crystal textures associated with the dynamic changes (Figure A.4) and photostationary states (Figure A.5) are consistent: homeotropic to weakly-birefringent to homeotropic to more-strongly-birefringent. We also note that these sequences have all the characteristics of first-order phase transitions, including coexistence and reversibility. Interestingly, the 405 nm stationary

state images also indicate the presence of hysteresis, which is characteristic of a first-order phase transition (e.g. supercooling or supersaturation). That is, if the previous illumination is at a longer wavelength (i.e. 436 nm, giving a lower *cis* fraction), the sample displays uniform weak birefringence at 405 nm. However, if the previous illumination is at a shorter wavelength (i.e. 365 nm, giving a higher *cis* fraction), the sample displays coexistence of homeotropic and weakly birefringent regions at 405 nm.

By comparing stationary state images with dynamic changes upon a change of illumination wavelength, we determined the characteristic sequence of phases associated with a specific set of thermodynamic conditions. Figures A.4 and A.5 illustrate how this sequence was determined for samples at 25 ˚C and 16.44 mM 8Az3 in liquid crystal. The same procedure was followed for a matrix of thermodynamic conditions including four 8Az3 concentrations of 8.22 mM, 12.33 mM, 16.44 mM, and 20.55 mM at each of four temperatures, 5 ˚C, 15 ˚C, 25 ˚C, and 35 ˚C. In all cases, the sequence of photostationary states was consistent with the sequence observed dynamically upon a sudden change in illumination wavelength. All states and transitions were repeatable and reversible. Based on these data, phase diagrams were determined as a function of temperature, 8Az3 concentration, and illumination wavelength (i.e. bulk *cis/trans* composition). For convenience, a nomenclature was developed where each phase was given a symbolic name based on the predominant component. This nomenclature, descriptions of phases, and the phase diagrams themselves are presented in the following sections.

A.2.3 High Temperature Phases

At 15 ˚C, 25 ˚C, and 35 ˚C, the same phase sequence illustrated in Figures A.4 and A.5 was observed at higher 8Az3 concentrations. However, at very low 8Az3 concentrations, a strongly birefringent phase was observed, consistent with planar liquid crystal anchoring at the interface; the azimuthal orientation was random and varied continuously. The liquid crystal texture and birefringence in this phase was indistinguishable from the liquid crystal appearance in contact with a bare water interface. Therefore, we labeled this low-concentration phase as *G* (gas); such a phase has been similarly observed for low concentrations of *n*-alkanoic acid molecules at an identical interface.[7]

Representative images of all high-temperature phases and coexisting phases are shown in Figure A.6. The phases that would hypothetically be observed for pure *trans* or pure *cis* isomeric 8Az3 are labeled *T* and *C* respectively. Since there are two such *T* phases as a function of temperature, subscripts are used to distinguish them. The high temperature T_1 phase induced homeotropic anchoring. The *C* phase induced tilted liquid crystal anchoring that resulted in significant birefringence, as indicated by the deep blue color. The azimuthal orientation varied continuously and randomly in the *C* phase. We note here that our experimental conditions did not allow for the observation of a purely *cis* monolayer. However, the trend with wavelength and the topology of the phase diagram supports the conclusion that the liquid crystal texture associated with the emerging *C* phase (high birefringence with a continuously varying liquid crystal azimuth) would encompass the entire sample for a pure *cis* monolayer.

Two phases were observed in the interior of the phase diagram for all illumination wavelengths. These phases, observed only for isomer mixtures, are labeled *M*. The M_T phase was observed for *trans*-rich mixtures; the LC was weakly-birefringent with a random azimuthal orientation. The M_C phase was observed for *cis*-rich mixtures, and induced homeotropic anchoring. Although both the T_1 and M_C phases induced homeotropic anchoring, they are separated on the phase diagram by the M_T phase, which suggests that they are in fact distinct phases.

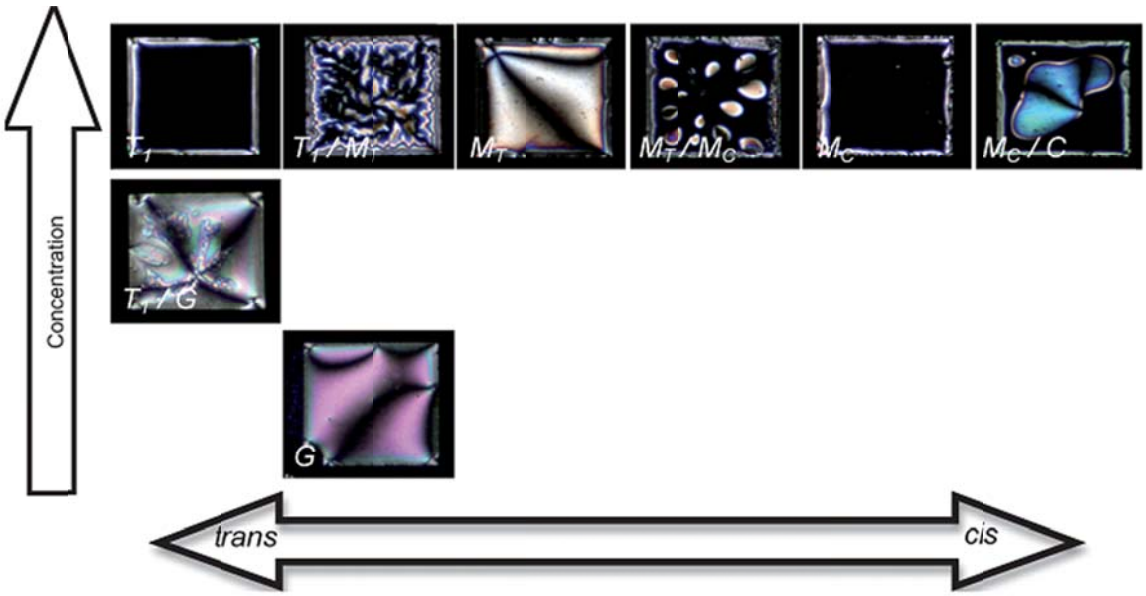

Figure A.6: Representative polarized light microscope images of each phase, or coexistence of phases, observed at temperatures of 15 ˚C or higher. The symbols assigned to the phases are annotated on the images.

A.2.4 Low temperatures

At 5 ˚C, a different texture was observed for pure *trans* 8Az3. The phase, which we label T_2, is characterized by weakly-birefringent meandering domains with distinct domain boundaries, as shown in Figure A.7. The T_2 phase is also seen in coexistence with the M_T phase. Rotation of the sample confirms that the contrast between T_2 domains corresponds to different azimuthal orientations of the nematic director. This type of domain structure corresponds to tilted condensed phases of fatty acid Langmuir monolayers (e.g. L_2, L_2')[12, 20] and was also observed in liquid crystal cells where fatty acids were adsorbed at the nematic/water interface.[7]

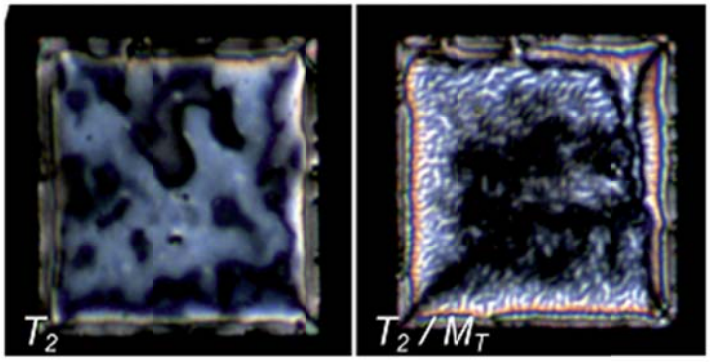

Figure A.7: Representative images of additional phases observed at 5 ˚C.

A.2.5 Phase diagrams

Phase diagrams were constructed that were consistent with all of the observations of dynamic changes and stationary states. These are presented in Figure A.8 as binary phase diagrams for each of the four temperatures studied. The horizontal lines on the diagrams represent thermodynamic paths associated with the dynamic changes observed after switching the illumination wavelength; these paths allowed us to determine the sequence of phases at that temperature and bulk concentration, and also the nature of the phase transitions. The axes of these phase diagrams correspond to the experimentally-accessible thermodynamic variables (bulk concentration and bulk composition) but do not necessarily correspond in a simple way to variables associated with the concentration and composition of the interfacial layer. This will be discussed in greater detail below. For example, we found that the M_T–M_C transition was first order at lower concentrations (i.e. coexistence was observed), but became continuous at higher concentrations. The vertical lines represent changes to 8Az3 concentrations at constant temperature and illumination wavelength. The intersecting grid lines represent the specific stationary states that were observed. These provided information about the absolute positions of transition lines. As a result of these measurements, the overall topology of the phase diagrams could be determined with confidence, and the relative shifts of phase transitions as a function of temperature could also be determined. For example, both *M* phases clearly shift to the left (*trans*-rich side) with increasing temperature.

First order (discontinuous) transitions (indicated by coexistence regions and tie lines) were characterized by the nucleation and growth of domains of the emerging

phase. The approximate locations of phase boundaries for these transitions were determined via the lever rule using area fractions of coexisting phases measured under stationary state conditions. However, hysteresis exhibited by these phase transitions left a degree of uncertainty in the precise positions of these boundaries. Continuous transitions did not exhibit phase coexistence. The dotted lines are speculative, but are supported by trends in the data. Some artistic license was taken in drawing the specific contours of the transition lines.

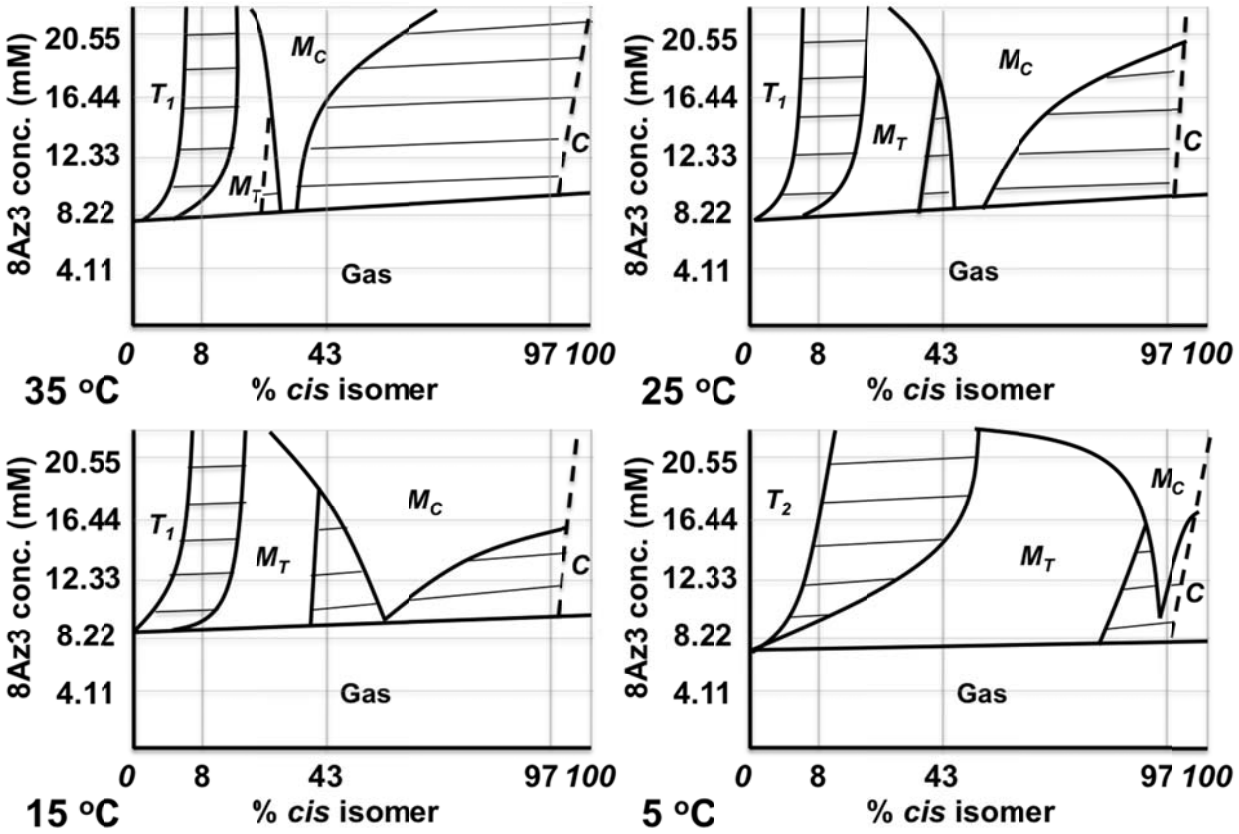

Figure A.8: Schematic phase diagrams constructed from the combination of stationary state observations and dynamic changes following a new illumination wavelength. The intersections between grid lines indicate stationary state conditions that were observed. The locations of phase boundaries are approximate, but the topologies are believed to be reliable.

A.2.6 Monolayers at the air/water interface and LB films

Past studies with Langmuir monolayers of the pure *trans* isomer of 8Az3 revealed the absence of isotropic 2D fluid phases (the equivalent to the L_1 or *LE* in fatty acid Langmuir monolayers) at all temperatures up to 50 ºC. This system features a high pressure phase with hexatic order, as suggested by textures in BAM images and by the analysis of GIXD data,[21] and a low pressure mesophase, which develops characteristic temperature-dependent textures.[14] Under all temperatures and surface pressures studied (up to monolayer collapse) molecules tilt away from the interface normal: no evidence of an untilted or isotropic phase has been found. In fact, monolayer compression has little effect on the tilt angle, in contrast with saturated fatty acid monolayers.[21]

As an intermediate system between the liquid crystal/water and the air/water interface, and to connect Brewster angle microscopy (BAM) images of Langmuir monolayers with polarized light microsroscopy images of liquid crystal cells, we have also examined the alignment patterns induced on a liquid crystal that is in contact with a Langmuir-Blodgett (LB) film of 8Az3 in a cell that is treated for homeotropic anchoring on the opposing plate[15]. Like the polarized light microscopy (PLM) images shown above, the nematic textures observed in the LB optical liquid crystal cell are in response to the structure of the 8Az3 interfacial layer, but unlike the PLM images (and like the BAM images) the 8Az3 monolayer structure formed at the air/water interface in the absence of structure-directing influences by an adjacent liquid crystal layer. As shown in Figure A.9, liquid crystal textures in contact with the 8Az3 LB film faithfully reproduce the structures observed in Langmuir monolayers of 8Az3 by BAM, both with pure *trans*

composition (Fig A.9A and A.9C) and with a photostationary *cis-trans* mixture (Fig A.9B and 8.9D).

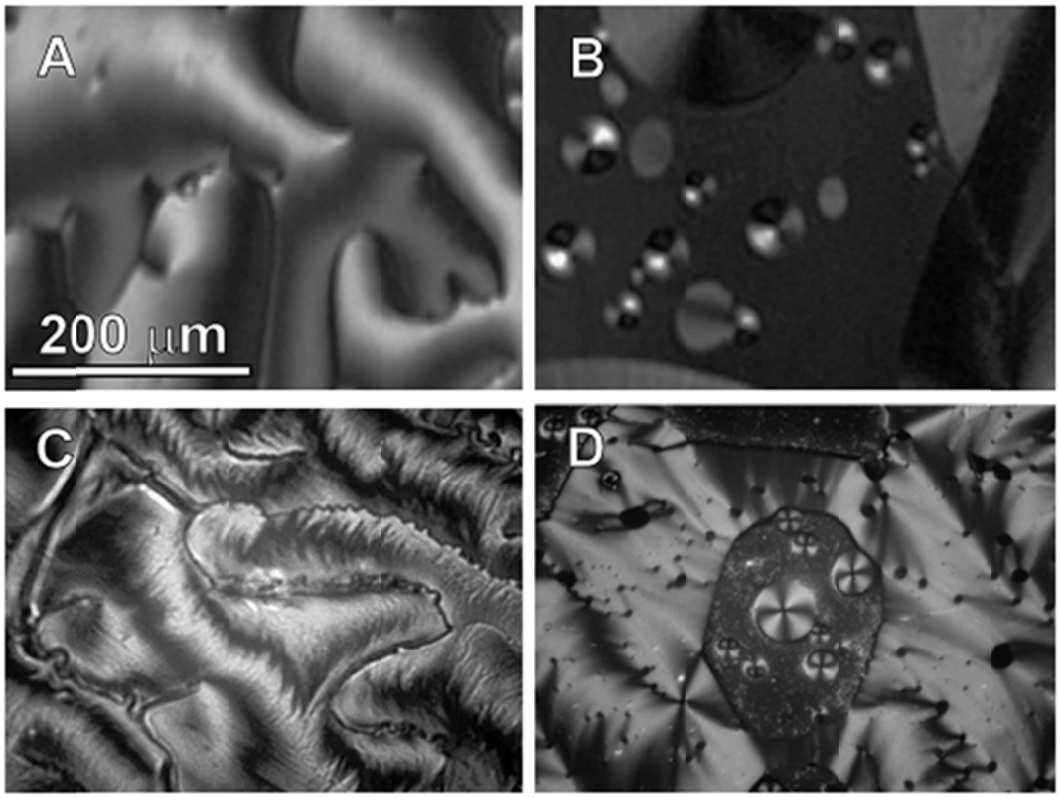

Figure A.9. BAM images of selected photostationary state textures in 8Az3 Langmuir monolayers.(A, B), and PLM images of the LC cell built with the corresponding LB film (C, D). Thermodynamic conditions are: (A, C) pure *trans*, 25 ºC, 2 mN/m; (B, D) room-light photostationary *cis-trans* mixture, 25 ºC, 2 mN/m.

A.3 Discussion

A.3.1 Relationship of bulk and interfacial phase diagrams

It is worth commenting on the connection between the phase diagrams presented in Figure A.8 (bulk concentration vs. bulk composition) and hypothetical 2D (interfacial concentration vs. interfacial composition) phase diagrams of the interfacial surfactant layer in equilibrium with the bulk solution. We emphasize that the axes of the phase diagrams in Figure A.8 correspond to thermodynamic variables associated with the bulk 8Az3-in-LC solution phase; these are of course the experimentally-accessible thermodynamic parameters (the bulk concentration is of course related to the solute's chemical potential.). One cannot, of course, assume that the surface composition and bulk composition are identical. Nor can one assume that a horizontal trajectory corresponds to a trajectory of constant total surface concentration. However, it is true that a horizontal trajectory in Figure A.8 associated with increasing *cis* fraction at constant total concentration does correspond to some trajectory within a 2D phase diagram where the interfacial concentration of *cis* also increases; however, the 2D trajectory will not in general be horizontal or even a straight line. Thus, the corresponding 2D phase diagram is likely to have the same topological structure, but will be distorted.

A.3.2 Liquid crystal textures at air/water and liquid crystal/water interface

It is also interesting to consider possible connections between the phases/textures associated with 8Az3 adsorbed at the nematic/aqueous interface and 8Az3 Langmuir monolayers at the air/water interface. The structures observed in the T_2 phase reported here at the liquid crystal/water interface are reminiscent of the textures at low temperatures and low-pressures in mesophases of *trans*-8Az3 Langmuir monolayers (Figure A.9A, C). However, it is far from clear how to correlate the T_1 phase (which leads to homeotropic anchoring) with the structures observed at the air/water interface. No isotropic phase is observed in 8Az3 Langmuir monolayers at the air/water interface at temperatures below 50 ˚C. Since the other side of the liquid crystal cell is homeotropically-anchored, homeotropic anchoring at the aqueous interface reduces the free energy due to elastic strain of the director field. Thus the elastic nature of the nematic director field would tend to favor phases that induce homeotropic anchoring. We speculate that this effect may result in the appearance of an isotropic (possibly untilted) phase for 8Az3 at the liquid crystal/water interface, though no analogous phase occurs at the air/water interface. A similar phenomenon was observed previously for phospholipid monolayers.[13]

Moving to the opposite side of the binary phase diagram, at the liquid crystal/water interface it is generally understood that the presence of *cis* isomers leads to disorder because these isomers frustrate molecular packing of alkyl chains.[22] Thus the *C* phase is likely a disordered phase, with the same symmetry as the *G* phase but with a significantly higher interfacial concentration leading to tilted, but not planar, anchoring. The intermediate liquid crystal tilt angles (25-35°) associated with the *C*

phase are unusual. It is more common for alignment layers to induce tilt angles that are either very large or very small. The disordered C phase correlates well with the isotropic textures observed on Langmuir monolayers of 8Az3 under UV illumination (maximum *cis* composition) and the corresponding LB plate under liquid crystal amplification (images not shown).

The presence of the *M* phases at the liquid crystal/water interface is an intriguing result. Their appearance in the interior of the phase diagram means that these thermodynamic phases exist only for mixtures, and do not appear in the phase diagram of either pure component. Although this not unprecedented in binary mixtures, it is an uncommon situation. This phase sequence is absent in 8Az3 monolayers at the air/water interface. Mixed *cis*-*trans* monolayers at the air/water interface exhibit the lateral coexistence of two phases: an isotropic *cis*-rich phase, and a *trans*-rich mesophase. Isolated domains of the latter form spontaneously and feature brush-like inner textures;[23] such textures are reproduced in the liquid crystal cells over LB plates (Figure A.9c, d). However, experiments show that these phases span the entire phase diagram at the air/water interface, from pure *cis* to pure *trans*. For example, one can monitor a continuous and slow transition from almost pure *cis* 8Az3 monolayers into pure *trans* form by exposing a spread monolayer to UV light, and allowing subsequent relaxation in the dark. Continuous BAM observation (with a deep red laser, which does not alter the *cis/trans* balance) shows the progressive formation of *trans*-rich mesophase domains in coexistence with the isotropic *cis*-rich medium. Only these two distinctive phases are observed in coexistence until the entire air/water interface is covered by the *trans* mesophase. In contrast, the M_C and M_T phases observed at the

liquid crystal/water interface appear only for mixtures and are not present for pure *trans* or pure *cis* monolayers.

A.3.3 Phases introduced by interactions with liquid crystals

Earlier studies with saturated fatty acid monolayers at the liquid crystal/water interface reported a phase sequence analogous to the one known at the air/water interface, but with a systematic 40 ºC depression of phase transition temperatures.[7] We have performed experiments on 8Az3 Langmuir monolayers to try to assess a similar relationship with phases at the liquid crystal/water interface. We have increased the temperature of pure *trans* monolayers up to nearly 50 ºC (at a constant lateral pressure of 2 mN/m), and we have found no evidence of an isotropic phase that could match the T_1 phase reported in the current work. We have also explored the phase coexistence in mixed *cis/trans* monolayers in the range of temperatures from 5ºC up to nearly 50ºC, and we have found only small changes in the lateral miscibility of the two components, and no evidence of intermediate single phase mixtures. We therefore hypothesize that the rich phase behavior of 8Az3 at the nematic liquid crystal/ water interface is due to its interaction with the adjacent liquid crystal phase.

We considered the prospect that changes to the liquid crystal textures may be due to the presence of 8Az3 in the bulk liquid crystal as opposed to anchoring transitions associated with interfacial monolayer phases. For example, liquid crystal materials that are “doped” with solute have been observed to exhibit new phases (although the doping is generally at much higher concentrations than used here).[11] It is

also possible that doped liquid crystals may also exhibit modified anchoring behavior or energies. In order to investigate this possibility, we performed identical experiments to those reported above, but with the liquid crystal water interface replaced by the liquid crystal/air interface. The amphiphilic 8Az3 is not expected to adsorb preferentially at the liquid crystal/air interface, so these experiments were expected to provide some information about the intrinsic effect of 8Az3 on the bulk liquid crystal phases and textures. Homeotropic alignment was observed for all illumination wavelengths, temperatures, and concentrations investigated (data not shown). Homeotropic alignment was also observed at the air interface when using an undoped nematic liquid crystal.

These control experiments demonstrate that no significant anchoring changes occur at the OTS SAM/liquid crystal interface or at the liquid crystal/air interface as a function of illumination. This suggests that there is no dramatic change in the bulk phase behavior or bulk symmetry and that the variable orientational behavior with *cis/trans* ratio is associated with the nematic/water interface. It is also important to note that bulk changes associated with doping would not be expected to lead to spatial heterogeneity such as we observe and attribute to interfacial phase separation. The coexistence of lateral domains that we observe is stable, reversible, and change consistently with temperature and bulk concentration. Taken as a whole, these observations are self-consistent and in agreement with what one would expect for phenomena driven by phase transitions in an interfacial layer.

A.4 Conclusions

A photoisomerizable, azobenezene-containing amphiphilic fatty acid was dissolved in a nematic liquid crystal phase and allowed to adsorb at the liquid crystal /water interface. A number of orientational states of the liquid crystal were observed as a function of concentration, temperature, and photostationary state (*cis/trans* isomeric ratio). Reversible continuous and discontinuous transitions were observed between these states suggesting the existence of various equilibrium monolayer phases as a function of binary composition. The orientation and texture of the adjacent liquid crystal phase reflected the molecular arrangement and texture within these interfacial phases. The phase diagram topology was determined as a function of temperature, surfactant concentration, and photostationary state, using empirically-observed liquid crystal textures to identify phases and phase transitions. Six distinct interfacial phases were identified, including five condensed phases and a dilute interfacial vapor phase. Interestingly, two of the condensed phases appeared only for *cis/trans* mixtures, indicating a degree of miscibility at the liquid crystal/water interface that is absent for analogous monolayers at the air/water interface, where only two condensed phases are observed, one for *trans*-rich monolayers and one for *cis*-rich monolayers. This demonstrates that interaction with an adjacent bulk nematic phase can not only shift phase transitions, it can also induce the appearance of new phases and modify the lateral miscibility of monolayer components.

A.5 References

1. Brake, J. M.; Daschner, M. K.; Abbott, N. L., Formation and Characterization of Phospholipid Monolayers Spontaneously Assembled at Interfaces between Aqueous Phases and Thermotropic Liquid Crystals. *Langmuir* **2005,** 21, (6), 2218-2228.

2. Price, A. D.; Schwartz, D. K., Fatty-Acid Monolayers at the Nematic/Water Interface: Phases and Liquid-Crystal Alignment. *J. Phys. Chem. B* **2007,** 111, (5), 1007-1015.

3. Price, A. D.; Schwartz, D. K., DNA Hybridization-Induced Reorientation of Liquid Crystal Anchoring at the Nematic Liquid Crystal/Aqueous Interface. *J. Am. Chem. Soc.* **2008,** 130, (26), 8188-8194.

4. Jerome, B., Surface Effects and Anchoring in Liquid-Crystals. *Reports on Progress in Physics* **1991,** 54, (3), 391-451.

5. Lockwood, N. A.; Abbott, N. L., Self-assembly of surfactants and phospholipids at interfaces between aqueous phases and thermotropic liquid crystals. *Current Opinion in Colloid & Interface Science* **2005,** 10, (3-4), 111-120.

6. Brake, J. M.; Mezera, A. D.; Abbott, N. L., Active Control of the Anchoring of 4'-Pentyl-4-cyanobiphenyl (5CB) at an Aqueous-Liquid Crystal Interface By Using a Redox-Active Ferrocenyl Surfactant. *Langmuir* **2003,** 19, (21), 8629-8637.

7. Price, A. D.; Schwartz, D. K., Fatty-acid monolayers at the nematic/water interface: Phases and liquid-crystal alignment. *Journal of Physical Chemistry B* **2007,** 111, (5), 1007-1015.

8. Ichimura, K.; Suzuki, Y.; Seki, T.; Hosoki, A.; Aoki, K., Reversible Change in Alignment Mode of Nematic Liquid-Crystals Regulated Photochemically by Command Surfaces Modified with an Azobenzene Monolayer. *Langmuir* **1988,** 4, (5), 1214-1216.

9. Ichimura, K.; Hayashi, Y.; Ishizuki, N., Photocontrol of Inplane Alignment of a Nematic Liquid-Crystal by a Photochromic Spiropyran Monolayer Absorbing Linearly Polarized-Light. *Chemistry Letters* **1992**, (6), 1063-1066.

10. Ichimura, K.; Tomita, H.; Kudo, K., Command surfaces .14. Photoregulation of in-plane alignment of a liquid crystal by the photoisomerization of stilbenes chemisorbed on a substrate silica surface. *Liquid Crystals* **1996,** 20, (2), 161-169.

11. Ichimura, K., Photoalignment of liquid-crystal systems. *Chemical Reviews* **2000,** 100, (5), 1847-1873.

12. Kaganer, V. M.; Mohwald, H.; Dutta, P., Structure and phase transitions in Langmuir monolayers. *Reviews of Modern Physics* **1999,** 71, (3), 779-819.

13. Gupta, J. K.; Meli, M. V.; Teren, S.; Abbott, N. L., Elastic energy-driven phase separation of phospholipid monolayers at the nematic liquid-crystal-aqueous interface. *Physical Review Letters* **2008,** 1, (4).

14. Crusats, J.; Albalat, R.; Claret, J.; Ignes-Mullol, J.; Sagues, F., Influence of temperature and composition on the mesoscopic textures of azobenzene Langmuir monolayers. *Langmuir* **2004,** 20, (20), 8668-8674.

15. Fang, J. Y.; Gehlert, U.; Shashidar, R.; Knobler, C. M., Imaging the azimuthal tilt order in monolayers by liquid crystal optical amplification. *Langmuir* **1999,** 15, (2), 297-299.

16. Fischer, E., Calculation of photostationary states in systems A<=>B when only A is known. *Journal of Physical Chemistry* **1967,** 71, 3704-3706.

17. Rau, H.; Greiner, G.; Gauglitz, G.; Meier, H., Photochemical Quantum yields in the A(+hv)<=>B (+hv,delta) system when only the spectrum of A is known. *Journal of Physical Chemistry* **1990,** 94, 6523-6524.

18. Aronzon, D.; Levy, E. P.; Collings, P. J.; Chanishvili, A.; Chilaya, G.; Petriashvili, G., rans-cis isomerization on an azoxybenzene liquid crystal. *Liquid Crystals* **2007,** 34, 707-718.

19. Asano, T.; Okada, T., Thermal Z-E Isomerization of Azobenzenes. The Pressure, Solvent, and Substituent Effects. *Journal of Organic Chemistry* **1984,** 49, 4387-4391.

20. Riviere, S.; Henon, S.; Meunier, J.; Schwartz, D. K.; Tsao, M. W.; Knobler, C. M., Textures and Phase-Transitions in Langmuir Monolayers of Fatty- Acids - a Comparative Brewster-Angle Microscope and Polarized Fluorescence Microscope Study. *Journal of Chemical Physics* **1994,** 101, (11), 10045-10051.

21. Durbin, M. K.; Malik, A.; Richter, A. G.; Yu, C. J.; Eisenhower, R.; Dutta, P., Ordered phases in Langmuir monolayers of an azobenzene derivative. *Langmuir* **1998,** 14, (4), 899-903.

22. Yim, K. S.; Fuller, G. G., Influence of phase transition and photoisomerization on interfacial rheology. *Physical Review E* **2003,** 67, (4).

23. Ignes-Mullol, J.; Claret, J.; Albalat, R.; Crusats, J.; Reigada, R.; Romero, M. T. M.; Sagues, F., Texture changes inside smectic-C droplets in azobenzene langmuir monolayers. *Langmuir* **2005,** 21, (7), 2948-2955.

Appendix B

Liquid Crystal Detection of Oligonucleotide Hybridization

B.1 Introduction

Insofar, this dissertation has demonstrated that extended DNA molecules orient nematic liquid crystals oblique to the extension direction at an azimuthal angle of 30º. This response is unique to chiral molecules, as liquid crystal generally aligns itself in the direction of anisotropy (i.e. the extension direction). While we have demonstrated the ability to distinguish between double and single-stranded DNA, it is far from becoming a useful technology. We have merely demonstrated that extremely long, genomic length DNA can disrupt liquid crystalline alignment. For this to be a viable detection scheme, however, we must demonstrate that not only do long molecules of extended DNA align liquid crystals, but that oligonucleotide-length DNA is able to disrupt liquid crystalline alignment. Current approaches in DNA technology use oligonucleotide length (usually less than 200 nucleotides), rather than the 15,000-48,000 base pair-length DNA used in this work. As there are only 10 base pairs per rotation in a double helix, it is logical that oligonucleotide-length DNA strands will retain the necessary secondary structure (e.g. the major and minor grooves of the double helix) necessary to induce the oblique liquid crystal alignment observed when it is in contact with long DNA strands.

To fully test the feasibility of this method as a sensing mechanism, we want to test (1) prove that shorter DNA strands evoke the same liquid crystal alignment as long

strands of DNA (2), direct attachment of a single stranded oligonucleotide, followed by surface hybridization. Chapter 3 has demonstrated that the ratio of extended to coiled molecules has a direct effect on liquid crystal alignment. Therefore, optimization of extension would also be useful. It would be ideal to optimize this parameter as well, but the multiple theories surrounding the mechanism of DNA attachment and leave too many options to be explored in the remaining time frame.

B.2 Goals

B.2.1 Shortening DNA stands for extension

Again, the key experimental parameter for a useful DNA sensor is the ability to distinguish between dsDNA and ssDNA. However, we have only proved the ability to distinguish between long, genomic strands of dsDNA and ssDNA. Only 10 base pairs are required to complete a turn in a dsDNA double helix, therefore if our hypothesis that it is the major groove of dsDNA providing the chirality necessary to induce alignment is true.[1] As we have reason to believe that the liquid crystal alignment is affected by the ratio of extended to coiled DNA, we hypothesize that shortened would also be able to align liquid crystal at the unique oblique angle of -32±4. With that in mind, shortened DNA strands still carry the distinct possibility of increased efficiency of DNA extension, as more strands attach with decreasing strand length.[1] Additionally, as we believe that multiple attachment points within the DNA strand lead to pinned, entangled DNA that does not extend during the molecular combing process, it follows that shorter strands, with their more reactive ends, could have a higher fidelity in extension, leading to increased, more reliable liquid crystal alignment. The other distinct possibility is that a

much higher surface concentration of extended DNA is necessary to impart liquid crystalline alignment. As we are aiming to shift from strands that are 48,500 bp to strands of 200 bp or less, many more strands of DNA would have to be on the surface, even while retaining identical surface coverage of DNA.

We have explored two methods for shortening DNA: degradation by sonication, and cutting via restriction enzyme. Shortening techniques were as follows: sonication (9 W probe sonicator) for 90 seconds, which results in fragments 100-1000 base pairs. In Figure B.1, one can see the evolving distribution of DNA strand lengths with sonication. Above 30 seconds, no additional shortening was observed, and DNA remained between 100 and 1000 base pairs.

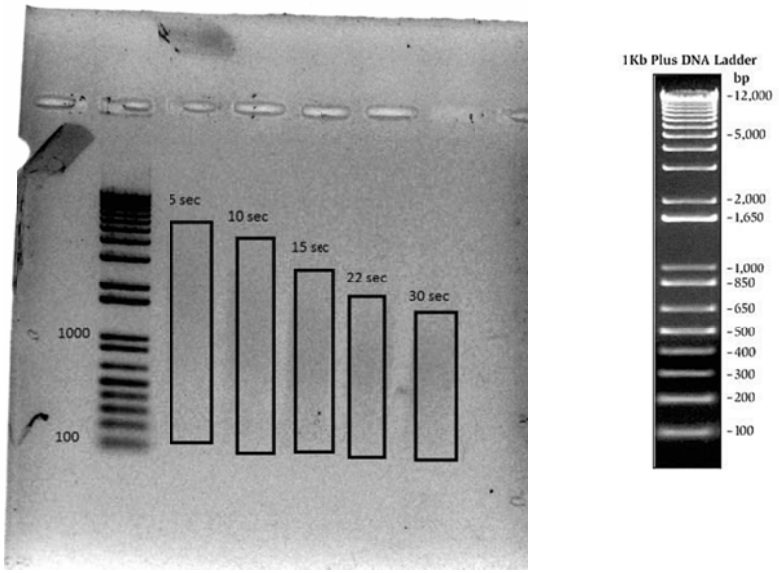

Figure B.1: Agarose gel electrophoresis detailing shortening via sonication. Times longer than 30 seconds are not shown, as the DNA remains between 100-100 base pairs.

Sonication of lambda DNA, however has its drawbacks. First, the heat generated by the procedure has the potential to denature the DNA. This can be mitigated by sonicating the sample while immersed in an ice bath, though this cannot dissipate all the heat in the sample volume. More importantly, there is no specific length control beyond 100-1000bp.

We have observed that in fact, sonicated DNA of length 100-1000bp induces liquid crystal alignment. Unfortunately, due to the size of the DNA fragments, it is impossible to visually inspect these fragments for extension. They are expected to be no longer than ~ 500 nm, leaving them within the realm of a diffraction limited spot. However, as can be seen in the preliminary experiments in figure B.2, the liquid crystal

is clearly aligned at an oblique angle to the extension direction. Initial experiments using DNA with length 100-400 bp (Sonication at power 8 for 90 seconds) causes irregular liquid crystal alignment. This is likely due to the degradation process of shearing. With this amount of shear, it is likely there is much more single stranded DNA, as well as unpaired DNA ends. This again demonstrates the sensitivity of liquid crystals to phenomenon indefectible by more conventional microscopy methods.

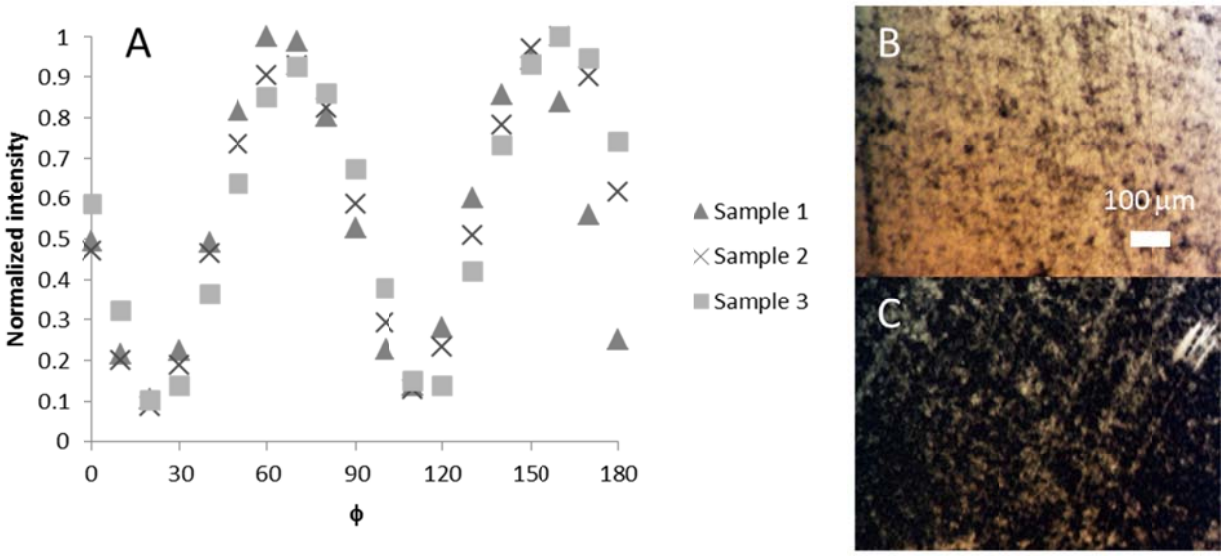

Figure B.2: Liquid crystal aligned by sonicated DNA, with a final length ranging between 100-1000 base pairs. A) Normalized intensity as a function of rotation. B) Example at 0 degree rotation. C) Example at 30 degree rotation.

In order to gain full control of the length of DNA fragments, a more selective method of cutting DNA must be used. Restriction enzymes digest DNA by cutting at specific sites. We have used two enzymes, EagI and SphI to reduce DNA to lengths ranging from 900-20,000 bp. Table B.1 describes restriction sites and lengths of

fragments produced. While restriction enzymes cut with high fidelity under proper reaction conditions, the quantity of DNA recoverable from agarose gels in insufficient to perform molecular combing experiments with the current protocol. Only a few nanograms at a time are recovered from agarose gels, and microgram quantities are in fact used in the current DNA deposition method. Thus, the larger quantities of DNA available via sonication were used experimentally, despite the ability to precisely control for DNA length with the digested DNA.

There is obviously an essentially infinite combination of restriction enzymes and lengths of cut DNA, but the concentration of recoverable DNA separated by agarose gel is too low be useful in the current method of molecular combing. A separation method with a higher yield would enable testing of discrete, known DNA sequences. However, due to the larger quantities possible from sonicated DNA, only it has been shown to induce liquid crystal alignment oblique to the dipping direction.

Table B.1: Restriction Enzyme cut site and fragment length for lambda phage DNA

Restriction Enzyme	**Cut Site**	Fragment length (base pairs)
EagI	2212 12002 23442 24371 27374 36654 48805	11961 16710 19944
SphI	19944 39418	929 2212 3003 9084 9790 11440 12044
EagI SphI double digest	2212 12002 19944 23442 24371 27374 36654 39418 48805	929 2764 3003 3498 7942 9280 9387 9790

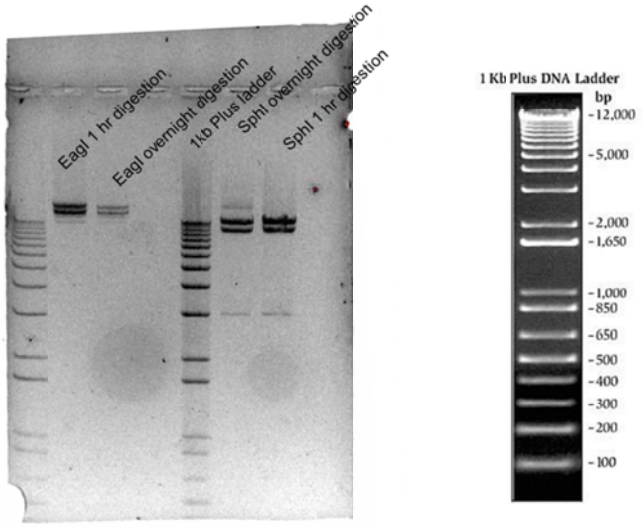

Figure B.3: Digestion of EagI and SphI. DNA bands with discrete chain lengths are clearly visible, but only a few nanograms are recoverable from each lane. The current molecular combing protocol uses ~50 microgram of DNA per experiment.

B.2.2 Orthogonal labeling of dsDNA and ssDNA

We have clearly demonstrated that dsDNA must be well-extended to induce oblique alignment in DNA. Additionally, we have demonstrated that ssDNA aligns the liquid crystal in the extension direction, as expected for any extended non-chiral polymer. What is less clear, however, is the threshold of sensitivity that detects double stranded DNA over background of single stranded DNA. If the goal is to detect specific sequences via hybridization on a solid surface, it is logical to assume that not all available probes will hybridize to target.

To accurately predict the relationship between liquid crystal alignment, ssDNA, and dsDNA, we must first orthogonally label ssDNA and dsDNA. The method used in

Chapter 3, YOYO-1 iodide, intercalate into the double helix, and is thus specific to dsDNA.[2-7] Successful labeling of ssDNA requires a different technique. The ULYSIS (Invitrogen) system is based on the universal linkage reagent by Kreatech.[8] This procedure covalently attaches a fluorophore of choice to the phosphate backbone of the DNA. Thus, even when denatured, we are able to observe the ssDNA fluorescently. YOYO-1 iodide (491 excitation/509 emission) was selected due to label dsDNA. While there is a small amount of overlap in the spectral excitation/emission spectrums of the two fluorophores, crosstalk between channels is negligible (within error for background).

B.2.3 Epoxide-Amine oligonucleotide attachment

In many arrays, oligonucleotide density closer than 1 molecule per 4 nm^2 to prevent steric hindrances from interfering with hybridization.[9] The overall goal of this work is to attach known probe sequences to the surface, so that we may then measure the amount of DNA on the surface. The hypothesis for attachment is the amine-epoxide attachment mechanism. It is well known that epoxide rings are subject to a nucleophilic ring-opening attack.[10] An amine linker has already been used in several cases to attach oligonucleotides to epoxide surfaces.[11 12-14] It is especially convenient that this epoxide layer imparts degenerate azimuthal anchoring, the prerequisite for our detection scheme using extended DNA molecules. Unfortunately, the epoxide layer seems to be extremely sensitive to deposition conditions. While pH 9 and above is purported to be ideal range for nucleophilic ring opening reacting, we believe that this is in fact an overly reactive condition. At pH above 9, oligonucleotide attachment was low,

and sample to sample variation was unacceptably inconsistent (data not shown). Literature deposition conditions range from pure water[11], to as basic as to 100 mM KOH (pH 12).[13, 14] The Beattie group recommends attachment in water due to increased nonspecific attachment during the hybridization step (presumably due to the disappearance of any blocking from the epoxide groups), as well as increased drop spreading due to monolayer destruction by the basic solution. Surprisingly, they also found that probe attachment increased at lower temperatures (20 ºC as opposed to 37 ºC or 65 ºC), again presumably reducing the reactivity of water, causing increased selectivity for a primary amine to act as a nucleophile. While other literature suggested both elevated and room temperature protocols, we found that attachment occurred even at conditions initially considered too mild for the nucleophilic reaction to occur (room temperature at neutral pH).

We propose that at extremely favorable reaction conditions such as elevated temperature, and high pH, water itself acts a nucleophile, and due to its vast excess as the solvent, can easily outcompete any other nucleophile in solution, therefore causing decreased attachment efficiency. Elevated temperatures are also known to drive the ring-opening reaction, but these elevated temperatures were also suspected in favoring water as a nucleophile over primary amines due to the vast excess of water in an aqueous solution.

B.2.4 Streptavidin-biotin attachment

As attachment via amine-epoxide linkage proves unreliable, we explore a second option for linkage. Streptavidin-biotin interactions are some of the strongest non-covalent interactions available.[10] The binding affinity is extremely high, on the order of $K_a = 10^{15}\, M^{-1}$ [15,16], causing equilibrium to shift to the point of nearly every molecule being bound. These bonds are secure, as long as temperature is kept low enough to prevent protein denaturation. These were also attempted as a method to attach oligonucleotides to a streptavidin coated surface. While streptavidin is not GPTMS, which is known to produce degenerately aligned liquid crystal with not surface memory effect, it was suspected that this protein would induce degenerate azimuthal alignment. Work completed in the Abbott group demonstrated that films of bovine serum albumin (BSA) induced degenerate alignment, but that the alignment would change in the direction of any rubbing.[17] It is therefore reasonable to hypothesize that another, similar protein could cause induce degenerate alignment. Similar to other alignment layers that induce degenerate planar alignment, a protein layers is expected to have a surface memory effect. It is, however, irrelevant to distinguishing between double and single stranded DNA. We would, however, be unable to distinguish between single stranded DNA and a control state without DNA. Assuming that passing through a moving interface affects a BSA layer similarly to mechanical rubbing, we would no longer be able to distinguish between single stranded DNA and absence of DNA.

Double stranded DNA, however, would still give oblique alignment due to its unique chiral structure. Thus, we would continue to show a unique liquid crystal signature for double-stranded DNA, again allowing for sensitive detections.

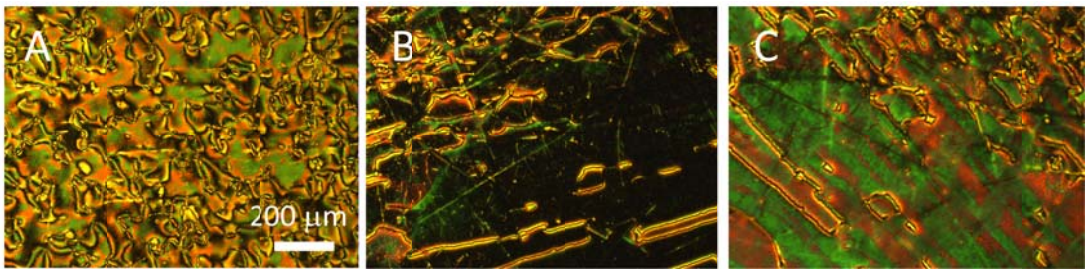

Figure B.4: Liquid crystal interactions with streptavidin. A) Streptavidin/OTS hybrid aligned cell. Schlieran textures indicate degenerate planar alignment. B) Streptavidin/OTS hybrid aligned cell passed through the interface to mimic DNA extension. Dipping direction is aligned with the crossed polarizer. Extinction indicates that passing through the interface causes liquid crystal alignment with a streptavidin layer. C) Streptavidin/OTS hybrid aligned cell when dipping direction is 45º to crossed polarizers.

B.2.5 Oligonucleotide hybridization

DNA hybridization occurs most efficiently at 5-10 ºC beneath the melting point (T_m). T_m is defined as the temperature at which 50% of bases are paired with their complement. T_m was taken from product information from Operon Biosciences.[18 19] Surface hybridization was attempted. In order for hybridization to occur at the surface, we must aim for significantly less stringent conditions than used in previous work in our group.[20] In previous work, extremely high stringency conditions (mM salt concentration) were used in order to more fully demonstrate that hybridization would only occur at the liquid-liquid crystal interface. In this case, as any probe molecule can only hybridize on the solid substrate, as it is the only place complementary strands will exist.[18] High stringency is defined as conditions that are unfavorable to DNA hybridization, therefore, only highly complementary pairs will remain hybridized. Stringency can depend on salt

concentrations, pH, and temperature. In experiments with Na^+, it was shown that helix stability increase up to approximately 1M. Helix stability is relatively insensitive to pH changes between 5 and 9. At low pH, bases in the single strand binds more than protons than in the duplex, thus favoring the single strand. At higher pH, the bases are deprotonated, eliminated normal hydrogen bonding and increasing charge repulsion. An eventual goal is surface hybridization. Preliminary hybridization experiments show that either stringency conditions must be optimized, or that hybridization is impeded at the solid interface. In order for hybridization to occur, we must aim for significantly less stringent conditions than used in previous work in our group, in which hybridization could only occur due to the partitioning of DNA to the liquid-liquid crystal interface[20]. In this case, the goal is surface hybridization to DNA probes covalently attached to a GPTMS SAM. DNA hybridization occurs most efficiently at 5-10 ºC beneath the melting point [18 19]. DNA helices becomes increasingly stable up to 1 M NaCl[9,21]. Surface hybridization was attempted with GPTMS SAMs with covalently attached 32 bp oligonucleotides. Sequence amine_32_488 (See Chapter 5.2.2) was attached. Attachment was verified by increase of fluorescence over background which remained after a boiling water rinse. BSA has been shown to induce degenerate azimuthal anchoring without rubbing. It could function as a blocking agent during hybridization studies [17].

B.3 References

1. Singh, V.; Zharnikov, M.; Gulino, A.; Gupta, T., DNA immobilization, delivery and cleavage on solid supports. *Journal of Materials Chemistry* **2011,** 21, (29), 10602-10618.

2. Carlsson, C.; Larsson, A.; Jonsson, M.; Albinsson, B.; Norden, B., Optical and Photophysical Properties of the Oxazole Yellow DNA Probes YO and YOYO. *Journal of Physical Chemistry* **1994,** 98, (40), 10313-10321.

3. Gurrieri, S.; Wells, K. S.; Johnson, I. D.; Bustamante, C., Direct visualization of individual DNA molecules by fluorescence microscopy: Characterization of the factors affecting signal/background and optimization of imaging conditions using YOYO. *Analytical Biochemistry* **1997,** 249, (1), 44-53.

4. Larsson, A.; Carlsson, C.; Jonsson, M.; Albinsson, B., Charachterization of the Binding of the Fluorecent Dyes YO and YOYO to DNA by Polarized-LIght Spectroscopy *Journal of the American Chemical Society* **1994,** 116, (19), 8459-8465.

5. Reuter, M.; Dryden, D. T. F., The kinetics of YOYO-1 intercalation into single molecules of double-stranded DNA. *Biochemical and Biophysical Research Communications* 403, (2), 225-229.

6. Rye, H. S.; Yue, S.; Wemmer, D. E.; Quesada, M. A.; Haugland, R. P.; Mathies, R. A.; Glazer, A. N., Stable fluorescent complexes of double-stranded DNA with bis-intercalating asymmetric cyanine dyes: properties and applications. *Nucleic Acids Research* **1992,** 20, (11), 2803-2812.

7. Akerman, B.; Tuite, E., Single- and double-strand photocleavage of DNA by YO, YOYO and TOTO. *Nucl. Acids Res.* **1996,** 24, (6), 1080-1090.

8. Kreatech http://www.kreatech.com/us/products/ulstm-labeling-kits/general-labeling-kits.html.

9. Schena, M., *Microarray Analysis*. Wiley-Liess: 2003.

10. Hermanson, G. T., *Bioconjugate Techniques*. 2 ed.; Elsiver Academic Press: Amsterdam, Boston, 2008.

11. Liu, X.; Krull, U. J., DNA hybridization on silica microbeads that are physically adsorbed as arrays on glass surfaces. *Anal. Chim. Acta* **2006,** 562, (1), 1-8.

12. Beattie, K.; Beattie, W.; Meng, L.; Turner, S.; Coral-Vazquez, R.; Smith, D.; McIntyre, P.; Dao, D., Advances in genosensor research. *Clin Chem* **1995,** 41, (5), 700-706.

13. Beattie, W.; Meng, L.; Turner, S.; Varma, R.; Dao, D.; Beattie, K., Hybridization of DNA targets to glass-tethered oligonucleotide probes. *Molecular Biotechnology* **1995,** 4, (3), 213-225.

14. Lamture, J. B.; LBeattie, K.; Burke, B. E.; Eggers, M. D.; Ehrlich, D. J.; Fowler, R.; Hollis, M. A.; Kosicki, B. B.; Reich, R. K.; Smith, S. R.; Varma, R. S.; Hogan, M. E., Direct detection of nucleic acid hybridization on the surface of a charge coupled device. *Nucleic Acids Res.* **1994,** 22, (11), 2121-2125.

15. Holmberg, A.; Blomstergren, A.; Nord, O.; Lukacs, M.; Lundeberg, J.; Uhlén, M., The biotin-streptavidin interaction can be reversibly broken using water at elevated temperatures. *Electrophoresis* **2005,** 26, (3), 501-510.

16. Sassolas, A.; Leca-Bouvier, B. D.; Blum, L. J., DNA Biosensors and Microarrays. *Chem. Rev.* **2007,** 108, (1), 109-139.

17. Kim, S. R.; Abbott, N. L., Rubbed Films of Functionalized Bovine Serum Albumin as Substrates for the Imaging of Protein–Receptor Interactions Using Liquid Crystals. *Advanced Materials* **2001,** 13, (19), 1445-1449.

18. Anderson, M. L. M., *Nucleic Acid Hybridization*. Springer: New York, 1999.

19. Bloomfield, V. A.; Crothers, D. M.; Ignacio Itnoco, J., *Nucleic Acids: Structure, Properties, and Functions*. University Science Books: Sausalito, CA, 2000.

20. Price, A. D.; Schwartz, D. K., DNA Hybridization-Induced Reorientation of Liquid Crystal Anchoring at the Nematic Liquid Crystal/Aqueous Interface. *J. Am. Chem. Soc.* **2008,** 130, (26), 8188-8194.

21. Lemieux, B.; Aharoni, A.; Schena, M., Overview of DNA chip technology. *Molecular Breeding* **1998,** 4, (4), 277-289.